

Adjacency effect in nearshore aquatic remote sensing: modelling, correction, and application

Yulun Wu

Thesis submitted to the University of Ottawa
in partial fulfillment of the requirements for the degree of
Doctor of Philosophy in Geography

Department of Geography, Environment and Geomatics
University of Ottawa

Supervisor:
Anders Knudby

Thesis Committee:
David Lapen
Michael Sawada
Chuiqing Zeng

© Yulun Wu, Ottawa, Canada, 2025

Abstract

The adjacency effect (AE) alters the top-of-atmosphere signals of coastal and inland waters, and it poses a major challenge for remote sensing of nearshore aquatic environments. To address this, we developed a Monte Carlo-based 3D radiative transfer model to study the AE, validated its accuracy against existing codes, and conducted case studies to demonstrate its application in analyzing the impact of AE in custom environments. In addition, we introduced a methodology and code for AE correction and demonstrated significant improvements in satellite-derived water-leaving reflectance retrievals using globally distributed *in situ* reflectance measurements. The tool, named T-Mart, is open-source and publicly available (<https://github.com/yulunwu8/tmart>). We applied AE correction and evaluated the performance and limitations of satellite-based water quality retrievals in small rivers traversing agricultural lands in Eastern Ontario, Canada. Satellite-derived reflectance and water quality parameters were validated against *in situ* measurements collected from May to October 2023. In the South Nation River and the Ottawa River, turbidity can be reliably monitored. Despite the improved retrievals through AE correction, further work is required to accurately monitor coloured dissolved organic matter and chlorophyll-a. While the findings highlight the complexities of satellite-based water quality monitoring applications for small rivers, AE correction represents a crucial step towards more accurate aquatic remote sensing of inland waters, laying the groundwork for more refined methodologies in future studies.

Acknowledgements

This work would not have been possible without the generous financial support of Agriculture and Agri-Food Canada, the Shallow Water Earth Observation Lab, Liquid Geomatics, the Canadian Space Agency, the University of Ottawa Admission Scholarship, and the Ontario Graduate Scholarship. I am also deeply grateful for the Big Idea Grant from the office of International Research and Experiential Learning, which allowed me to pursue a project outside my thesis. I sincerely thank the International Ocean Colour Coordinating Group (IOCCG), the Laboratoire d'Océanographie de Villefranche-sur-Mer, and the French Space Agency for facilitating and funding my attendance at the IOCCG Summer Lecture Series in 2022, and to the Ocean Carbon and Biogeochemistry program for organizing and funding my participation at the PACE Hackweek 2024. Additionally, I am thankful for travel grants provided by the Faculty of Arts, GSAED, IOCCG, and the Canadian Remote Sensing Society, which allowed me to present my work at various conferences.

I am immensely grateful to my supervisor, Dr. Anders Knudby, for your unwavering trust, vision in science, and your invaluable guidance throughout this journey. Your dedication to prioritizing learning opportunities for students has shaped my academic path, and I cannot imagine completing this journey without you. To Dr. David Lapen, thank you for your confidence in me and for sharing your vision of creating impactful science; I have always been able to count on your support. I also want to thank Dr. Michael Sawada, from whom I gained foundational skills in coding and GIS; your attention to detail has been instrumental in my growth. Thank you to Dr. Chuiqing Zeng for your critical feedback and encouragement, which motivated me throughout my research. A special thanks to Dr. Simon Bélanger for your insightful comments during the thesis evaluation.

I sincerely thank everyone who helped with field data collection for Chapter 3: Dr. David Lapen, Emilia, Mark, Tessa, Yiwen, Zhewen, Neve, Kaiyi, and Rongkai. A heartfelt thank you goes to Emilia for your exceptional help with instrument calibration, water quality sampling, and the meticulous planning of field trips. Your hard work and countless behind-the-scenes efforts made all the difference.

Throughout the journey, I benefited tremendously from discussions with Shun Bi, Alexandre Castagna, John Hedley, Nima Pahlevan, Quinten Vanhellemont, Mohsen Ansari, and participants of the Ocean Optics journal club, especially Anna who volunteers her time to organize the discussions.

To Kady, Betsy, and Dr. Michael Sawada, thank you for your guidance and trust during my time at the Ottawa Neighbourhood Study; it marked the beginning of my professional career. Wish, your mentoring, especially in writing, had a profound impact on me; I was a really bad student before I met you. I am profoundly grateful to Dr. Karen Richardson, Dr. Emmanuel Devred, Dr. Stephen Bird, Marlow, Adam, and Jordi for your guidance and mentoring; I thoroughly enjoyed working with you. I also extend my wholehearted thanks to the members of Dr. Jeremy Kerr and Dr. Jules Blais's labs, especially Peter and Cynthia, for opening the door to research for me. Meredith and Jennifer, your workshop has been incredibly helpful! I deeply appreciate Dr. Kaley

Walker for the Atmospheric Radiative Transfer and Remote Sounding course, which greatly enhanced my understanding of Earth observation.

I am grateful to the SWEOLers, Andrew, Chris, Claudia, Gabby, Galen, Gen, Kaiqi, Kiyomi, Kutalmis, Lakmal, Marie-Bé, Matus, Mohsen, Neve, Rose, Ryleigh, Sarah, Sher, Souleymane, and Yiwen, for exchanging ideas, giving feedback, and the camaraderie. I thank friends I met through GGSA and in the GEG department: Adam, Amir, Ayshan, Benoît, Brandon, Brittany, Camille, Celeste, Connor, Domynik, Efe, Erika, Hugo, Ian, Jamie, Kethra, Louis, Marie-Lore, Nathaniel, Negar, Pénélope, Razi, Shannon, Sydney, and Zhewen (and the SWEOLers above!); the journey would not have been so enjoyable without you. Many thanks go to the members of Dr. Koreen Millard's lab, especially Elisha, for hanging out and sharing expertise. To my TTMLIS friends, I am thankful for the decades of unwavering friendship. I express my appreciation to friends and colleagues in the ocean optics community, everyone I have played basketball with, and Galen, Zi'ang, Mingjia, and Chenghan for being incredible buddies. I am also grateful to the city of Ottawa and the University of Ottawa, which have been my home and academic haven for the past decade.

Lastly, I would like to thank my parents, my brother, and all members of the Wu/Tang families for your unreserved love and support.

Table of contents

Table of contents

Abstract.....	ii
Acknowledgements.....	iii
Table of contents	v
List of figures	vii
List of tables.....	ix
Introduction.....	1
Chapter 1: Topography-adjusted Monte Carlo simulation of the adjacency effect in remote sensing of coastal and inland waters.....	3
1.1 Introduction	4
1.2 Methods	7
1.2.1 Propagation of radiation in the atmosphere	7
1.2.2 Surface reflection	9
1.2.3 Acceleration of computation.....	11
1.3 Validation.....	13
1.3.1 Comparison to libRadtran	13
1.3.2 Comparison to 6S.....	16
1.4 Case studies	17
1.4.1 Case Study 1: NIR reflectance of lakes in Minnesota.....	17
1.4.2 Case study 2: transects of NIR reflectance	20
1.4.3 Case study 3: surface-reflected light of ocean water in Hawaii.....	21
1.5 Discussion	25
1.5.1 Model accuracy	25
1.5.2 Contribution to aquatic remote sensing	26
1.5.3 Case studies	27
1.5.4 Installation and uses of T-Mart.....	29
1.5.5 Future development.....	29
1.6 Conclusion.....	30
1.7 Appendix A. Surface reflectance of water.....	31
1.8 Appendix B. Modeled TOA reflectance of lakes as a function of AOT and wind speed	34
Chapter 2: Sensor-generic adjacency-effect correction for remote sensing of coastal and inland waters	35
2.1 Introduction	36
2.2 Methods	39
2.2.1 Adjacency-effect correction.....	40
2.2.2 Calculation of the atmospheric point-spread function	46
2.2.3 Validation	47
2.3 Results	53
2.3.1 Performance overview	53
2.3.2 Scatterplot comparison and additional results	55
2.3.3 Example matchups	57

Table of contents

2.4 Discussion	59
2.4.1 Improvement across AC processors.....	59
2.4.2 Benchmark with another method	60
2.4.3 Variability of correction results with distance.....	60
2.4.4 Implications.....	61
2.4.5 Outlook.....	62
2.5 Conclusion.....	64
2.6 Supplementary materials	66
Chapter 3: Accuracy and limitations of optical remote sensing for water quality of small rivers: a case study of two rivers in Eastern Ontario, Canada	83
3.1 Introduction	84
3.2 Methods	84
3.2.1 Field and satellite data.....	84
3.2.2 Atmospheric correction.....	87
3.2.3 Water quality retrieval.....	87
3.2.4 Performance metrics	89
3.2.5 Forward modelling	89
3.3 Results	90
3.3.1 Atmospheric correction.....	90
3.3.2 Water quality retrieval.....	92
3.3.3 Forward modelling	96
3.4 Discussion	97
3.4.1 Atmospheric correction.....	97
3.4.2 Water quality retrieval.....	97
3.5 Conclusion.....	99
Conclusion	100
References.....	102

List of figures

Fig. 1.1. Illustration of a photon incident on a triangulated surface.....	9
Fig. 1.2. a) Diffuse downwelling irradiance at surface level normalized to total irradiance at TOA, and b) bihemispherical reflectance at TOA, both as a function of molecular-scattering optical thickness at selected solar zenith angles.....	15
Fig. 1.3. % Differences between T-Mart and libRadtran DISORT in calculated a) diffuse downwelling irradiance at surface level normalized to total irradiance at TOA and b) bihemispherical reflectance at TOA	16
Fig. 1.4. TOA reflectance of a Lambertian surface for a) AOT = 0 and surface albedo = 0.1 and b) AOT ₅₅₀ = 0.5 and surface albedo = 0.5.	17
Fig. 1.5. Observed TOA reflectance (band 8 of Sentinel-2 MSI, centered at 833 nm) of Lakes near Brainerd.....	18
Fig. 1.6. Modeled and observed TOA reflectance (band 8 of Sentinel-2 MSI, centered at 833 nm) of Lake centroids near Brainerd,.....	19
Fig. 1.7. a) Transects across Lake Edward, Minnesota, and b) the observed TOA reflectance (band 8 of Sentinel-2 MSI, centered at 833 nm).....	20
Fig. 1.8. Modeled and observed TOA reflectance (band 8 of Sentinel-2 MSI, centered at 833 nm) along a) west-east and b) north-south transects of Lake Edward	21
Fig. 1.9. Effective surface reflectance as a function of wind speed from 400 to 800 nm.	23
Fig. 1.10. Effective surface reflectance as a function of wind speed and AOT from 400 to 800 nm	24
Fig. 1.11. a) Sky remote-sensing reflectance simulated at various AOTs and from Lee et al. (2010)'s measurements, and b) modeled total atmospheric transmittance at various AOTs.....	25
Fig. 2.1. Illustration of the removal of the adjacency effect from TOA reflectance.	43
Fig. 2.2. Example atmospheric optical properties and atmospheric point-spread function (PSF) at 400 nm.	46
Fig. 2.3. Geographical distribution of 212 matchups from the GLORIA dataset within 200 m of shorelines and with Sentinel-2 or Landsat 8 overpasses.....	48
Fig. 2.4. Number of <i>in situ</i> measurements coinciding with Sentinel-2 and Landsat 8 overpasses as a function of distance to shore.....	49
Fig. 2.5. Example of shifting values to include negative values in the calculation of β and ε	52
Fig. 2.6. Performance metrics with and without adjacency-effect correction, grouped by atmospheric correction processor and band wavelength.	54
Fig. 2.7. Satellite-derived water-leaving reflectance, with and without adjacency-effect correction, compared with <i>in situ</i> values.	57
Fig. 2.8. Distribution of retrieved aerosol optical thickness at 550 nm.....	57

List of figures

Fig. 2.9. Examples of the impact of adjacency-effect correction on TOA reflectance and water-leaving reflectance derived by three atmospheric correction processors.....	58
Fig. 2.10. Improvement in RMSE following AE correction for matchups at 200 m distance intervals from shore.	61
Fig. 3.1. Locations of <i>in situ</i> water quality and reflectance data collected in the South Nation River and the Ottawa River in 2023.	85
Fig. 3.2. Shifted water-quality-measurement locations to test the impact of residual nearshore effects.	89
Fig. 3.3. Performance metrics without and with adjacency-effect correction, grouped by wavelength.	90
Fig. 3.4. Satellite-derived water-leaving reflectance compared with <i>in situ</i> values, without and with adjacency-effect correction.	91
Fig. 3.5. Comparison of ACOLITE-derived and MERRA2 AOT ₅₅₀ values.	92
Fig. 3.6. Satellite-derived water-leaving reflectance at four water-quality sites, used as input to bio-optical algorithms, alongside coincident <i>in situ</i> water quality measurements.	93
Fig. 3.7. Evaluation of satellite-derived water quality parameters against <i>in situ</i> values.....	95
Fig. 3.8. Simulated water-leaving reflectance with various concentrations of WQ parameters (median ± 2 SD).....	96

List of tables

Table 1.1. Symbols and definitions of radiometric quantities used in this article.	6
Table 2.1. Symbols and acronyms used in this article.	39
Table 2.2. Sample size of matchups with and without adjacency-effect correction	48
Table 2.3. Percentage reduction of performance metrics with the implementation of adjacency-effect correction	55
Table 2.4. Scene IDs and AOT ₅₅₀ used in adjacency-effect correction for the examples shown in Fig. 2.9.	59
Table 3.1. Satellite overpasses with coincident <i>in situ</i> reflectance measurements in 2023.	85
Table 3.2. Satellite overpasses with coincident <i>in situ</i> water quality measurements in 2023.....	86
Table 3.3. Water quality retrieval algorithms.	88
Table 3.4. Same as Fig. 3.3 but presenting the numerical values and the percentage reductions.91	
Table 3.5. Overview of water-quality-retrieval algorithms and their performances.....	94
Table 3.6. Median and SD of <i>in situ</i> WQ measurements.....	96

Introduction

In optical remote sensing, the adjacency effect (AE) refers to the influence of light reflected by adjacent areas on a target's spectral signal through atmospheric scattering (Tanré et al., 1987). The AE occurs when light from nearby objects, such as land and clouds, with a spectral shape and magnitude different from the target waterbody, is scattered by atmospheric molecules and particles into the path between the target and the sensor, ultimately reaching the sensor. This effect modifies the at-sensor radiance observed over the target, reducing the spectral contrast between the target and its surrounding area.

At-sensor radiance is the input to atmospheric correction (AC), which in aquatic remote sensing describes the conversion of at-sensor radiance into the corresponding sea-level water-leaving radiance or reflectance, and this requires accurate estimation of various atmospheric and surface-reflectance parameters (Mobley et al., 2016). The modified at-sensor radiance from the AE in nearshore environments therefore compromises the accuracy of AC. Since the output of AC serves as input to bio-optical algorithms that derive aquatic products, such as water turbidity, chlorophyll-a (Chl-a) and organic-matter concentrations, bathymetry, and bottom-habitat classification (Giardino et al., 2019; Kutser et al., 2020), any error introduced by the AE directly affects the quality of these products.

The AE is commonly observed over nearshore waters in the near-infrared (NIR) wavelengths, in which adjacent vegetated land is typically much more reflective than water and atmospheric scattering is dominated by the strong forward scattering of aerosols (Sterckx et al., 2011). Several studies have documented abnormally high NIR reflectance over these waters using airborne and spaceborne sensors, attributable to the AE (Kuhn et al., 2019; Odermatt et al., 2008; Pan et al., 2022; Reinersman and Carder, 1995; Sterckx et al., 2011). This heightened NIR reflectance near vegetative areas can disrupt algorithms used for deriving aerosol optical thickness (AOT) in AC, often leading to overestimated AOT and consequently overcorrection of surface reflectance in visible wavelengths (Hieronymi et al., 2023). Separating NIR contributions from the AE and water itself therefore becomes critical for effective AC and bio-optical modelling, especially in highly productive waters with non-negligible reflectance in NIR bands (Wang and Shi, 2005).

Despite its significant impacts, the AE is often overlooked in standard AC schemes and operational processing of satellite imagery in aquatic remote sensing (Frouin et al., 2019). Considering the sensitivity of aquatic remote sensing products to even minor sources of noise, the evaluation and correction of AE are essential in advancing aquatic remote sensing from the open ocean to nearshore waters (Bulgarelli and Zibordi, 2018).

To address the impact of the AE in remote sensing of nearshore environments, this thesis is structured around the following research questions:

- 1) How can the AE be accurately characterized for satellite imagery used in nearshore aquatic remote sensing?
- 2) How can the AE be corrected for to improve the accuracy of nearshore aquatic remote sensing products?
- 3) To what extent does correcting for the AE improve the accuracy of these products?

Introduction

This thesis is structured in an article-based format, with each chapter designed as a stand-alone paper for publication in academic journals. The chapters are outlined as follows:

Chapter 1: AE modelling (Wu et al., 2023)

- Title: Topography-adjusted Monte Carlo simulation of the adjacency effect in remote sensing of coastal and inland waters
- Co-authors: Anders Knudby, David Lapan
- Published in *Journal of Quantitative Spectroscopy and Radiative Transfer*; DOI: 10.1016/j.jqsrt.2023.108589
- This chapter presents the mechanisms and example applications of a Monte Carlo-based radiative transfer model, T-Mart. The model allows for characterization of the AE in custom environments and establishes a framework for AE correction.

Chapter 2: AE correction (Wu et al., 2024)

- Title: Sensor-generic adjacency-effect correction for remote sensing of coastal and inland waters
- Co-authors: Anders Knudby, Nima Pahlevan, David Lapan, Chuiqing Zeng
- Published in *Remote Sensing of Environment*; DOI: 10.1016/j.rse.2024.114433
- Building on the modelling work, this chapter derives equations for AE correction and validates the correction using globally distributed publicly available *in situ* reflectance data.

Chapter 3: AE correction for regional water quality monitoring (in preparation)

- Title: Accuracy and limitations of optical remote sensing for water quality of small rivers: a case study of two rivers in Eastern Ontario, Canada
- This chapter assesses the impact of AE correction on atmospheric correction for small waterbodies, including the South Nation River and the Ottawa River, evaluates downstream water quality products, and explores the limitations of aquatic remote sensing in the study area.

Note: the published Chapters 1 and 2 follow US spelling, while the rest of the thesis follows Canadian spelling.

Chapter 1: Topography-adjusted Monte Carlo simulation of the adjacency effect in remote sensing of coastal and inland waters

Yulun Wu^a, Anders Knudby^a, David Lapen^b

^aDepartment of Geography, Environment and Geomatics, University of Ottawa, Ottawa, Canada

^bOttawa Research and Development Centre, Agriculture and Agri-Food Canada, Ottawa, Canada

Abstract

We present a Monte Carlo radiative transfer (RT) code that simulates the top-of-atmosphere (TOA) reflectance of waterbodies considering the adjacency effect. The code is the first open-source tool that supports modeling of the adjacency effect with arbitrary topography. It uses the same atmospheric and aerosol settings as 6S, along with user-input surface reflective properties and topography, allowing users to transition from 1D to 3D RT modeling and characterize the adjacency effect in their study areas. The calculation of radiometric quantities was validated against libRadtran, showing a maximum difference lower than 0.6 % in extreme optical settings. Examples of the use of the code are presented in three case studies where modeled and measured radiative properties align with each other. One case study shows that 83.7 % of the variance in the near-infrared TOA reflectance of 47 lakes in Minnesota was explained by the adjacency effect, emphasizing the significance of the adjacency effect to atmospheric correction algorithms that use near-infrared bands to retrieve aerosol and glint information. Another case study supports the finding of strong wavelength dependence of the effective sea-surface reflectance in above-water measurements of remote sensing reflectance. The code will support physics-based methods that remove the adjacency effect in atmospheric correction processes, and it has the potential to improve satellite-based monitoring of coastal and inland waterbodies.

Keywords: radiative transfer; aquatic remote sensing; adjacency effect; atmospheric correction; coastal waters; inland waters

DOI: 10.1016/j.jqsrt.2023.108589

1.1 Introduction

In optical remote sensing, the adjacency effect is the distortion of the target's spectral signal due to atmospheric scattering when observing spectrally heterogeneous surfaces. The adjacency effect reduces the contrast between neighboring pixels with different reflectances, and it is commonly observed in remote sensing of coastal and inland waters where water tends to have a lower reflectance than nearby vegetation, especially in the near-infrared (NIR) wavelengths. Water can also be subject to adjacency effects produced by nearby sea ice (Bélanger et al., 2007) and clouds (Feng and Hu, 2016).

The adjacency effect is detectable on water pixels for common ocean-color sensors for as far as 36 km from the coast (Bulgarelli and Zibordi, 2018), and is even more significant in remote sensing of small inland waterbodies such as rivers where, compared to coastal environments, a greater proportion of the neighboring pixels are non-water objects. The adjacency effect often leads to failed isolation of the water-leaving portion of the top-of-atmosphere (TOA) reflectance, undermining the accuracy of retrieved water properties (Sterckx et al., 2011). While a few studies investigated methods that correct for the adjacency effect (Sei, 2015; Sterckx et al., 2011; Vermote et al., 1997b), most ocean-color data processors assume a homogenous underlying surface (Antoine and Morel, 1999; Mobley et al., 2016). The approach taken by Sei (2015) and Vermote et al. (1997b) calculates an azimuthally symmetric point-spread function of the environmental radiance of a Lambertian (i.e., isotropically reflecting) surface prior to atmospheric correction. This does not apply to off-nadir observations that are common in aquatic remote sensing to avoid sun glint; water's specular reflectance is also not considered in this approach. On the other hand, the SIMilarity Environment Correction approach (SIMEC) (Sterckx et al., 2011) assumes that water's spectral shape in the NIR range is stable for a wide range of water biophysical properties. SIMEC iteratively removes a small portion of the average land reflectance in the scene from the reflectance of water pixels until the pixels follow the predetermined spectral shape. However, at least two bands in red-edge and NIR wavelengths are required to fit the spectral shape, limiting its application to sensors with such bands. In addition, bottom reflectance in shallow waters, extreme turbidity, algal blooms, or sun glint, can significantly change water's reflectance from the predetermined spectral shape, reducing the effectiveness of SIMEC. A fully physics-based adjacency-correction method will likely overcome these challenges and improve aquatic remote sensing of coastal and inland waters; such an approach requires accurate characterization of the adjacency effect through radiative transfer (RT) modeling.

Various techniques have been developed to solve RT problems for aquatic applications, such as the discrete-ordinate method used in libRadtran (Emde et al., 2016), the successive-orders-of-scattering method used in 6S (Vermote et al., 1997b) and Zhai et al. (2010), and the invariant-imbedding techniques used in HydroLight (Hedley and Mobley, 2019). However, when considering arbitrary boundary geometry and significant multiple scattering, and with an arbitrary distribution of optical properties within the media, these techniques become insufficient and Monte Carlo methods often become the only feasible option (Gordon, 1985). It should be noted that 6S supports simple adjacency modeling but only for circular and isotopically reflecting objects, which does not apply to inland and coastal aquatic remote sensing. To model such complex environments, the Monte Carlo approach is used in this study.

Bulgarelli et al. (2014) used the Monte Carlo approach to model the adjacency effect in a coastal environment. A fixed atmospheric profile with molecular and aerosol optical properties was implemented, flat land and water surfaces were assumed, and the wind-induced rough sea surface was modeled through an analytical expression.

This study expands Bulgarelli et al. (2014)'s work to include a rich library of atmosphere and aerosol profiles from 6S and consider arbitrary three-dimensional (3D) topography to characterize coastal environments such as fjords, cliffs, and hilly terrains. The widely used Cox-Munk wave-slope statistics (Cox and Munk, 1954) were used to characterize water surfaces, and arbitrary solar-target-viewing geometry is supported. The RT code was developed in Python and was named Topography-adjusted Monte-carlo Adjacency-effect Radiative Transfer code (T-Mart); it allows RT modeling in a coupled 3D ocean-atmosphere system in diverse environmental conditions with arbitrary boundary geometry. The full code and instructions of T-Mart can be found on <https://github.com/yulunwu8/tmart>.

This article is structured as follows. Section 1.2 describes the environmental settings and the calculations of radiometric quantities in T-Mart, followed by validation of the code's accuracy in Section 1.3. Modeled and measured radiative properties are compared in three case studies to further validate and demonstrate the use of the code in Section 1.4, two of which investigate the contribution of the adjacency effect and one highlights the surface-reflected light off clear ocean water. The case studies and the installation, use, and accuracy of the code are discussed in Section 1.5.

Chapter 1: Adjacency effect modelling

Table 1.1. Symbols and definitions of radiometric quantities used in this article.

Symbol	Definition	Unit
AOT_{550}	Aerosol optical thickness at 550 nm	-
τ_{ext}	Optical thickness for extinction (sum of scattering and absorption)	-
τ_{scat}	Optical thickness for scattering	-
τ_{abs}	Optical thickness for absorption	-
T_{abs}	Direct transmittance for absorption	-
R	Hemispherical-directional reflectance, ratio of radiance ($\text{W sr}^{-1} \text{ m}^{-2}$) multiplied by π to downwelling irradiance (W m^{-2})	sr^{-1}
R_{dir}	Direct reflectance	sr^{-1}
R_{env}	Environmental reflectance	sr^{-1}
R_{atm}	Atmospheric intrinsic reflectance	sr^{-1}
R_{surf}	Reflectance of land or water surface	sr^{-1}
R_{water}	Reflectance of water (surface and water-leaving)	sr^{-1}
R_{glint}	Reflectance of sun glint and sky glint	sr^{-1}
ρ	Bihemispherical reflectance, ratio of upwelling irradiance (W m^{-2}) to downwelling irradiance (W m^{-2})	-
ρ_{surf}	Reflectance of land or water surface	-
ρ_{water}	Reflectance of water (surface and water-leaving)	-
ρ_{TOA}	Reflectance of the entire atmosphere-land-ocean system at the top of the atmosphere	-
$\rho_{\text{water-leaving}}$	Normalized above-surface water-leaving reflectance	-
ρ_{Fresnel}	Specular or Fresnel reflectance	-
ρ_{whitecap}	Whitecap reflectance	-
E_u	Upwelling irradiance	W m^{-2}
E_d	Downwelling irradiance	W m^{-2}
E_d^{diff}	Diffuse downwelling irradiance	W m^{-2}
L_t	Total upwelling radiance (surface and water-leaving)	$\text{W sr}^{-1} \text{ m}^{-2}$
L_w	Water-leaving radiance	$\text{W sr}^{-1} \text{ m}^{-2}$
L_{sky}	Sky radiance	$\text{W sr}^{-1} \text{ m}^{-2}$
L_{sr}	Surface-reflected radiance	$\text{W sr}^{-1} \text{ m}^{-2}$
r	Effective sea-surface reflectance, ratio of L_{sr} to L_{sky}	-
R_{rs}	Remote-sensing reflectance of water, ratio of L_w to E_d	sr^{-1}
T_{rs}	Total remote-sensing reflectance, ratio of L_t to E_d	sr^{-1}
S_{rs}	Sky remote-sensing reflectance, ratio of L_{sky} to E_d	sr^{-1}

1.2 Methods

A Monte Carlo RT code, T-Mart, was developed in Python to simulate photons' propagation and attenuation from the TOA to Earth's surface and back to the TOA. Collimated solar irradiance is the light source and a sensor is placed at an arbitrary point in 3D space. A backward Monte-Carlo approach (Mayer et al., 2010) was implemented to speed up computation, i.e., photons are released from the sensor and collected at the light source. A pre-specified number of photons (N_{photon}) are launched into the atmosphere, and they are scattered, reflected, and attenuated according to their propagation paths and the optical properties of the media and the reflecting surfaces. Photons are tallied when they exit the TOA to infer the optical properties of the atmosphere-land-ocean system.

T-Mart limits its scope to wavelengths between 0.4 and 1.65 μm , where the spectral dependence of whitecap reflectance is known ([Appendix A4](#)). This meets the requirements for ocean color remote sensing, which relies mostly on visible and NIR wavelengths (Dierssen et al., 2021). Clouds and polarization are not implemented in T-Mart and are not considered in this study.

1.2.1 Propagation of radiation in the atmosphere

By default, the modeled atmosphere in T-Mart is divided into 20 horizontally homogeneous layers. The absorption and scattering properties of each layer are defined by its aerosol and molecular composition, and these optical properties were imported from 6S to T-Mart through the Py6S interface (Wilson, 2013). Six aerosol models from 6S were included: continental, maritime, urban, desert, biomass burning, and stratospheric. Each model has its unique spectral extinction coefficient, scattering albedo, asymmetry parameter, and scattering phase function. There were also six atmosphere models from 6S: midlatitude summer, midlatitude winter, subarctic summer, subarctic, tropical, and U.S. standard. Each of them has a specified vertical distribution of water vapor and ozone. The concentration of aerosols and other molecules in each atmospheric layer is determined by pre-specified scale heights. By default, the scale heights are 8 km for molecules and 2 km for aerosol particles following 6S (Vermote et al., 2006).

A photon's movement starts with a specified initial position and an initial direction. Once the photon is released, an optical thickness for scattering (τ_{scat}) is sampled following Mayer (2009),

$$\tau_{\text{scat}} = -\ln(\mathfrak{R}) \quad (1.1)$$

where \mathfrak{R} is a random number evenly distributed between 0 and 1. The symbols and definitions of radiometric quantities used in this article are summarized in Table 1.1. An end position of this straight-line movement is then determined by integrating the scattering coefficient along the propagation direction until reaching the τ_{scat} determined by Eq. (1.1):

$$\tau_{\text{scat}} = \sum_{\text{layers}} l_i \cdot k_{\text{scat} i} \quad (1.2)$$

where l_i is the length that the photon travels in layer i , and $k_{\text{scat}\,i}$ is the scattering coefficient of that layer. This essentially stacks the layers in the photon's direction of propagation and determines the number of layers it takes to "consume" the sampled τ_{scat} . It should be noted that because of the random nature of \mathfrak{R} , the end position is rarely at the boundary between two atmospheric layers.

There are three possible scenarios after the photon's movement:

- 1) The end position is below Earth's surface. In this case, the intersecting point between the surface and the straight line formed by the movement's initial and end positions is located, and the intersecting point is used as the new initial position for the next movement (Section 1.2.2).
- 2) The end position is above the TOA. In this case, the simulation for this photon is ended and radiometric quantities are calculated (Section 1.2.3.2). New photons are then launched until the specified N_{photon} is reached.
- 3) The end position is in the atmosphere. A scattering mode (either aerosol or Rayleigh scattering) is sampled using the ratio of the two scattering coefficients (Mayer, 2009). A new propagation direction is then determined according to the scattering phase function of the sampled scattering mode.

The absorption of light in the atmosphere is simulated through a weight system (Mobley, 1994). The photon carries a weight of 1 when it enters the atmosphere, and the weight changes according to the path of the photon's movement, the absorption coefficients of the atmospheric layers, and the reflective properties of the surfaces.

Regardless of the three scenarios above, an absorption optical thickness is calculated similarly to Eq. (1.2) for the photon's movement,

$$\tau_{\text{abs}} = \sum_{\text{layers}} l_i \cdot k_{\text{abs}\,i} \quad (1.3)$$

where $k_{\text{abs}\,i}$ is the absorption coefficient of layer i . For movements that stopped before "consuming" the entire sampled τ_{scat} (scenarios 1 and 2 above), τ_{abs} is calculated from the initial position only to the intercepting point at TOA or the surface. Next, the direct transmittance for absorption can be calculated as

$$T_{\text{abs}} = e^{-\tau_{\text{abs}}} \quad (1.4)$$

following Liou (2002). The attenuation of radiation as it travels through the medium is simulated by modifying the photon's weight (w),

$$w = w_0 \cdot T_{\text{abs}} \quad (1.5)$$

where w_0 is the photon's weight before the movement. The history of a photon's scattering and reflection events is recorded throughout its movements to differentiate the various components of TOA reflectance (Section 1.2.3.2).

1.2.2 Surface reflection

1.2.2.1 Definitions of reflectances in T-Mart

Two types of reflectances are described throughout this article, defined following Schaepman-Strub et al. (2006). Bihemispherical reflectance (ρ , unitless) describes the ratio of the radiant flux leaving a surface or medium to the incident radiant flux. Hemispherical-directional reflectance (R , sr^{-1}) describes the ratio of reflected radiant flux per unit solid angle surrounding a given direction, multiplied by π , to the incident radiant flux from the entire hemisphere. A Lambertian surface has the same numerical value for ρ and R . In optical remote sensing applications, R is usually used because of the difficulty of collecting reflected radiant flux toward the entire hemisphere.

1.2.2.2 Surface triangulation and reflectance

When the line formed by a photon's movement intersects the modeled land or water surface, the photon is reflected from the point of intersection (Fig. 1.1) and a new weight of the photon is calculated by multiplying the initial weight by the bihemispherical reflectance of the surface (ρ_{surf}) following Mayer (2009). On land, the pixels of a digital elevation model (DEM) are connected to form 3D triangles to model RT in complex topography and the impact of elevation and landscape morphology on TOA reflectance. When a photon intercepts the triangulated surface, a new direction of propagation is sampled following the reflective properties of the surface, and the new direction is tilted to the surface normal of the triangle (Fig. 1.1).

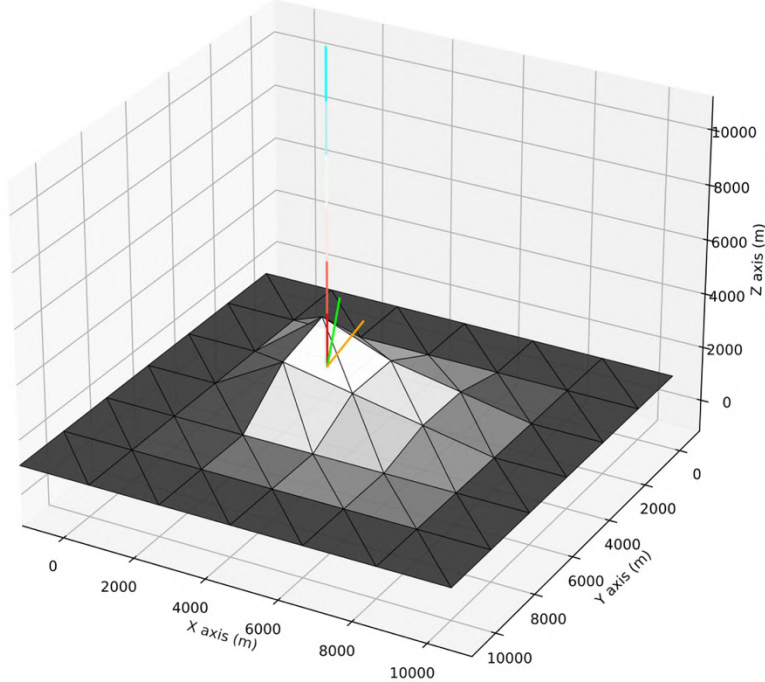


Fig. 1.1. Illustration of a photon incident on a triangulated surface. The photon moves from the blue end to the red end of the vertical line and intersects the triangulated pixel below. The green line intersecting the same point is the surface normal of the triangle. The orange line is the sampled reflected direction of a Lambertian surface tilted to the surface normal; it is also the new direction of propagation in the photon's next movement.

For every photon movement, the line formed by the movement is tested for intersection with the triangles. If a photon reaches the surface outside the DEM, it is reflected by the background surface. The background surface extends horizontally to infinity, and it is divided into two sections separated by a straight line. Each background section is a homogeneous land or water surface with a specified reflectance, to facilitate the modeling of coastal environments where both terrestrial and aquatic background reflectances are needed.

A few standard reflectance spectra were incorporated in T-Mart, including dry beach sand, wet beach sand, conifer forest, and lawn grass from the USGS Spectral Library (Kokaly et al., 2017), and three water spectra calculated by HydroLight with chlorophyll concentrations of 0.1, 1 and 10 mg/m³. The normalized water-leaving reflectance ($\rho_{\text{water-leaving}}$, unitless), defined as the measured reflectance with a nadir-viewing sensor and the sun at the zenith in the absence of atmospheric attenuation (Morel and Gentili, 1996), was used and it was calculated by multiplying the HydroLight-calculated remote sensing reflectance (R_{rs} , sr⁻¹) by π in the above-described environment (Mobley, 2022). In addition, users can manually specify the reflectance spectra of custom surfaces.

1.2.2.3 Reflectance of water

Section 1.2.2.2 focused on how T-Mart models the reflective properties of surfaces in general. The reflectance of water in T-Mart is more complex and consists of three components: 1) user-specified $\rho_{\text{water-leaving}}$ just above the water surface, 2) specular or Fresnel reflectance (ρ_{Fresnel} , unitless), and 3) whitecap reflectance (ρ_{whitecap} , unitless). When a photon impinges on the modeled water surface, water's total bihemispherical reflectance (ρ_{water} , unitless) of the three components is calculated and is used to determine the weight of the photon after the reflection. The abovementioned bihemispherical reflectances of water are calculated as follows. For every water-reflecting event, the orientation of the surface is first sampled from the Cox-Munk slope distribution (Cox and Munk, 1954) to model the interface between the air and the water at an infinitesimally fine scale. The incidence angle is then calculated according to the surface orientation and the incoming direction of the photon. The Fresnel reflectance of water is calculated using the incidence angle and wavelength of the photon as well as water's salinity and temperature ([Appendix A3](#)). Then, ρ_{water} is calculated as the sum of whitecap-fraction-corrected ρ_{whitecap} , ρ_{Fresnel} and $\rho_{\text{water-leaving}}$,

$$\rho_{\text{water}}(\lambda) = F \cdot \rho_{\text{whitecap}}(\lambda) + (1 - F)[\rho_{\text{Fresnel}}(\lambda) + \rho_{\text{water-leaving}}(\lambda)] \quad (1.6)$$

where λ is the wavelength and F is the fraction of the sea surface covered by whitecaps (calculations of whitecap reflectance and fraction are presented in [Appendix A4](#)). Similar to how ρ_{surface} modifies the photon's weight, the weight of the photon is multiplied by ρ_{water} at the water reflection, but the photon has a probability of going through a specular reflection according to the ratio of whitecap-fraction-corrected ρ_{Fresnel} to ρ_{water} . Although the photon carries the same weight after the reflection regardless of the mode of reflection (specular or Lambertian), the photon's energy is conserved through sampling of moving directions. To summarize, T-Mart has two reflectance models: 1) Lambertian surfaces that reflect light isotopically and 2) specular reflectance following the Cox-Munk slope distribution and Fresnel's

equations. Note that the reflectance of water has both Lambertian and specular components: $\rho_{\text{water-leaving}}$ and ρ_{whitecap} are treated as Lambertian, and ρ_{Fresnel} is treated as specular.

1.2.3 Acceleration of computation

Monte Carlo methods come with inherent noise that can be reduced by increasing the sample size, which may lead to a long computation time (Buras and Mayer, 2011). One way to speed up computation is to use more computing units; the *multiprocessing* package in Python was used in T-Mart to utilize the multiple cores of personal computers. GPU acceleration will likely make this even faster due to GPUs' parallel-computation nature, but it was not implemented because it often requires specialized graphic cards and software environments which are difficult for users to maintain. In addition, the backward Monte Carlo (Section 1.2.3.1) and the local-estimate techniques (Section 1.2.3.2) were implemented in T-Mart to speed up computation. Currently, T-Mart processes one million photons in roughly 5 minutes on personal computers with eight-core processors. This translates to differences of less than 0.6 % compared to libRadtran in extreme optical conditions (Fig. 1.3). The standard error of Monte Carlo estimates is proportional to $N_{\text{photon}}^{-\frac{1}{2}}$ (Mobley, 1994), meaning that if we increase or decrease the computation time by a factor of 10, the precision is accordingly increased or decreased by a factor of $\sqrt{10}$.

1.2.3.1 Backward Monte Carlo technique

In forward Monte Carlo models, simulated photons are released from the light source and are collected by a simulated instrument at a specified location (Marchuk et al., 1980). In the field of aquatic remote sensing, the light source is the parallel solar irradiance incident on the TOA and the simulated sensor is located at a point on a satellite orbit. The problem with the forward approach is that the simulated sensor is often very small compared to Earth's atmosphere and ocean system. As a result, the probability of a photon intercepting the sensor is extremely low, making the modeling impractical or highly inefficient (Mobley, 1994). In addition, when simulating 3D scenarios, the area of the surface receiving photons cannot be determined in advance because this depends on the sun-sensor geometry and environmental conditions, such as the scattering properties of the atmosphere (Mobley, 1994).

Backward Monte Carlo models are often used to overcome the challenges in forward Monte Carlo modeling (Bulgarelli et al., 2014; Mayer et al., 2010; Reinersman and Carder, 1995). Instead of releasing the photons at the light source, backward models release photons at the sensor and trace them back to the light source. This approach overcomes the difficulties of releasing photons at a surface of unknown size and collecting photons at a very small target, and because almost all released photons are tallied, this also significantly improves computational efficiency (Mayer et al., 2010; Mobley, 1994). Backward Monte Carlo methods rely on the principle of reciprocity in radiative transfer (Light, 2003), i.e., the same amount of photons will be received at the sensor if the sensor and the light source switch places.

1.2.3.2 Calculating radiometric quantities

T-Mart can calculate both ρ and R (Section 1.2.2.1). The former does not consider the angular distribution of the reflected radiance but is important in determining the illumination conditions of the atmosphere and surfaces. The latter is more commonly used in remote sensing when the reflectance of a surface is derived by observing it from a single fixed sensor aperture.

T-Mart calculates ρ at the TOA or any elevation by counting the number of photons moving across a plane-parallel surface, weighted by the photons' weights and normalized to the initial number of photons (N_{photon}),

$$\rho = E_u/E_d = \frac{\sum_{\text{photon}} \sum_{\text{movement}} w}{N_{\text{photon}}} \quad (1.7)$$

where E_u is the upwelling irradiance (W m^{-2}) and E_d is the downwelling irradiance (W m^{-2}). As seen in Eq. (1.7), a photon can contribute to the irradiance or exitance at a certain level more than once through multiple movements or multiple scattering. As a result, photons reflected by the surface can be redirected to the surface again by molecules and aerosols in the atmosphere, reflecting the spherical albedo of the atmosphere (Vermote et al., 2006).

Next, R is calculated using the local-estimate technique (Marchuk et al., 1980). The local-estimate technique is analogous to creating a virtual photon at each collision (scattering or reflection) and forcing it to move toward the sensor, weighted by the photon's probability of scattering into the sensor's direction. At every collision, the probability of a photon scattering into the sensor's direction is calculated according to the scattering phase function at the collision, the remaining weight of the photon, and the extinction coefficient between the collision and the sensor (Mayer, 2009). The combined aerosol and molecular scattering phase function, weighted by the respective scattering optical thicknesses, is used when the collision happens in the atmosphere. Just like regular photons, the virtual photon is subject to extinction along its way to the sensor.

For a scattering event, the local-estimate weight, w_L , is calculated as part of the total reflectance,

$$w_L = w \cdot \frac{p(\theta_p) \cdot e^{-\tau_{\text{ext}}}}{\cos(\theta_v)} \quad (1.8)$$

where w is the photon's weight, θ_p is the angle between the sensor's direction and the photon's propagation direction before scattering, and the phase function $p(\theta_p)$ describes the probability that the scattered angle is θ_p . The extinction optical thickness (τ_{ext}) is the sum of τ_{scat} and τ_{abs} , and $e^{-\tau_{\text{ext}}}$ describes the direct transmittance for extinction between the collision point and the sensor. Last, θ_v is the viewing zenith angle and $\cos(\theta_v)$ accounts for the slant area of the target as viewed by the sensor.

For a reflection event, R_{surf} can replace $p(\theta_p)$ in Eq. (1.8) as the probability of a photon reflecting into the sensor's direction,

$$w_L = w \cdot \frac{R_{\text{surf}} \cdot e^{-\tau_{\text{ext}}}}{\cos(\theta_v)}. \quad (1.9)$$

For a photon's collision at a Lambertian surface, either R or ρ of the surface can be used as R_{surf} as there is no angular dependency. For a collision at a water surface, the bihemispherical-directional reflectance of water (R_{water} , sr $^{-1}$) replaces R_{surf} in Eq. (1.9), and it is calculated by replacing ρ_{Fresnel} in Eq. (1.6) with the hemispherical-directional reflectance of glint (R_{glint} , sr $^{-1}$),

$$R_{\text{water}}(\lambda) = F \cdot \rho_{\text{whitecap}}(\lambda) + (1 - F)[R_{\text{glint}}(\lambda) + \rho_{\text{water-leaving}}(\lambda)]. \quad (1.10)$$

The full calculation of R_{glint} is described in [Appendix A](#) for brevity. Lastly, R can be calculated as

$$R = \frac{\sum_{\text{photon}} \sum_{\text{movement}} w_L}{N_{\text{photon}}}, \quad (1.11)$$

and it can be further divided into three components following 6S (Vermote et al., 2006):

Direct reflectance (R_{dir} , sr $^{-1}$):	$n_{\text{scatter}} = 0$
Environmental reflectance (R_{env} , sr $^{-1}$):	$n_{\text{surface}} \geq 1$ and $n_{\text{scatter}} \geq 1$
Atmospheric intrinsic reflectance (R_{atm} , sr $^{-1}$):	$n_{\text{surface}} = 0$

where n_{surface} and n_{scatter} are respectively the numbers of surface reflections and scattering that happened to a photon. It should be noted that n_{scatter} resets to 0 each time a photon reaches a surface, because scattering events before the photon reaches the last surface are viewed as diffuse contributions to the surface irradiance. In other words, R_{dir} is from photons that travel from the target pixel to the sensor without being scattered (regardless of the photons' history before hitting the target pixel), R_{env} is from photons that travel from the non-target pixels to the sensor through scattering, and R_{atm} is from photons that never reached the surface of the Earth. Changes in R_{env} due to inhomogeneous surfaces are the basis of the adjacency effect.

1.3 Validation

T-Mart was validated against libRadtran and 6S, with a focus on the accuracy of the calculated radiometric quantities with libRadtran. Validation of T-Mart against 6S was conducted to test the results of the two models using the same atmospheric and aerosol settings.

1.3.1 Comparison to libRadtran

libRadtran (Emde et al., 2016) is a widely used software package for Earth-observation RT calculations. It is open-source and was written in Fortran and C. libRadtran supports the calculations of radiances, irradiance, and actinic fluxes given atmospheric and surface

parameters. Some of its applications include studying the radiative effects of greenhouse gases (Ehret et al., 2008) and aerosols from burning emissions (Saleh et al., 2015) and mapping the leaf area of seagrasses and their depth in the water (Hedley et al., 2016). Due to its versatility and wide use, libRadtran was used to validate the results produced by T-Mart.

There are six RT solvers in the publicly available version of libRadtran, each with its own specialties. MYSTIC and DISORT are among the most used solvers. Like T-Mart, MYSTIC is based on Monte Carlo random sampling. DISORT, the default solver of libRadtran, is based on the discrete-ordinates method which approximates RT by discretizing the infinite number of possible angles in a 3D space (Stamnes et al., 1988). MYSTIC has a 3D version that would ideally be used as the benchmark in this study due to its similar nature to T-Mart, but it is unavailable to the public and only a one-dimensional (1D) version is provided (Mayer et al., 2020). DISORT is therefore used as the benchmark for this comparison, provided that MYSTIC and DISORT produce almost identical results (Mayer, 2009) and DISORT does not have statistical noise from Monte Carlo simulations.

Validations of T-Mart against DISORT were run with molecular-scattering optical thicknesses from 0.05 to 0.5 in the absence of aerosols. This range is similar to the molecular-scattering optical thicknesses from 400 to 700 nm, which is approximately 0.4 at 400 nm and 0.04 at 700 nm. Although wavelengths and molecular-scattering optical thicknesses are highly correlated, optical thickness is used as the unit for comparison to show more gradual changes in calculated radiometric quantities. ρ_{surf} is set to 0.1 and τ_{abs} is set to 0.3 for all validation runs with libRadtran. It is worth noting that a τ_{abs} of 0.3 is quite an extreme value that is usually only found in the strong absorption bands. It is included here to highlight the possible differences in how the codes handle the absorptive properties of the atmosphere. Aerosol models in T-Mart were imported from 6S for continuity of past data processing (Section 1.5.2); they are slightly different from the ones in libRadtran therefore aerosols were not considered in this section.

Comparisons of diffuse downwelling irradiance at the surface (E_d^{diff} , W m^{-2}) and bihemispherical reflectance at TOA (ρ_{TOA} , unitless) were made. E_d^{diff} was included because the accuracy of the diffuse part of irradiance, rather than the direct part, depends on many factors in the RT calculations such as the modeled multiple scattering, atmospheric spherical albedo, and surface reflectance. Direct irradiance can be easily calculated through Beer's Law; it is not included as it is essentially the same across all RT models. The comparisons included ρ_{TOA} because it considers all steps of solar radiation entering the atmosphere, interacting with the surface, and exiting the TOA.

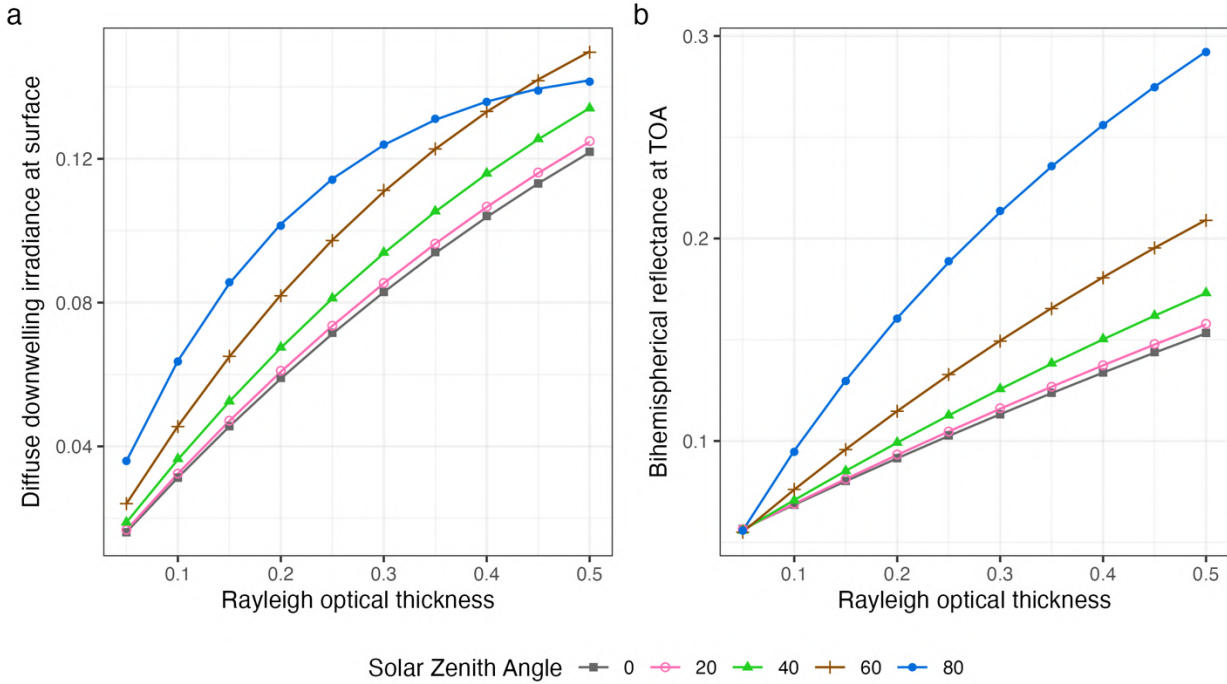


Fig. 1.2. a) Diffuse downwelling irradiance at surface level (E_d^{diff}) normalized to total irradiance at TOA, and b) bihemispherical reflectance at TOA (ρ_{TOA}), both as a function of molecular-scattering optical thickness at selected solar zenith angles. Lines are from libRadtran DISORT, and shapes are from T-Mart. Nadir viewing angle, $\rho_{\text{surf}} = 0.1$, $\tau_{\text{abs}} = 0.3$, and $N_{\text{photon}} = 1,000,000$ for T-Mart runs. The discrepancy between the lines and the shapes is almost unnoticeable here, but it is quantified in Fig. 1.3.

Both E_d^{diff} and ρ_{TOA} calculated by T-Mart and DISORT are very similar (Fig. 1.2). Their differences are calculated as

$$\% \text{ difference} = \frac{\text{Value}_{\text{T-Mart}} - \text{Value}_{\text{DISORT}}}{\text{Value}_{\text{DISORT}}} \times 100 \quad (1.12)$$

and the % differences at each solar zenith angle across optical thicknesses are presented in Fig. 1.3, with a maximum % difference of 0.59 %. The differences are smaller when τ_{abs} is lowered, as this reduces the noise in the Monte Carlo model; they are about five times smaller at a τ_{abs} of 0 compared to a value of 0.3 (not shown). The calculated radiometric quantities exhibit slight angular dependency (Fig. 1.3), likely due to the angular discretization in the discrete-ordinate method; while a Monte Carlo method calculates the exact angular solution, methods with angular discretization may produce larger errors from larger discretized angles.

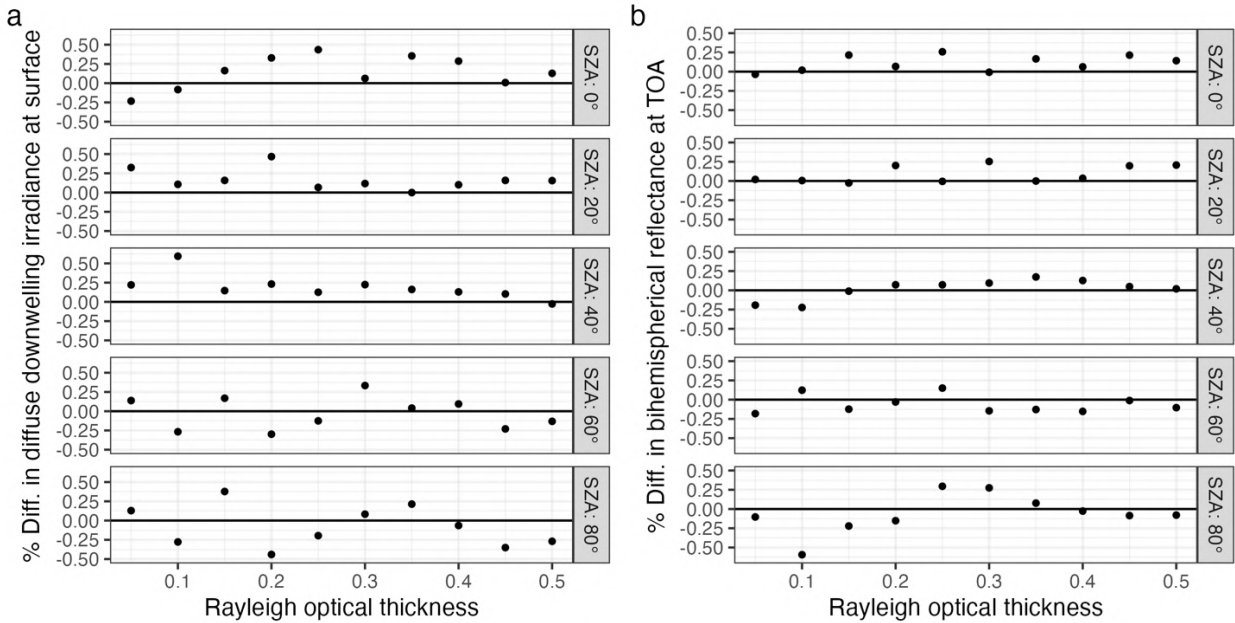


Fig. 1.3. % Differences between T-Mart and libRadtran DISORT in calculated a) diffuse downwelling irradiance at surface level (E_d^{diff}) normalized to total irradiance at TOA and b) bihemispherical reflectance at TOA (ρ_{TOA}), both as a function of molecular-scattering optical thickness at selected solar zenith angles. Nadir viewing angle, $\rho_{\text{surf}} = 0.1$, $\tau_{\text{abs}} = 0.3$, and $N_{\text{photon}} = 1,000,000$ for T-Mart runs.

1.3.2 Comparison to 6S

6S (Vermote et al., 1997b) is another RT code widely used in the remote-sensing community. It solves RT with the successive-order-of-scattering method. A comparison of reflectances calculated by T-Mart and 6S was made for a typical coastal environment with the “midlatitude summer” atmosphere and “maritime” aerosols in 6S. Two scenarios were run: 1) aerosol optical thickness (AOT) is 0.0 and surface albedo is 0.1, and 2) AOT at 550 nm (AOT_{550}) is 0.5 and surface albedo is 0.5. An AOT_{550} of 0.5 is quite extreme and is used here only to highlight the possible differences between the RT solvers. The solar zenith and viewing zenith angles were both 30° with a 90° relative azimuth angle, following a typical ocean-color observation (Mobley, 2022). R was broken down into R_{dir} , R_{env} , and R_{atm} (Section 1.2.3.2) in the comparison. Results from T-Mart and 6S for both scenarios generally align with each other, except at high-molecular-absorption wavelengths such as 760 nm (Fig. 1.4a and b). T-Mart tends to produce slightly lower R_{dir} and R_{env} and slightly higher R_{atm} at high-absorption wavelengths. For most purposes, these differences are not a major concern because i) they are relatively small, and ii) these wavelengths are usually avoided for aquatic remote sensing; however, caution should be taken for applications that make use of high-absorption wavelengths.

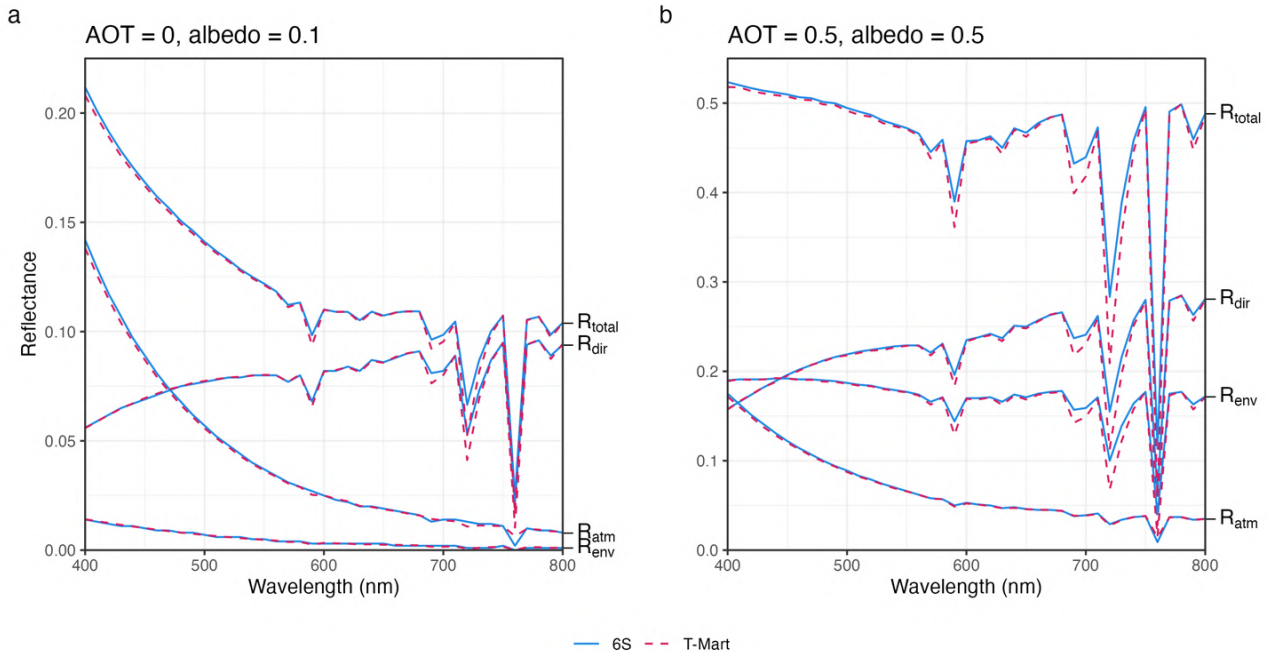


Fig. 1.4. TOA reflectance of a Lambertian surface for a) $\text{AOT} = 0$ and surface albedo = 0.1 and b) $\text{AOT}_{550} = 0.5$ and surface albedo = 0.5. Both results are produced with a mid-latitude summer atmosphere and maritime aerosols. Solar zenith and viewing zenith angles are both 30° , with a 90° relative azimuth angle. $N_{\text{photon}} = 1,000,000$ for T-Mart runs.

Overall, even in extreme absorption and scattering conditions, T-Mart produces results that are very similar to those from libRadtran DISORT (difference < 0.6 % when $N_{\text{photon}} = 1,000,000$), and it generally also aligns well with 6S, except at high-absorption wavelengths.

1.4 Case studies

1.4.1 Case Study 1: NIR reflectance of lakes in Minnesota

There are more than 11,000 lakes in Minnesota (Minnesota DNR, 2013), many of which were formed when glaciers moved back and forth across Minnesota during the last Ice Age. The lakes vary in size and provide an excellent opportunity to study the magnitude of the adjacency effect because small lakes are relatively more affected by the adjacency effect than larger lakes; lakes of different sizes may therefore exhibit a gradient of the impact of the adjacency effect.

Lakes 30 km northwest of Mille Lacs Lake (46.25N, 93.64W) were selected for this case study (Fig. 1.5). Two Sentinel-2 images (20200921T171021_20200921T172005_T15TVM and 20200921T171021_20200921T172005_T15TUM) were chosen, both acquired at 11:10 am local time on September 21, 2020. The lakes were in the middle of the two images, so a mosaic was created, and its average viewing geometry was used in the modeling (solar zenith: 47.35° , solar azimuth: 163.3° , viewing zenith: 4.95° , viewing azimuth: 145°). These images were chosen because 1) there were no significant breaking waves in the lakes and the wind was stable for an extended period of time, allowing the use of Cox-Munk's equations, 2) there were no clouds near the lakes, which could introduce additional adjacency effect (Feng and Hu, 2016), 3) the high

aerosol loading during the time of image acquisition produced a strong adjacency effect, and 4) the images were free of strong sun glint across all lakes.

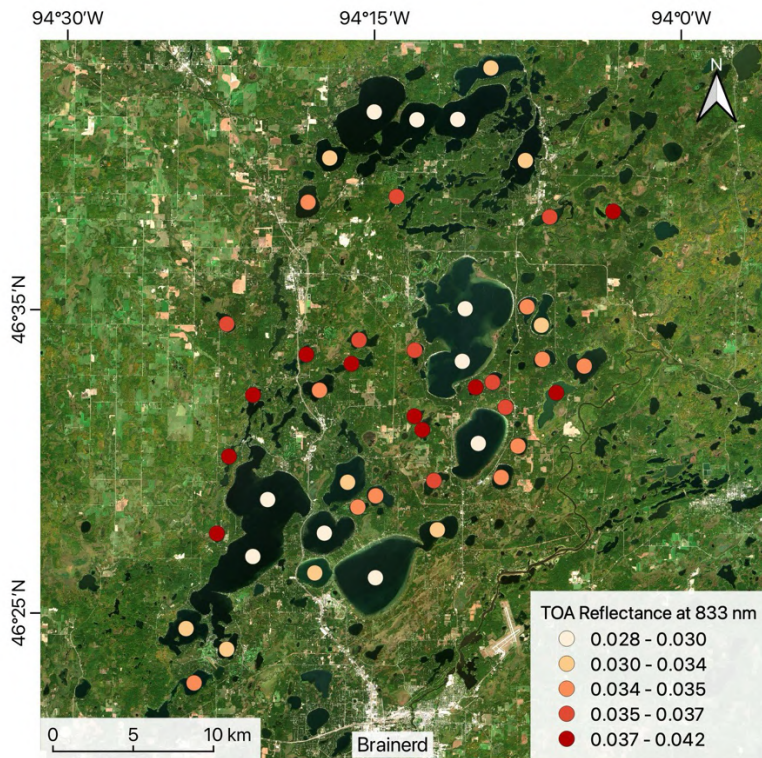


Fig. 1.5. Observed TOA reflectance (band 8 of Sentinel-2 MSI, centered at 833 nm) of Lakes near Brainerd, Minnesota on September 21, 2020.

The objective of this case study was to model the adjacency effect in T-mart and examine its contribution to the lakes' TOA reflectance in the NIR band of Sentinel-2 MSI (band 8, centered at 833nm). The NIR band was chosen because of its significance in aquatic remote sensing where it is often used in estimating the aerosol contribution in atmospheric correction of TOA images; the overestimated reflectance in NIR due to the adjacency effect can thus lead to overestimated AOT and underestimated reflectances in the visible wavelengths, with subsequent biases in the retrieved water optical properties (Moses et al., 2017).

The images were first imported to T-Mart. A water mask was applied to the scene using the Normalized Difference Water Index (NDWI) calculated as $(\text{band 3} - \text{band 8}) / (\text{band 3} + \text{band 8})$, and pixels with an NDWI greater than 0 were determined to be water upon visual examination. Based on water's high absorption in the NIR range, $\rho_{\text{water-leaving}}(833\text{nm})$ was assumed to be 0, an assumption we expect to hold except in extremely shallow or very turbid waters, where bottom reflectance or backscattering, respectively, may produce a small water-leaving signal at this wavelength (Moses et al., 2017; Werdell et al., 2018). The "midlatitude summer" atmosphere model and the "continental" aerosol model from 6S were used to characterize the atmosphere. An AOT₅₅₀ of 0.28 was used, and it was the average AOT₅₅₀ around the lakes derived by ACOLITE (Vanhellemont and Ruddick, 2018). ACOLITE was determined to be one of the best atmospheric correction processors for aquatic remote sensing of inland waters in an

intercomparison exercise (Pahlevan et al., 2021); it derives AOTs using the dark-spectrum-fitting technique which could utilize the shadows of ground-level objects in inland scenes, making it suitable to determine AOT_{550} in this case study. The surface reflectance of the land, an input to the model, was also retrieved in ACOLITE for consistency. A wind speed of 5 m/s was used based on the hourly weather history of Brainerd, Minnesota, a city located roughly 5 km away (www.wunderground.com, Fig. 1.5). An azimuthally averaged R_{glint} was used because the wind direction was unknown. ρ_{whitecap} was included but it was negligible with a wind speed of 5 m/s. The ground surface was assumed to be flat, as this part of Minnesota is largely a flat lowland. The pixels were resampled to 200 by 200 m resolution to speed up computation. A total of 47 lakes larger than 600 by 600 m were selected to avoid the “pixelated edge” effect, and the TOA reflectance was extracted and modeled at the centroids of these lakes for comparison (Fig. 1.5 and Fig. 1.6).

Even with a fixed $\rho_{\text{water-leaving}}$ of 0 and ignoring the effects of bottom reflectance and turbidity, the modeled TOA reflectance at 833 nm strongly correlated with the observed values across the 47 lake centroids (Fig. 1.6). With a simple linear regression, 83.7 % of the variance of the lakes’ TOA reflectance could be explained by the adjacency effect. This is striking because the NIR band is often used to derive aerosol properties that are extrapolated to visible bands in atmospheric correction for aquatic remote sensing. Taking into account the adjacency effect in atmospheric correction, especially under high aerosol loadings, is therefore essential for deriving accurate reflectance spectra of inland waters and aquatic remote sensing products.

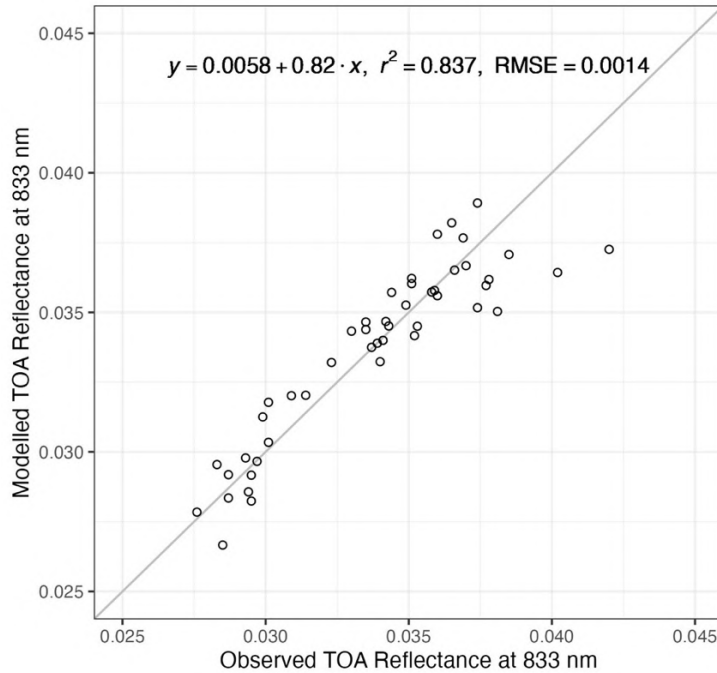


Fig. 1.6. Modeled and observed TOA reflectance (band 8 of Sentinel-2 MSI, centered at 833 nm) of Lake centroids near Brainerd, Minnesota on September 21, 2020. $AOT_{550} = 0.28$, wind speed = 5 m/s, and $N_{\text{photon}} = 1,000,000$ for T-Mart runs.

In addition, a sensitivity analysis was conducted to test the impact of various AOT and wind-speed values on the modeled TOA reflectance of the lakes. AOT_{550} of 0.23, 0.28, and 0.33 and

wind speeds of 3, 5, and 10 m/s were tested ([Appendix B](#)). An AOT₅₅₀ of 0.28 and wind speed of 5m/s produced the lowest RMSE and followed the 1:1 line the most closely, suggesting the two values used in Fig. 1.6 were reasonable.

1.4.2 Case study 2: transects of NIR reflectance

Another examination of the adjacency effect was conducted in Lake Edward (46.51N, 94.16W), one of the 47 lakes in Case Study 1. The TOA reflectance along two perpendicular transects across this lake was modeled in T-Mart and extracted from the images (Fig. 1.7). The same Sentinel-2 images and atmospheric settings for modeling in Case Study 1 were used in this case study.

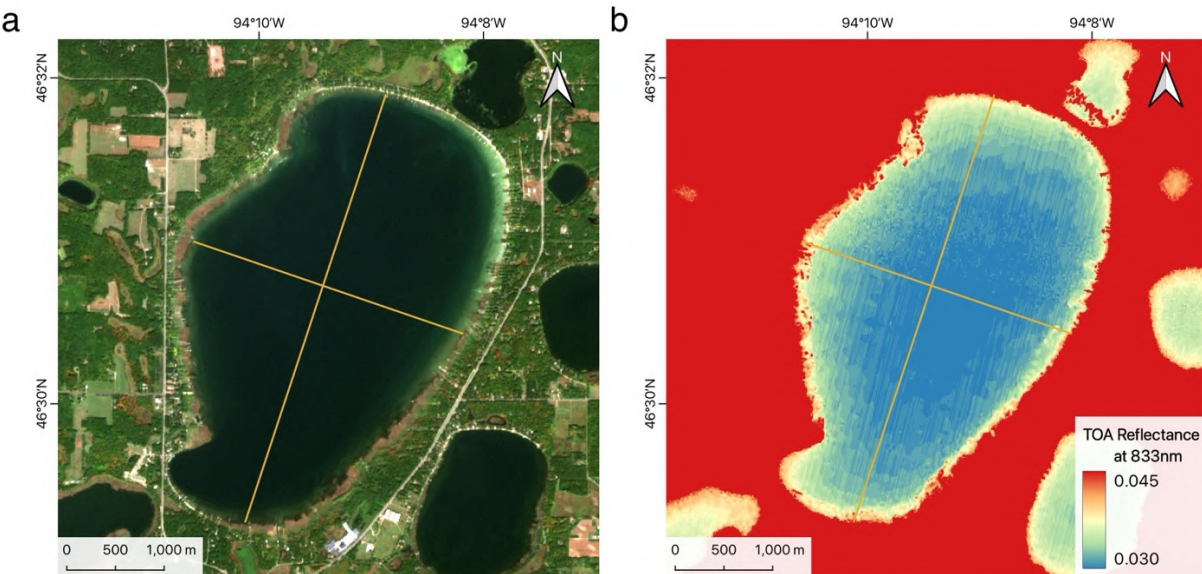


Fig. 1.7. a) Transects across Lake Edward, Minnesota, and b) the observed TOA reflectance (band 8 of Sentinel-2 MSI, centered at 833 nm) on September 21, 2020.

The modeled and observed TOA reflectance at 833 nm aligned with each other along the two transects in Lake Edward; both reached their lowest values in the middle of the lake and gradually increased toward the shorelines (Fig. 1.8). This aligned with the observation of Kiselev et al. (2015) where higher adjacency-effect-induced TOA reflectance in a NIR band was also found toward the shorelines. The observed reflectance was higher than modeled values near the edges of the lake (Fig. 1.8), likely from bottom reflectance or higher turbidity near the shore which can invalidate the assumption of no water-leaving radiance at 833 nm.

The modeled TOA reflectance was overestimated in the southern part of the North-South transect (Fig. 1.8b), where the narrow part of the lake had a higher simulated TOA reflectance than the observed reflectance. This may be explained by the fetch-limited wave growth (Kahma, 1981) – the size of the surface waves depends on the fetch or the length of water over which the wind has blown without obstruction. The narrowed southern part of the lake limits the fetch length and therefore could limit the size of the waves and lead to lower glint reflectance.

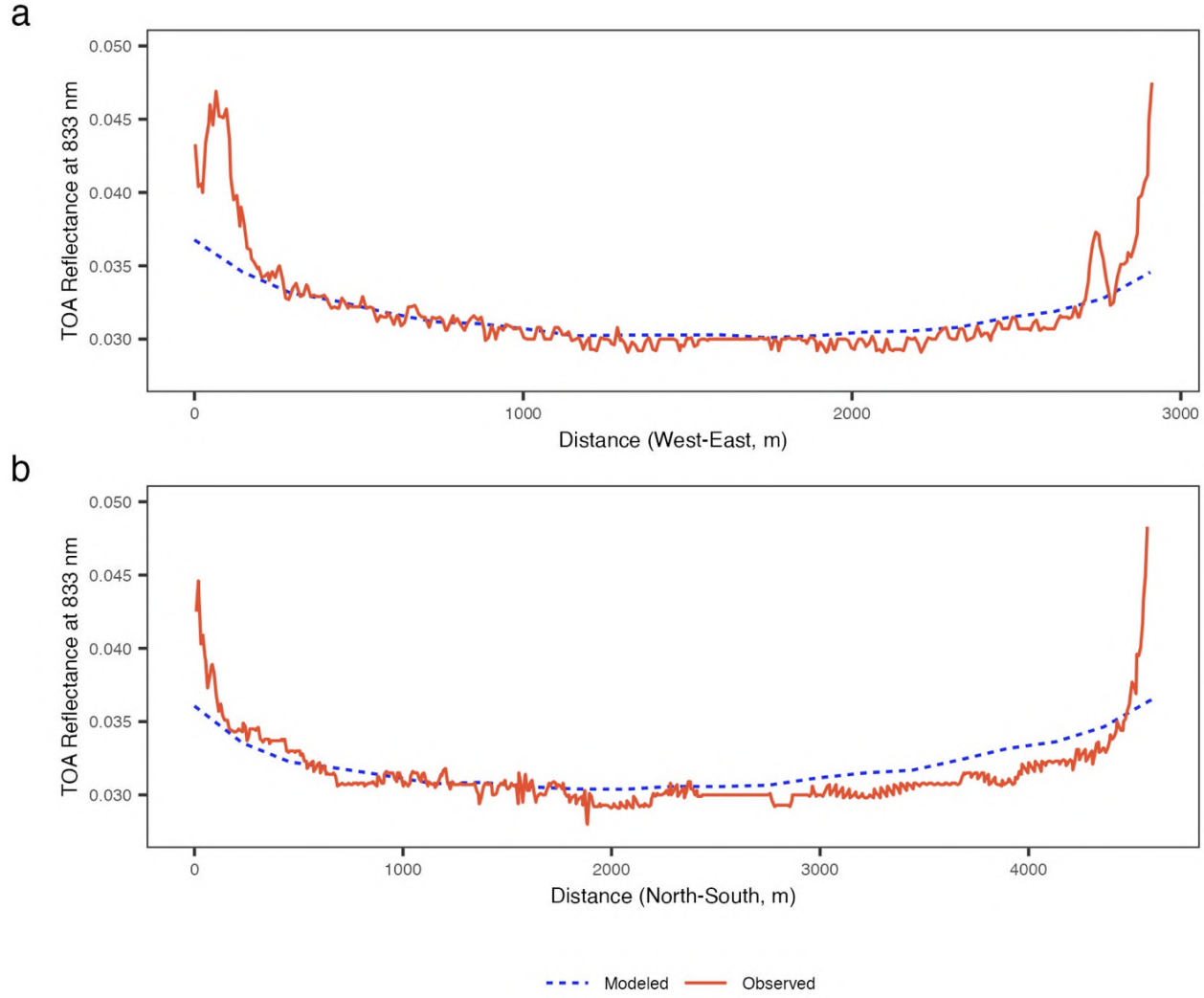


Fig. 1.8. Modeled and observed TOA reflectance (band 8 of Sentinel-2 MSI, centered at 833 nm) along a) west-east and b) north-south transects of Lake Edward, Minnesota on September 21, 2020.

1.4.3 Case study 3: surface-reflected light of ocean water in Hawaii

The surface-reflected light off of water, or glint, contains little information about the constituents in the water and can therefore be considered noise in ocean color remote sensing. This case study compares modeled surface-reflected light with field-measurement-derived values from Lee et al. (2010).

Glint has many implications in aquatic remote sensing. For atmospheric correction of open-ocean TOA images, glint is often modeled by Cox-Munk's equations and removed from the TOA reflectance of water (Zhang and Wang, 2010; Kay et al., 2009). For in-situ above-water measurements of water's reflectance, a common approach to isolate the water-leaving radiance (L_w , $\text{W sr}^{-1} \text{m}^{-2}$) from glint is to measure the sky radiance (L_{sky} , $\text{W sr}^{-1} \text{m}^{-2}$) at an angle reciprocal to the measurement of the total upwelling radiance (L_t , $\text{W sr}^{-1} \text{m}^{-2}$), multiply the sky radiance by a pre-computed effective sea-surface reflectance (r , unitless) to calculate surface-

reflected radiance (L_{sr} , $\text{W sr}^{-1} \text{m}^{-2}$), and remove L_{sr} from L_t (Lee et al., 2010). This can be summarized as

$$\begin{aligned} L_t &= L_w + L_{\text{sr}} = L_w + r \cdot L_{\text{sky}} \\ r &= \frac{L_{\text{sr}}}{L_{\text{sky}}} \\ L_w &= L_t - r \cdot L_{\text{sky}}. \end{aligned} \quad (1.13)$$

The value of r depends on sky conditions, the sea surface state, and viewing geometry (Mobley, 1999). It is often set to a spectrally flat value of 0.028 for all wavelengths with a viewing zenith angle of 40° and an azimuth angle of 135° relative to the sun when the wind speed is lower than 5 m/s; and for higher wind speeds, r increases accordingly but remains spectrally flat (Mobley, 1999).

Lee et al. (2010) took field measurements of L_t (9 scans), L_{sky} (5 scans), and downwelling irradiance just above the surface (E_d , 3 scans) to derive r . These measured values had slight variations due to natural ocean surface variability and the vessel constantly moving. To minimize the effect of the changing illumination, the radiances were converted to reflectances by normalizing them to E_d ,

$$T_{\text{rs}} = R_{\text{rs}} + r \cdot S_{\text{rs}} \quad (1.14)$$

where T_{rs} is the total remote-sensing reflectance (ratio of L_t to E_d), R_{rs} is the remote-sensing reflectance of water (ratio of L_w to E_d), and S_{rs} is the sky remote-sensing reflectance (ratio of L_{sky} to E_d). All these reflectances are hemispherical-directional and have a unit of sr^{-1} . Then, r is calculated as

$$r = \frac{T_{\text{rs}} - R_{\text{rs}}}{S_{\text{rs}}} \quad (1.15)$$

where the last unknown R_{rs} is derived from the bio-optical model of Morel and Maritorena (2001) using chlorophyll-a concentration of 0.05 and 0.1 mg/m³.

T-Mart can characterize the RT both in the atmosphere and at the ocean surface, allowing us to model r and compare with results from Lee et al. (2010). The environmental conditions documented by Lee et al. (2010) were used as input to model r in T-Mart. The measurements were made on clear open ocean near Hawaii (21.33 N, 158.16 W) at 12:50 pm local time on February 23, 1997. The wind speed was around 8 m/s, and the sky was cloud-free. L_t and L_{sky} were taken 90° from the solar plane to avoid strong sun glint, with zenith angles of 30° from nadir and 30° from zenith, respectively. The sun's position was calculated as 30.88° from zenith by entering the provided date, time and location in NOAA's Solar Calculator (<https://gml.noaa.gov/grad/solcalc/>). Only the relative azimuth angle of the sun was used in the modeling – although the sun's azimuth angle has an impact on the specular reflectance of water because the slopes of ocean surface waves have a small dependency on the wind direction (Appendix A2), the wind direction was unknown. Thus, an azimuthally averaged R_{glint} was

used, as this only depends on the relative azimuth angle between the sun and the sensor, and this is known from the image metadata. The AOT at the time of the measurements was unknown, and an averaged clear-sky AOT_{550} of 0.05 near Hawaii in February from the MODIS MCD19A2 data product (Lyapustin and Wang, 2018) was used. In addition, wind speeds of 6, 8, and 10 m/s were used to test the sensitivity of the results to wind speed.

Both modeled r and field-data-derived r showed a strong wavelength dependence over clear ocean water, increasing with longer wavelengths (Fig. 1.9). This raises concerns about Mobley (1999)'s suggestion of using a spectrally flat r in above-water measurements of R_{rs} . Most of the differences between the two datasets were within the 400 and 600 nm range, where the derived r largely depended on the chlorophyll concentration used in the bio-optical model (points in Fig. 1.9). The measurement-derived r values roughly fell within the 6-to-8 m/s range of the modeled values. The alignment between the two datasets supports the accuracy of the field measurements and the Cox-Munk surface-reflectance model implemented in T-Mart. The values of r varied significantly across the 400-to-800 nm spectrum in both datasets by a factor of up to 10, and the values at a single wavelength can be substantially different, too (Fig. 1.9). This suggests that r depends heavily on the environmental conditions such as wind speed and the movement of the vessel, in addition to its spectral dependence on atmospheric settings.

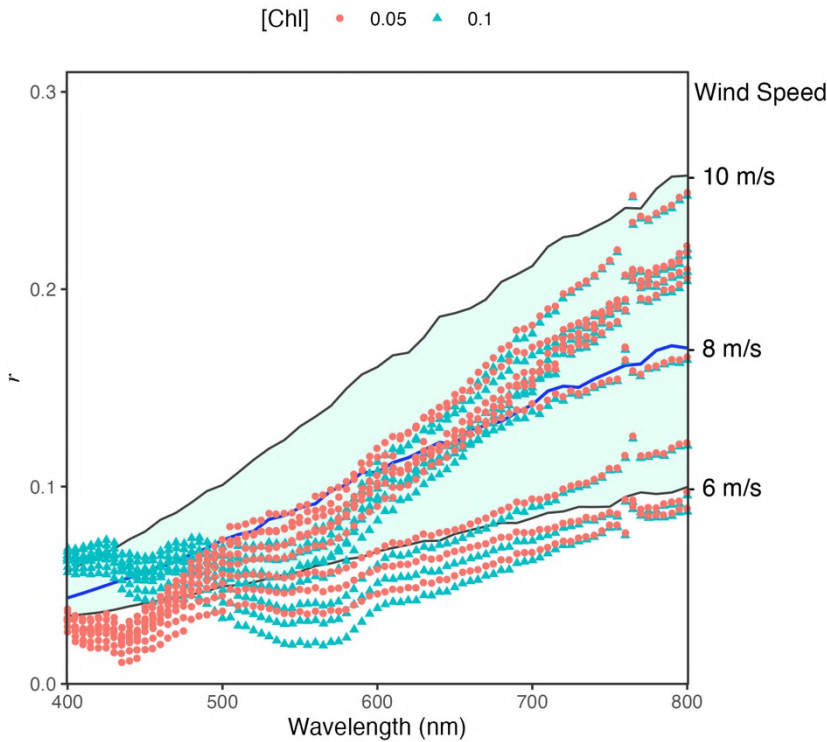


Fig. 1.9. Effective surface reflectance (r) as a function of wind speed from 400 to 800 nm. $AOT_{550} = 0.05$, wind speed = 6, 8, and 10 m/s (bottom, middle and top lines, respectively). Viewing and solar zenith angles are 30° and 30.88° , respectively, with a relative azimuth angle of 90° . Points are derived with two chlorophyll concentrations (unit: mg/m^3) from measurements in Lee et al. (2010). $N_{\text{photon}} = 100,000$ for T-Mart runs.

Another sensitivity analysis was run to explore the impact of various AOTs on r . AOT_{550} of 0, 0.05, and 0.1 were used against wind speeds of 6, 8, and 10 m/s, and it was found that r is higher

with lower AOTs (Fig. 1.10). This is because, at a low AOT, atmospheric scattering is predominantly molecular, which decreases exponentially with wavelength; this leads to a lowered L_{sky} at longer wavelengths. On the other hand, L_{sr} is not lowered with a lower AOT; in fact, it increases slightly due to lowered aerosol attenuation to solar irradiance in the atmosphere. An unchanging L_{sr} and a lowered L_{sky} contribute to the higher r (Eq. (1.13)). Higher r values were also associated with a higher wind speed (Fig. 1.10), which presumably increases the magnitude of the surface waves and directs more sun glint into the sensor's field of view, even if the sensor has an azimuth angle 90° relative to the sun.

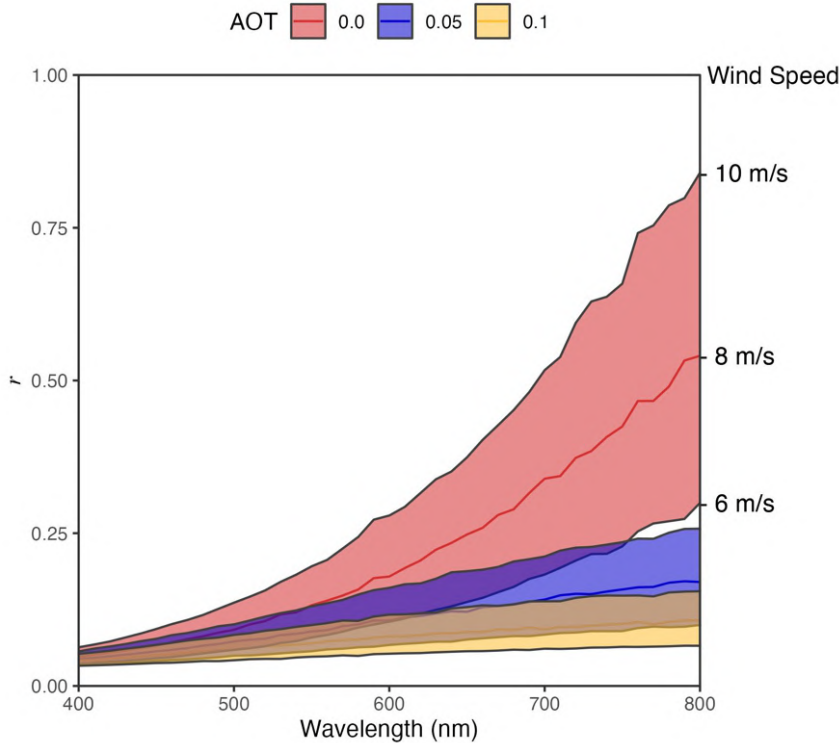


Fig. 1.10. Effective surface reflectance (r) as a function of wind speed and AOT from 400 to 800 nm, as modeled by T-Mart ($N_{\text{photon}} = 100,000$). Viewing and solar zenith angles are 30° and 30.88° , respectively, with a relative azimuth angle of 90° .

Lee et al. (2010) made direct measurements of S_{rs} , and the measured values fitted the range of modeled S_{rs} with a TOA between 0.05 and 0.025 (Fig. 1.11a). This suggests that the TOA of 0.05 used to produce Fig. 1.9 may be slightly overestimated, and the range of ρ with a slightly lower AOT will shift upward, making the measurement-derived values fit the modeled values better in the 400-700 nm range. The spectral shapes of simulated and measured S_{rs} are also slightly different, with most of the measured values decreasing more with wavelength than modeled values (Fig. 1.11a). This reflects small errors in the atmospheric and aerosol settings in the model. The wind speed was set to 8 m/s in the modeling of S_{rs} ; although in theory wind speed affects L_{sr} and ρ and therefore the spherical albedo of the atmosphere and L_{sky} , the impact is extremely small and wind speed was determined to have negligible impact on L_{sky} (not shown).

The impact of the total atmospheric transmittance, defined as the ratio of E_d at surface to E_d at TOA, was investigated (Fig. 1.11b). The magnitude of the total transmittance changed little with an AOT_{550} of 0.1 compared to 0.0 and 0.05; this is most likely due to aerosol's largely forward-scattering phase function. Although the high-absorption bands have a significant impact on the spectral shapes of L_{sky} and E_d (not shown), this impact is almost eliminated in the normalization process, leading to the relatively smooth spectral shapes of r and S_{rs} (Fig. 1.10 and Fig. 1.11a). The high-absorption bands led to some Monte Carlo noise in the modeled results, especially from H_2O at 720 nm and O_2 at 760 nm (Fig. 1.10).

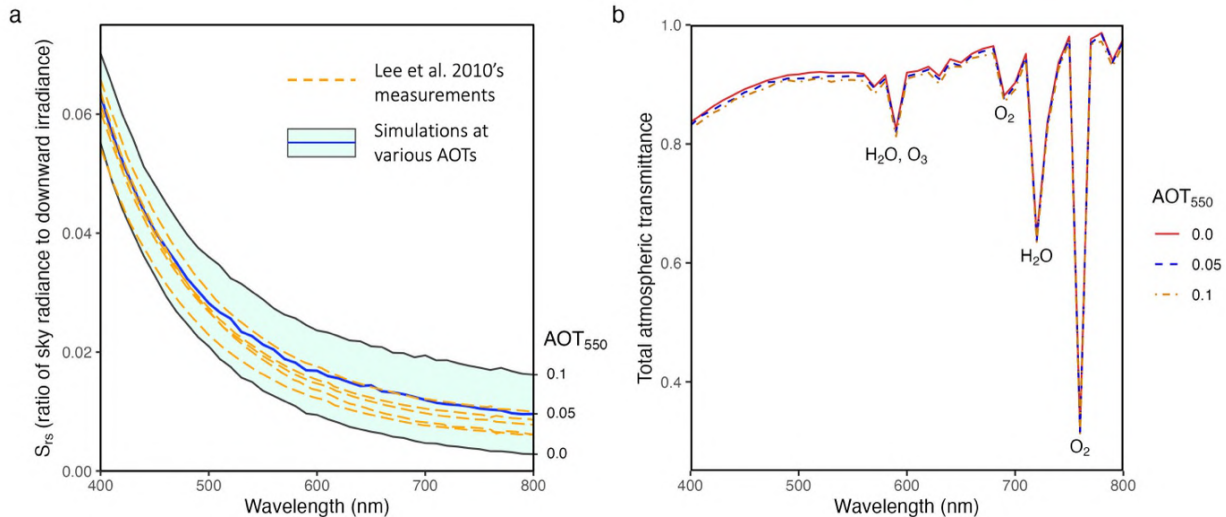


Fig. 1.11. a) Sky remote-sensing reflectance, S_{rs} , simulated at various AOTs and from Lee et al. (2010)'s measurements, and b) modeled total atmospheric transmittance at various AOTs, noting the important absorptive gases. Viewing and solar zenith angles are 30° and 30.88° , respectively, with a relative azimuth angle of 90° .

1.5 Discussion

1.5.1 Model accuracy

The accuracy of radiometric quantities calculated by T-Mart was carefully tested against RT models. T-Mart and libRadtran DISORT produced almost identical E_d^{diff} and ρ_{TOA} across a wide range of molecular-scattering optical thicknesses with high absorption (Fig. 1.2), providing confidence in the accuracy of T-Mart's radiative calculations. A comparison was also conducted between T-Mart and 6S using the same atmospheric and aerosol settings. Differences as large as 20 % in the calculated reflectances were observed at high-absorption wavelengths, but the results were very similar at most other wavelengths (Fig. 1.4). Although slower, Monte Carlo methods are unbiased RT solvers, and 6S itself was validated against Monte Carlo simulations (Kotchenova et al., 2006, 2008; Kotchenova and Vermote, 2007); these validations of 6S avoided high-absorption wavelengths (examples in Fig. 1.11b), and the reported up-to-1 % differences between 6S results and Monte Carlo benchmarks align with our observations at low-absorption wavelengths (Fig. 1.4). Given that T-Mart and libRadtran showed consistently good

agreement in high-absorption settings (Fig. 1.2) and they were developed independently, we conclude that T-Mart produces accurate estimates of its modeled radiometric quantities.

T-Mart also produced radiometric quantities in good agreement with measurement-derived values. In Case Studies 1 and 2, the modeled TOA reflectance matched Sentinel-2 observations across 47 lakes and along two transects in Lake Edward (Fig. 1.6 and Fig. 1.8). In Case Study 3, the effective sea-surface reflectance derived from measurements mostly fit the modeled values with a wind speed within 2 m/s of the recorded value, with few values outside the range where uncertainties were introduced by the chlorophyll concentrations used in the bio-optical model (Fig. 1.9). Although measurements may seem to be the best way to evaluate a model, they often come with their own uncertainties and can be influenced by changing environmental conditions. To fully compare a model to actual measurements, a closure experiment with complete input and output measurements is required. This is extremely challenging due to the large scale of ocean color remote sensing and the many factors that could affect the water, the atmosphere, and sometimes even the sensors. Assumptions are often made about the model input in model-versus-measurement comparisons for specific applications; thus, the assumptions and their impact must be considered when applying the modeled results.

We provide a special single-photon mode in T-Mart for users' validation purposes. The series of movements of a single photon from launching to exiting the atmosphere can be visualized in a 3D space (Fig. 1.1). Users can freely zoom and rotate the visualized modeled surface and photon movement in 3D through the Python *matplotlib* package, and the details of radiometric calculations at each movement are printed in the console. This allows users to examine the input surface topography and solar-viewing geometry and verify the calculated radiometric quantities.

1.5.2 Contribution to aquatic remote sensing

Existing RT models have limitations in modeling the TOA reflectance of coastal and inland waters. The widely used MODTRAN (Berk et al., 2014) and 6S (Vermote et al., 1997b) are both 1D RT modeling tools; they are unsuitable for modeling waterbodies influenced by the adjacency effect such as the elevated NIR reflectance over lakes surrounded by vegetation (Section 1.4.1). The RT code SMART-G (Ramon et al., 2019) uses the Monte Carlo approach; it supports adjacency modeling but is limited to circular water surfaces surrounded by homogeneous land of uniform reflectance. MCARaTS (Iwabuchi and Okamura, 2017) is another RT code, and it was used to model the adjacency effect in Pan et al. (2022). However, the code is atmosphere-oriented and lacks support for modeling water's radiative properties, such as water's specular reflectance. In addition, MCARaTS was developed in Fortran, and it only supports Linux/UNIX-like operating systems, making it difficult to work with open-source tools. The work of Bulgarelli et al. (2014) and Bulgarelli and Zibordi (2018) simulated the adjacency effect in aquatic remote sensing in the northern Adriatic Sea, but the code is closed source and lacks support for arbitrary topography, which may affect the illumination conditions of inland waterbodies (Moses et al., 2017). libRadtran (Emde et al., 2016) is a publicly available library of multiple RT solvers. The 3D version of the MYSTIC solver is close to T-Mart in nature, but only the 1D version is publicly available. Although developed for atmospheric applications, according to the user guide, the 3D MYSTIC is capable of modeling the adjacency effect (Mayer et al., 2020). However, the modeled space is cubic; if a photon leaves the modeled space through one

of the four horizontal sides, it re-enters the space through the opposite side (Mayer, 2009). The ‘duplicate’ spaces may be sufficient for atmosphere and cloud modeling but are not suitable for modeling coastal and inland environments where water and land tend to exhibit non-duplicate features. In addition, the implementation of Cox-Munk’s equations in libRadtran for modeling ocean surfaces has not been validated (Mayer et al., 2020).

T-Mart was developed to address the limitations described above. Foremost, T-Mart is the only publicly available RT model that allows the simulation of the adjacency effect on aquatic remote sensing in an arbitrary 3D space and provides a framework for developing and validating adjacency-correction tools in such an environment. All the RT models described above provide limited API support for extendibility, except 6S with its Python interface Py6S (Wilson, 2013) which allows users to access other Python functionality. T-Mart is exclusively written in Python, making it easy to work with the rich library of Python modules and allowing users to perform more complex tasks and create workflows within the Python environment. For example, users can import satellite images to T-Mart using the *GDAL* package in Python, as demonstrated in Section 1.4.2. The Python package *Pycuda* is used in SMART-G to run the GPU-accelerated code written in the C language, which requires NVIDIA GPUs. In practice, many computers lack NVIDIA GPUs, and even if they do, the multiple layers of APIs from Python to C and the hardware make version control and running the code difficult. On the other hand, T-Mart uses the native Python *multiprocessing* package to simplify installation and ensure the smooth running of the code. Code developed in Fortran or C languages requires compiling; this requires specific software environments and often comes with compatibility issues across operating systems. This is not an issue for T-Mart as it was developed in Python exclusively.

In addition, T-Mart uses 6S parameterizations for atmospheric and aerosol settings through the use of Py6S (Wilson, 2013); therefore, studies or applications that use 6S can easily incorporate T-Mart into their workflows and extend 1D RT modeling to 3D modeling without changing these parameters. Applications of 6S in aquatic remote sensing include building look-up tables for atmospheric correction (Vanhellemont and Ruddick, 2018), developing sun-glint-correction algorithms (Harmel et al., 2018), and studying the adjacency effect of ice (Bélanger et al., 2007). The same-parameterization approach allows the continuity of past data processing and enhances the existing workflows with 3D capabilities and adjacency-effect modeling support.

The radiative properties of shadowed water can also be calculated in T-Mart. Shadows contain information that is sometimes used in atmospheric correction; for example, Lee et al. (2007) used adjacent water pixels that are in and out of a cloud shadow to estimate R_{atm} , and ACOLITE uses shadows to retrieve AOTs (Vanhellemont and Ruddick, 2018). T-Mart can be a validation tool for such efforts.

1.5.3 Case studies

In Case Study 1, the variance of TOA NIR reflectance between 47 lakes of different sizes was largely explained by the adjacency effect ($r^2 = 0.837$). This has an implication for atmospheric correction algorithms that assume negligible water-leaving radiance in the NIR band. These algorithms use the NIR reflectance to retrieve AOT; if the adjacency effect is not considered, AOT can be overestimated from the elevated TOA NIR reflectance due to the adjacent

vegetation, leading to over-correction of atmospheric effects and low and even negative reflectances at visible wavelengths (Moses et al., 2017). This also affects glint-correction algorithms. The statistical wave-slope-distribution approach often fails to estimate the reflectance of spatially resolved glint in high-resolution imagery that is commonly used in coastal and inland scenes (Kay et al., 2009). Another approach uses the NIR band to estimate glint reflectance on a pixel-by-pixel basis; it assumes water-leaving radiance is negligible in the NIR band after atmospheric correction, and it removes or minimizes glint by establishing a linear relationship between the glint reflectance in NIR and visible bands (Kay et al., 2009). As a result, the intertwined contribution from the glint and the adjacency effect needs to be separated to estimate AOT and glint reflectance in atmospheric correction processes to retrieve accurate water reflectance and the follow-up bio-optical properties. A challenge lies in the different spectral shapes of the two effects; while glint reflectance depends on the spectral refractive index of water, which changes very little in the visible spectrum (Quan and Fry, 1995), the spectral shape of the adjacency effect depends heavily on the surrounding environment. In areas dominated by vegetation, the impact of the adjacency effect will be larger in NIR wavelengths, where the vegetation is much brighter than water, than in the visible range. T-Mart provides a framework to forward-model the two effects and possibly derive inversion algorithms.

The sensitivity analysis of the impact of various AOT and wind speed values showed that the TOA reflectance at NIR wavelengths increased with AOT and wind speed ([Appendix B](#)). The increased AOT seemed to have a greater effect on the high-reflectance (smaller) lakes, whereas the increased wind speed had a similar effect on all the lakes. By looking at waterbodies of different sizes, the waterbody-size dependency of AOT-induced R_{env} and the less size-dependent R_{glint} may help separate glint and adjacency-effect contributions in the atmospheric correction. Careful modeling and correction for glint and adjacency contribution are key to improving remote sensing of waterbodies similar to the lakes in the case study.

In Case Study 2, T-Mart correctly modeled the TOA reflectance along the two transects and the increased reflectance approaching the shorelines over Lake Edward. The underestimated modeled TOA reflectance near the shorelines illustrates that the zero-water-leaving-radiance assumption does not hold in waters with possible turbidity, suspended particles, bottom reflectance, and biochemical processes (Boss et al., 2007). The fetch effect (Kahma, 1981) may have contributed to the lowered TOA reflectance over the narrowed southern part of the lake. It is also possible that the wind speed was not distributed evenly across the lake at the time of image acquisition; a lowered wind speed can lead to smaller waves and lowered glint reflectance. Similar findings were reported by Tilstone et al. (2020), where the effective wind speed was reduced by 30 % when the wave height was determined to be low in a coastal environment. Additionally, while the change in TOA reflectance as a function of distance to the shore may not provide enough information to derive both AOT and aerosol properties such as aerosol composition and size distribution, the magnitude and the rate of change may restrict the possible values of one given the other.

In Case Study 3, the modeled sky remote-sensing reflectance and effective sea-surface reflectance aligned well with in-situ observations and field-data-derived values (Fig. 1.11a and Fig. 1.9, respectively). The differences between modeled and derived values in Fig. 1.9 mostly come from uncertainties in the chlorophyll concentrations used in the bio-optical model; this

highlights the challenge of choosing a value for r in the field. This case study provides model support for Lee et al. (2010), raising concerns about the spectrally invariant assumption for r in Mobley (1999). Such an assumption may only be valid when the sky is completely overcast, an environmental situation unconducive to ocean color remote sensing. The wide range of r values (Fig. 1.10) illustrates the sensitivity of r to wind speed and AOT as well as atmospheric and aerosol settings; this underscores the challenge of measuring R_{rs} using above-water approaches. Given that Cox-Munk's equations were developed for ocean environments, and they do not necessarily hold for inland and coastal environments where waves' amplitude is limited by fetch and the size and depth of the waterbody; controlled experiments are desired to test the calculations and measurements of r and R_{rs} in such environments.

It was found that the change in S_{rs} at various AOTs has very little wavelength dependence (Fig. 1.11a). A pure molecular sky at this viewing angle is exceptionally blue (AOT₅₅₀ 0.0 line in Fig. 1.11a), and the increased S_{rs} from aerosol loading is evenly distributed across the spectrum, making the sky appear whiter. As a result, if the atmosphere and aerosol models are sufficiently accurate in the model, either the color or the line height of S_{rs} may be used to estimate AOTs.

1.5.4 Installation and uses of T-Mart

T-Mart can be installed using two short command-line calls:

- `conda install -c conda-forge Py6S`
- `pip3 install tmart`

The dependencies of T-Mart are available on *conda-forge*, a community effort that ensures the compatibility of packages. T-Mart itself can be installed from the Python Package Index with a single command line. The entire installation of T-Mart and its dependencies can be completed in minutes. T-Mart runs on systems with Python support, and it is tested on macOS, Microsoft Windows, and Linux systems.

Detailed instructions for T-Mart are available from <https://tmart-rtm.github.io>. Users are instructed to import data, run the code and visualize results. Guidance is also provided for configuring the atmospheric and surface settings, the radiometric quantities of interest, and the observation and illumination geometries.

1.5.5 Future development

T-Mart can be used to develop adjacency-correction algorithms. By default, the calculated RT results contain the entire trajectory of every photon including the movements and collision locations as well as the local-estimate weights (Eq. (1.8)); this information can be used to derive formulations for adjacency-effect correction. Due to T-Mart's 3D nature, formulations at off-nadir angles and with arbitrary surfaces can be derived, as opposed to solutions restricted to circular targets in Vermote et al. (1997b), Sei (2015), and Ramon et al. (2019).

T-Mart can also be coupled with HydroLight to combine in-water RT with atmospheric and water-surface RT calculations. This can be done by providing HydroLight with the sky illumination computed by T-Mart, or by importing HydroLight-computed bidirectional reflectance distribution of water-leaving radiance into T-Mart. Polarization support will also be

useful with a vector version of HydroLight, which is currently in development (J. Hedley, personal communication).

1.6 Conclusion

This article presents a Monte Carlo code, T-Mart, that simulates the transfer of light in a 3D ocean-land-atmosphere system. The code is the first open-source tool that considers surface irregularity of water and land in modeling the adjacency effect on water's TOA reflectance, therefore suitable for RT over coastal and inland waters. It was exclusively developed in Python, allowing users to integrate it with the rich library of Python modules. T-Mart uses the same atmospheric and aerosol settings as 6S, facilitating existing workflows to transition from 1D to 3D RT modeling with minimal effort. The code was validated by comparing simulations with libRadtran and 6S as well as satellite and in-situ measurements, which all showed good alignment.

In three case studies, we demonstrated the use of the code, the importance of the adjacency effect in remote sensing of coastal and inland waters, and the wavelength dependence of the effective sea-surface reflectance. In Case Study 1, the adjacency effect explained 83.7 % of the variance in NIR TOA reflectance of 47 lakes in Minnesota, highlighting that the adjacency effect cannot be ignored in atmospheric correction for remote sensing of inland waters. The various spectral shapes of glint and the adjacency effect remain a challenge in atmospheric correction; T-Mart is capable of forward-modeling the additive contribution of the two effects, but the inversion problem remains to be investigated. In Case Study 2, the modeled and observed TOA reflectance in the NIR band matched each other along the two transects in Lake Edward; both reached their lowest values in the middle of the lake and gradually increased toward the shores. At the same time, there is a markedly elevated reflectance near the shores, likely from turbidity or bottom reflectance, invalidating the zero-water-leaving-reflectance assumption near the shores. In Case Study 3, modeled and field-data-derived r aligned with each other, showing significant wavelength dependence as r increases at longer wavelengths. In addition, the dependence of r on AOT and wind speed was demonstrated. The magnitude of S_{rs} was found to depend on AOT, but the spectral shape of S_{rs} showed minimal AOT dependency; this makes it possible to infer AOT from either the color or the line height of S_{rs} , given sufficiently accurate atmosphere and aerosol models.

It is envisaged that T-Mart will provide a framework for the development and validation of physics-based methods that remove or minimize the adjacency effect in remote sensing of coastal and inland waters. This has the potential to improve the accuracy of retrieved water reflectance, the basis for optical retrieval of bathymetry and water quality information, in such environments.

Author statement

YW: Conceptualization, Methodology, Software, Formal Analysis, Validation, Writing – Original Draft; **AK:** Conceptualization, Supervision, Funding Acquisition, Writing – Review & Editing; **DL:** Conceptualization, Funding Acquisition, Writing – Review & Editing.

Declaration of competing interest

The authors declare that they have no known competing financial interests or personal relationships that could have appeared to influence the work reported in this paper.

Acknowledgments

This work was supported by the Canadian Space Agency [19FAOTTB32; 22AO2-LIQU]; the Ontario Graduate Scholarship program; Liquid Geomatics; and Agriculture and Agri-Food Canada [J-001839-Emerging Ecosystem Services; J-0002305-Environmental Change Onehealth Observatory (ECO²)]. We thank the European Space Agency (ESA), the European Organisation for the Exploitation of Meteorological Satellites (EUMETSAT), and the European Union's Earth observation programme Copernicus for providing Sentinel-2 data. We thank Quinten Vanhellemont for identifying the lakes in Minnesota for studying the adjacency effect. Michael Sawada, Chuiqing Zeng, John Hedley, Shun Bi, and Rui Zhang are thanked for their valuable comments and discussions.

1.7 Appendix A. Surface reflectance of water

A1 Bidirectional and hemispherical-directional glint reflectances

Bidirectional reflectance is the ratio of reflected radiant flux per unit solid angle surrounding a given direction to the collimated incident radiant flux (Schaeppman-Strub et al., 2006). The bidirectional reflectance of glint is defined following Kay et al. (2009),

$$R'_{\text{glint}}(\theta_s, \phi_s, \theta_v, \phi_v) = \frac{p(\xi, \eta)\rho_{\text{Fresnel}}(n_w, \theta_i)}{4 \cos^4 \beta \cos(\theta_v) \cos(\theta_s)} \quad (\text{A1})$$

where $p(\xi, \eta)$ is the Cox-Munk probability distribution of the wave slopes in Eq. (A3), $\rho_{\text{Fresnel}}(n_w, \theta_i)$ is the Fresnel reflectance ([Appendix A3](#)) as a function of water's refractive index (n_w) and the incidence angle (θ_i), β is the tilt of the water surface facet that reflects the incident light to the viewing direction, θ_v and θ_s are the viewing and solar zenith angles, and ϕ_v and ϕ_s are the viewing and solar azimuth angles, respectively.

When the collimated direct solar irradiance is the only source of incident radiant energy, R'_{glint} can be used to estimate glint reflectance; however, with a diffuse illumination of sky light, the incident radiant energy from the entire hemisphere must be considered to derive the hemispherical-directional glint reflectance,

$$R_{\text{glint}}(\theta_v, \phi_v) = \frac{1}{N} \sum_{j=1}^N R'_{\text{glint}}(\theta_{sj}, \phi_{sj}, \theta_v, \phi_v) \quad (\text{A2})$$

where N is the number of reflection events at the water surface in the Monte Carlo simulation, and θ_{sj} and ϕ_{sj} are respectively the zenith and azimuth angles of the j th collimated incident

radiant flux. Eq. (A2) essentially calculates the reflected radiance in a specified direction given the combined direct and diffuse illumination conditions.

A2 Cox-Munk wave-slope statistics

The Cox-Munk slope statistics (Cox and Munk, 1954) describes the distributions of wave slopes of a wind-roughened sea surface as a function of wind speed and direction. It is widely used to model and remove glint from aquatic remote-sensing products. The probability of slopes can be calculated as

$$p(\xi, \eta) = \frac{1}{2\pi\sigma_c\sigma_u} \exp \left[-\frac{1}{2} (\xi^2 + \eta^2) \right] \times \left[1 - \frac{1}{2} c_{21}(\xi^2 - 1) \eta - \frac{1}{6} c_{03}(\eta^3 - 3\eta) + \frac{1}{24} c_{40}(\xi^4 - 6\xi^2 + 3) + \frac{1}{4} c_{22}(\xi^2 - 1)(\eta^2 - 1) + \frac{1}{24} c_{04}(\eta^4 - 6\eta^2 + 3) \right] \quad (\text{A3})$$

where ξ and η are the normalized slopes,

$$\xi = \frac{z_x}{\sigma_c} \text{ and } \eta = \frac{z_y}{\sigma_u}, \quad (\text{A4})$$

and z_x and z_y are the slopes (change in elevation over change in horizontal distance) along crosswind and upwind directions. The two slope variances (σ_u and σ_c are for upwind and across wind directions, respectively) are calculated using the wind speed U (m/s) at 12.5 m from the surface,

$$\begin{aligned} \sigma_u^2 &= 3.16 \cdot 10^{-3} U \\ \sigma_c^2 &= 1.92 \cdot 10^{-3} U + 0.003. \end{aligned} \quad (\text{A5})$$

The skewness and peakedness coefficients in (A3) are

$$c_{21} = 0.01 - 0.0086U, c_{03} = 0.04 - 0.033U, c_{40} = 0.40, c_{22} = 0.12, c_{04} = 0.23. \quad (\text{A6})$$

A3 Fresnel's equation

The law of refraction, also known as Snell's law, states that,

$$n_1 \sin \theta_1 = n_2 \sin \theta_2 \quad (\text{A7})$$

where n_1 and n_2 are the refractive indices of two media, and θ_1 and θ_2 are interchangeably angle of incidence and angle of transmission. The refractive indices of air (n_a) and water (n_w) are usually taken as 1 and 1.34 at visible wavelengths. T-Mart allows user-specified n_w or calculates

n_w as a function of user-specified salinity, temperature, and wavelength according to equation 3 in Quan and Fry (1995).

The angle of transmission (θ_t) is a function of the incidence angle (θ_i) and the refractive indices of the two media. Take a light incident on the water from the air as an example,

$$\theta_t = \sin^{-1}\left(\frac{n_a}{n_w} \sin \theta_i\right). \quad (\text{A8})$$

The fraction of this collimated incident irradiance reflected specularly by the air-water interface (i.e., not penetrating the surface) is then described by Fresnel's equation for unpolarized light,

$$\rho_{\text{Fresnel}}(\theta_i) = \frac{1}{2} \left\{ \left[\frac{\sin(\theta_i - \theta_t)}{\sin(\theta_i + \theta_t)} \right]^2 + \left[\frac{\tan(\theta_i - \theta_t)}{\tan(\theta_i + \theta_t)} \right]^2 \right\}. \quad (\text{A9})$$

A4 Whitecaps

Whitecaps are the foamy crests of waves at the water surface. The whitecap model in T-Mart generally follows Mobley (2022) with modifications to the spectral dependence (Table A1). Whitecap reflectance is treated to be Lambertian, and it is calculated following Koepke (1984),

$$\rho_{\text{whitecap}}(\lambda) = 0.22 \times a_{\text{whitecap}}(\lambda) \quad (\text{A10})$$

where $a_{\text{whitecap}}(\lambda)$ is a correction factor that describes the wavelength dependence of ρ_{whitecap} . The values of a_{whitecap} are presented in Table A1.

Table A1. Normalized spectral dependence of whitecap reflectance. Source: Figure 3 of Frouin et al. (1996).

Wavelength (nm)	Value
400	1
444	1
543	0.95
663	0.92
871	0.62
1023	0.53
1654	0.14

The fraction of the sea surface covered by whitecaps (F) is a function of wind speed, and it is 0 at a wind speed of 6.33 m/s or lower (Stramska, 2003),

$$F = 8.75 \times 10^{-5} (U - 6.33)^3. \quad (\text{A11})$$

1.8 Appendix B. Modeled TOA reflectance of lakes as a function of AOT and wind speed

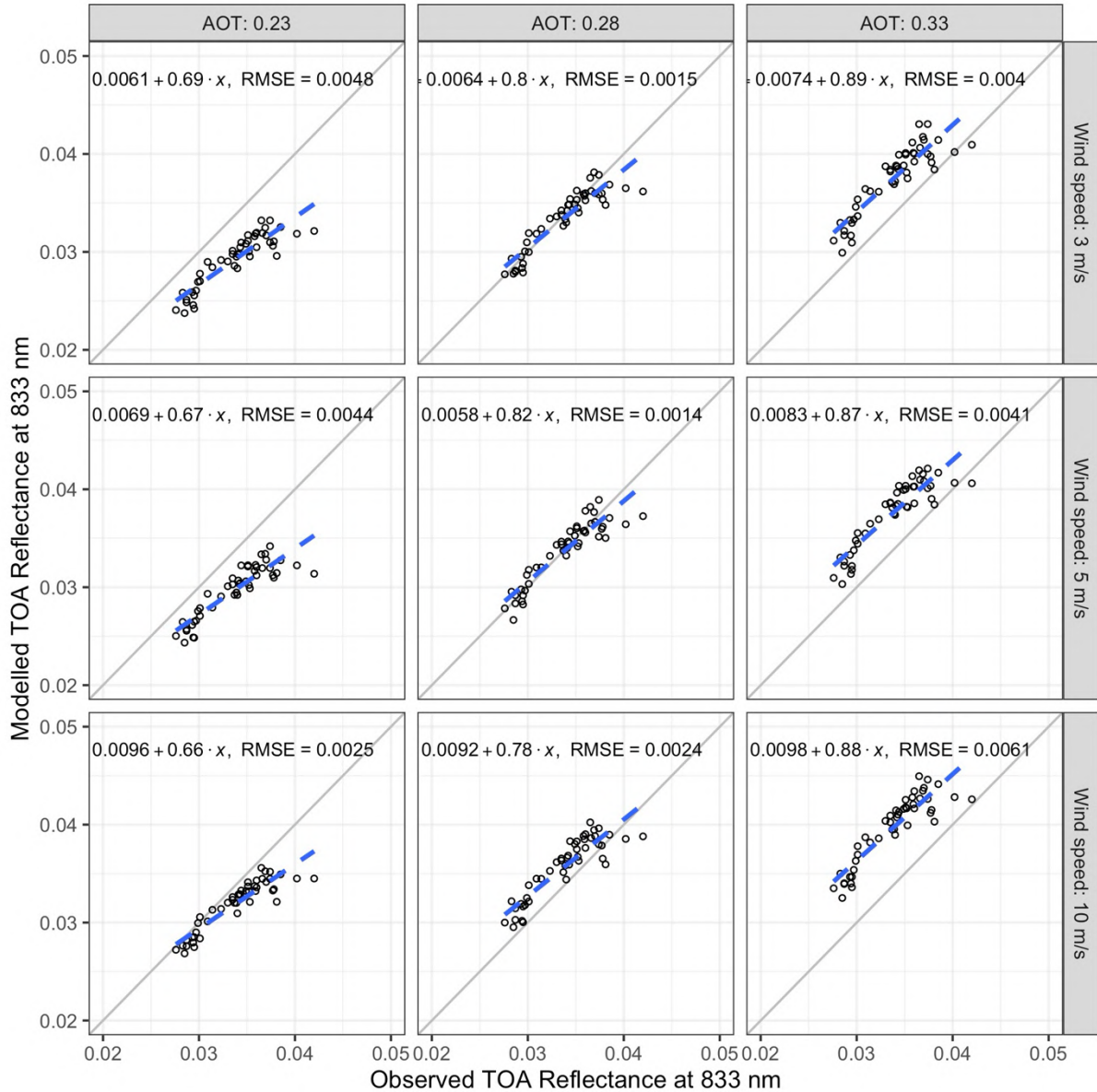


Fig. B1. Modeled and observed TOA reflectance (band 8 of Sentinel-2 MSI, centered at 833 nm) of Lake centroids near Brainerd, Minnesota on September 21, 2020. AOT₅₅₀ of 0.23, 0.28, and 0.33, and wind speeds of 3, 5, and 10 m/s were included. $N_{\text{photon}} = 1,000,000$ for T-Mart runs.

Chapter 2: Sensor-generic adjacency-effect correction for remote sensing of coastal and inland waters

Yulun Wu^a, Anders Knudby^a, Nima Pahlevan^{b,c}, David Lapen^d, Chuiqing Zeng^e

^aDepartment of Geography, Environment and Geomatics, University of Ottawa, Ottawa, ON, Canada

^bScience Systems and Applications Inc., Lanham, MD, USA

^cNASA Goddard Space Flight Center, Greenbelt, MD, USA

^dOttawa Research and Development Centre, Agriculture and Agri-Food Canada, Ottawa, ON, Canada

^eEnvironment and Climate Change Canada, Canada Centre for Inland Waters, Burlington, ON, Canada

Abstract

The adjacency effect distorts the top-of-atmosphere (TOA) spectral signals of coastal and inland waters and is a major challenge for optical remote sensing of nearshore aquatic environments. We introduce a closed-form expression that corrects for the adjacency effect prior to atmospheric correction. The method is included in an open-source Python tool, which ingests level-1 imagery and calculates the point-spread function of the atmosphere to convolve the input imagery. For each band, the difference between the observed and convolved reflectances is used to quantify and correct for the adjacency effect, i.e., pixels are corrected to the TOA reflectance they would have if surrounded by pixels of identical reflectance. Validation was conducted for Sentinel-2 MSI and Landsat 8 OLI imagery against a global dataset of coincident *in situ* radiometric measurements. Results showed improved accuracy of water-leaving reflectance derived by atmospheric correction processors, including ACOLITE, POLYMER, and l2gen, when these were applied following adjacency-effect correction. For matchups within 200 m of shorelines ($n = 212$), adjacency-effect correction resulted in an average 16.7 % reduction in root mean squared error, a 32.4 % reduction in symmetric signed percentage bias, and a 36.8 % reduction in median symmetric accuracy for the three processors. The improvements were more significant in the near-infrared (NIR) range for ACOLITE, visible wavelengths for l2gen, and evenly distributed across the visible-NIR spectrum for POLYMER. We anticipate that this physics-based approach to adjacency-effect correction will lead to improved satellite-derived aquatic products for coastal and inland waters under diverse atmospheric and aquatic conditions.

Keywords: aquatic remote sensing; adjacency effect; atmospheric correction; coastal waters; inland waters

DOI: 10.1016/j.rse.2024.114433

2.1 Introduction

In optical remote sensing, the adjacency effect (AE) refers to how adjacent surfaces influence the observed spectral signal of a target surface through atmospheric scattering (Tanré et al., 1987). The AE reduces the contrast between neighboring pixels with different reflectances and poses a challenge for quantitative remote sensing of nearshore waters adjacent to bright surfaces. The AE is commonly observed over coastal and inland waters in the near-infrared (NIR) wavelengths, in which adjacent vegetated land is much more reflective than water and the strong forward scattering of aerosols dominates atmospheric scattering (Sterckx et al., 2011). The magnitude of the AE depends on several factors, including the gas and aerosol composition of the atmosphere (Santer and Schmechtig, 2000), sun-sensor geometry (Vermote et al., 1997b), topography (Moses et al., 2017), land-cover type and sensor characteristics (Bulgarelli and Zibordi, 2018), the reflectance difference between the target and surrounding pixels (Wang et al., 2021a, 2021b), and the shape and size of waterbodies, with small waterbodies being more affected by the AE than large ones (Sterckx et al., 2015; Martins et al., 2019).

The AE poses a significant challenge for atmospheric correction (AC) over inland and coastal waters, negatively affecting the characterization of atmospheric properties (Bulgarelli et al., 2017) and the accuracy of satellite-derived aquatic data products (Warren et al., 2021). In such environments, inaccurate AC often leads to errors in the estimated surface reflectance, and those errors are propagated into the quantitative retrieval and analysis of biogeochemical variables, such as near-surface concentration of chlorophyll-a (Chl-a) and total suspended solids (TSS), as well as their spatial and temporal variability (Pahlevan et al., 2020). The heightened NIR reflectance over waters near vegetation can disrupt algorithms that use such wavelengths to derive aerosol optical thickness (AOT), resulting in overestimated AOTs and subsequent overcorrection of surface reflectance in visible wavelengths (Hieronymi et al., 2023). In coastal and productive waters where NIR reflectance is non-negligible (Wang and Shi, 2005), separating the NIR contributions from the AE and water itself is therefore essential for effective AC and bio-optical modeling. Considering the sensitivity of aquatic remote sensing products to even minor sources of noise, evaluating and correcting for the AE is crucial in remote sensing of freshwater and coastal aquatic environments (Bulgarelli and Zibordi, 2018).

The problem of the AE for satellite observations has been investigated for decades (Bélanger et al., 2007; Bulgarelli et al., 2014; Bulgarelli and Zibordi, 2018; Sterckx et al., 2011; Tanré et al., 1987; Vermote et al., 1997a; Wang et al., 2021a), and various methods have been developed to address this challenge for aquatic applications. Correcting for the AE requires knowledge of the point spread function (PSF) of the atmosphere, which describes the spatial origin of diffuse radiation and how radiation from various surface locations contributes to at-sensor measurements (Sei, 2015). Various approaches have been taken to characterize the PSF. One approach to obtain the PSF and correct for the AE is to use the computationally efficient primary scattering approximation (Santer and Schmechtig, 2000). For example, the primary scattering approximation was employed in the sensor-generic AE correction algorithm developed by Kiselev et al. (2015), which was integrated into the Modular Inversion and Processing system for deriving biophysical parameters from at-sensor radiance measurements (Heege and Fischer, 2004). Similarly, the Improved Contrast between Ocean and Land (ICOL) processor, developed for correcting the AE in MERIS data, also employs the primary scattering assumption (Santer

and Sterckx, 2013). ICOL incorporates simplified formalisms for the influence of clouds and a land mask to adjust the diffuse component of Fresnel reflection of the water surface in the presence of the AE. The performance of ICOL has not been reported consistently across the literature: while Odermatt et al. (2010) found improved retrieval of Chl-a from MERIS data in six perialpine lakes in Europe, Binding et al. (2011) noted that ICOL did not notably improve water constituent retrievals in Lake of the Woods at the Canada-US border.

Another approach to characterizing the PSF involves formulations derived from Monte Carlo simulations (Vermote et al., 1997a, 2006; Tanré et al., 1981; Sei, 2015; Reinersman and Carder, 1995). Martins et al. (2019) and Paulino et al. (2022) extracted the contribution of the AE through the formulae of PSF parameterized from Monte Carlo simulations in Vermote et al. (2006). While these derived formulations allow quick computation, they are limited by the assumption that environmental weights only depend on diffuse transmittances and distance from the neighboring pixel to the target pixel, neglecting the importance of observation geometry in the AE (Bulgarelli et al., 2014). Moreover, these formulations were derived using a single aerosol model from McClatchey et al. (1971), thereby ignoring the diversity of aerosol types and their varying optical characteristics. Similarly, Reinersman and Carder (1995) computed the PSF for a simulated sensor at an altitude of 20 km through Monte Carlo methods, and they implemented an iterative approach to correct for the AE at the surface level. In this approach, surface reflectance is first estimated in the absence of AE correction, then modified iteratively until the simulated TOA reflectance matches the observed reflectance. Although the iterative process has had preliminary successes, it can be computationally costly and not all pixels across the scene may converge at the same iteration, highlighting the value of a non-iterative approach.

The SIMilarity Environment Correction (SIMEC) approach also employs the PSF from Vermote et al. (2006), but it compensates for the function's limitations by comparing the retrieved spectra with the spectral shape of deep natural waters (Sterckx et al., 2011, 2015). SIMEC is incorporated in the iCOR AC processor (De Keukelaere et al., 2018). It operates on the assumption that water's spectral shape in the red-edge-to-NIR range is stable for a wide range of water biophysical properties, and that any deviation from this shape is a result of the AE or errors in atmospheric correction. Relying on two bands in the red-edge and NIR range, SIMEC iteratively adjusts the reflectance of water pixels by removing the PSF-weighted-average reflectance until a predetermined spectral shape is achieved. However, bottom reflectance in shallow waters, extreme turbidity, high algal concentrations, or sunglint can significantly alter water reflectance from the predetermined spectral shape (Sterckx et al., 2011, 2015; Paulino et al., 2022). This limits the use of SIMEC for imagery captured by instruments not designed for ocean-color studies, such as Landsat 8 Operational Land Imager (OLI) and Sentinel-2 MultiSpectral Instrument (MSI), as these sensors are usually not maneuvered to minimize sunglint. In addition, SIMEC's deep-water assumption needs to be revised for applications to satellite-derived bathymetry and bottom habitat mapping, which rely on the magnitude and spectral shape of bottom reflectance. Despite significant progress, challenges thus remain in developing and applying AE correction methods. There is a need for an open-source, non-iterative, and fully physics-based adjacency-correction method that does not assume the spectral shape of the target, considers multiple scattering, and utilizes up-to-date ancillary atmosphere and aerosol data.

Here we derive a set of equations to perform AE correction with fewer assumptions and approximations than the studies described above, and present an open-source preprocessing tool that implements them as an addition to the Topography-adjusted Monte-carlo Adjacency-effect Radiative Transfer code (T-Mart, Wu et al., 2023). The tool ingests level-1 images along with ancillary atmospheric and aerosol data from the NASA Ocean Biology Processing Group (OBPG, 2023), calculates the PSF of the atmosphere using the ancillary data for each band, and uses it to convolve the level-1 imagery. Top-of-atmosphere (TOA) reflectance is then modified to adhere to the homogeneous-surface assumption implicit in most AC tools, i.e., pixels are corrected to the TOA reflectance they would have if surrounded by pixels of identical reflectance. The operation is done at the TOA-reflectance level; it can thus be followed by AC tools of the user’s choice, maximizing the AC efforts developed for different environmental conditions. For example, POLYMER performs well in moderately glint-covered environments (Steinmetz and Ramon, 2018), and ACOLITE performs well in productive waters (Pahlevan et al., 2021). The tool currently supports Sentinel-2 MSI, Landsat 8/9 OLI, and PRISMA data products, and is freely available on GitHub.

We first present the methodology behind the AE correction, and then demonstrate its utility by comparing surface reflectance derived by three state-of-the-art AC processors, with and without prior AE correction, against *in situ* measurements from a global dataset. Sentinel-2 MSI and Landsat 8 OLI imagery were selected for evaluation due to their relatively high spatial resolution and abundant matchups with *in situ* reflectance spectra. The focus of this article is not to compare the performance of the three AC processors, but rather to demonstrate the improvements AE correction offers to products derived from each processor.

2.2 Methods

Table 2.1. Symbols and acronyms used in this article.

Symbol	Definition
ρ_{TOA}	Measured at-sensor reflectance at the TOA level
$\rho_{\text{TOA-AE-free}}$	Adjacency-effect-free ρ_{TOA}
$\rho_{\text{TOA}}^{\text{RA}}$	Atmospheric intrinsic reflectance due to Rayleigh and aerosol scattering at the TOA level
ρ'_{TOA}	Surface reflectance propagated to the TOA level
$\rho'_{\text{TOA-AE-free}}$	Adjacency-effect-free ρ'_{TOA}
$\rho_{\text{TOA}}^{\text{dir}}$	Director component of ρ'_{TOA}
$\rho_{\text{TOA}}^{\text{diff}}$	Diffuse component of ρ'_{TOA}
ρ_s	Surface reflectance of the target pixel
ρ_s^u	Surface reflectance of an infinite uniform Lambertian target
ρ_s^{env}	PSF-weighted average surface reflectance around the target pixel
ρ_w	Water-leaving reflectance
R_{rs}	Remote sensing reflectance (sr^{-1})
S	Spherical albedo of the atmosphere
α	Wavelength-dependent scaling factor used in adjacency-effect correction
cc	Fraction of at-sensor diffuse radiation that comes from the central cell of the PSF
T_{RA}	Total upward or downward atmospheric transmittance due to Rayleigh and aerosol scattering and absorption
t_d	Diffuse upward transmittance
τ	Combined atmospheric aerosol and molecular optical thickness
μ_s	Cosine of the solar zenith angle
μ_v	Cosine of the view zenith angle
AC	Atmospheric correction
AE	Adjacency effect
AOT	Aerosol optical thickness
AOT_{550}	Aerosol optical thickness at 550 nm
Chl-a	Chlorophyll-a
NIR	Near infrared
PSF	Point-spread function
SWIR	Shortwave infrared
TOA	Top of atmosphere
TSS	Total suspended solids
β	Symmetric signed percentage bias (%)
ε	Median symmetric accuracy (%)
RMSE	Root mean squared error

2.2.1 Adjacency-effect correction

In this section, we derive a set of equations to perform AE correction. These are first summarized in Section 2.2.1.1, followed by a detailed derivation in Section 2.2.1.2. Variables are defined in both sections for readability.

2.2.1.1 Derived equations

The output of the AE correction algorithm is the adjacency-effect-free TOA reflectance ($\rho_{\text{TOA-AE-free}}$), which represents the TOA reflectance pixels would exhibit if each pixel were surrounded by pixels of identical reflectance. The calculation of $\rho_{\text{TOA-AE-free}}$ for a single pixel is summarized in Eq. (2.1),

$$\begin{aligned}\rho_{\text{TOA-AE-free}} &= \rho_{\text{TOA}}^{\text{RA}} + \rho'_{\text{TOA-AE-free}} \frac{1 - \rho_s^{\text{env}, S}}{1 - \rho_s \cdot S}, \text{ where} \\ \rho'_{\text{TOA-AE-free}} &= \rho'_{\text{TOA}} - \alpha (\rho'_{\text{TOA}} * \text{PSF} - \rho'_{\text{TOA}}), \text{ where} \\ \rho'_{\text{TOA}} &= \rho_{\text{TOA}} - \rho_{\text{TOA}}^{\text{RA}} \text{ and } \alpha = (1 - cc) \frac{t_d(\mu_v)}{\exp(-\tau/\mu_v)}.\end{aligned}\quad (2.1)$$

In Eq. (2.1), $\rho_{\text{TOA}}^{\text{RA}}$ is the atmospheric intrinsic reflectance due to Rayleigh and aerosol scattering at the TOA level, ρ_s is the surface reflectance of the target pixel, ρ_s^{env} is the PSF-weighted average surface reflectance around the target pixel, S is the spherical albedo of the atmosphere, PSF is the atmospheric point-spread function, ρ_{TOA} is the measured at-sensor reflectance at the TOA level, cc represents the fraction of at-sensor diffuse radiation that comes from the central cell of the PSF where the target pixel is located, t_d is the diffuse upward transmittance, τ is the combined atmospheric aerosol and molecular optical thickness, and μ_v is the cosine of the view zenith angle. Detailed derivation of Eq. (2.1) is presented in Section 2.2.1.2.

2.2.1.2 Derivation

When the surface is uniform and Lambertian, the measured at-sensor spectral reflectance at the TOA level (upwelling radiance multiplied by π and divided by downwelling irradiance, dimensionless), ρ_{TOA} , can be expressed as (Vermote et al., 1997a):

$$\rho_{\text{TOA}} = \rho_{\text{TOA}}^{\text{RA}} + \frac{\rho_s^u \cdot T_{\text{RA}}(\mu_s) \cdot T_{\text{RA}}(\mu_v)}{1 - \rho_s^u \cdot S} \quad (2.2)$$

where $\rho_{\text{TOA}}^{\text{RA}}$ is the atmospheric intrinsic reflectance due to Rayleigh and aerosol scattering at the TOA level, ρ_s^u is the reflectance of an infinite uniform Lambertian target, $T_{\text{RA}}(\mu_s)$ and $T_{\text{RA}}(\mu_v)$ are the total downward and upward atmospheric transmittances with μ_s and μ_v being the cosine of the solar zenith angle and view zenith angle, respectively, and S is the spherical albedo of the atmosphere. All these variables except the zenith angles have a wavelength dependence, which is omitted here and after for brevity. Symbols and acronyms are summarized in Table 2.1.

When considering surface heterogeneity, ρ_{TOA} can be rewritten by decoupling the signals coming directly from the target from those coming from adjacent areas and scattered into the target-sensor path (Vermote et al., 1997a):

$$\rho_{\text{TOA}} = \rho_{\text{TOA}}^{\text{RA}} + \frac{\rho_s \cdot T_{\text{RA}}(\mu_s) \cdot \exp(-\tau/\mu_v) + \rho_s^{\text{env}} \cdot T_{\text{RA}}(\mu_s) \cdot t_d(\mu_v)}{1 - \rho_s^{\text{env}} \cdot S} \quad (2.3)$$

where ρ_s is the surface reflectance of the target pixel, τ is the combined atmospheric aerosol and molecular optical thickness, $t_d(\mu_v)$ is the diffuse upward transmittance which is a function of μ_v , and ρ_s^{env} is the PSF-weighted average surface reflectance around the target pixel. The size of the target pixel is assumed to be infinitesimally small in Eq. (2.3) because ρ_s does not contribute to diffuse radiation at the TOA level in the equation and ρ_s^{env} is calculated for a continuous surface, as shown in Eqs. (2.4) and (2.5). This assumption is removed starting in Eq. (2.16). For a continuous surface, ρ_s^{env} at (x_0, y_0) can be expressed as,

$$\rho_s^{\text{env}}(x_0, y_0) = \int_{-\infty}^{+\infty} \int_{-\infty}^{+\infty} \rho_s(x, y; x_0, y_0) \cdot \text{PSF}(x, y; x_0, y_0; \mu_v) dx dy \quad (2.4)$$

where $\rho_s(x, y; x_0, y_0)$ is the surface reflectance located at coordinates (x, y) in reference to the target at (x_0, y_0) , and $\text{PSF}(x, y; x_0, y_0; \mu_v)$ is the weight of the atmospheric PSF at (x, y) towards the target at (x_0, y_0) , i.e., the percent contribution to the diffuse transmission per unit area of an isotropic source placed at (x_0, y_0) . The PSF can be expressed as a double integral over the x and y directions, with the weights summed to 1:

$$\int_{-\infty}^{+\infty} \int_{-\infty}^{+\infty} \text{PSF}(x, y; x_0, y_0; \mu_v) dx dy = 1. \quad (2.5)$$

Since $\rho_{\text{TOA}}^{\text{RA}}$ describes photons that never reach the surface, it is independent of the adjacency problem and thus can be temporarily removed from the TOA reflectance in Eq. (2.3) in the AE correction,

$$\rho'_{\text{TOA}} = \rho_{\text{TOA}} - \rho_{\text{TOA}}^{\text{RA}} = \frac{\rho_s \cdot T_{\text{RA}}(\mu_s) \cdot \exp(-\tau/\mu_v) + \rho_s^{\text{env}} \cdot T_{\text{RA}}(\mu_s) \cdot t_d(\mu_v)}{1 - \rho_s^{\text{env}} \cdot S} \quad (2.6)$$

where ρ'_{TOA} is the surface reflectance propagated to the TOA level. For brevity, we separate the direct and diffuse components of ρ'_{TOA} in Eq. (2.6),

$$\begin{aligned} \rho'_{\text{TOA}} &= \rho_{\text{TOA}}^{\text{dir}}(\rho_s) + \rho_{\text{TOA}}^{\text{diff}}(\rho_s^{\text{env}}), \text{ where} \\ \rho_{\text{TOA}}^{\text{dir}}(\rho_s) &= \frac{\rho_s \cdot T_{\text{RA}}(\mu_s) \cdot \exp(-\tau/\mu_v)}{1 - \rho_s^{\text{env}} \cdot S}, \text{ and} \\ \rho_{\text{TOA}}^{\text{diff}}(\rho_s^{\text{env}}) &= \frac{\rho_s^{\text{env}} \cdot T_{\text{RA}}(\mu_s) \cdot t_d(\mu_v)}{1 - \rho_s^{\text{env}} \cdot S}. \end{aligned} \quad (2.7)$$

As an essential step of the AE correction, ρ'_{TOA} is convolved with the PSF as the kernel. The convolved form, $\rho'_{\text{TOA}} * \text{PSF}$, can be expressed as,

$$\rho'_{\text{TOA}} * \text{PSF} = \rho_{\text{TOA}}^{\text{dir}}(\rho_s) * \text{PSF} + \rho_{\text{TOA}}^{\text{diff}}(\rho_s^{\text{env}}) * \text{PSF}. \quad (2.8)$$

The spatial dependence of ρ'_{TOA} , ρ_s , and ρ_s^{env} during the convolution process is omitted in Eq. (2.8) for brevity; unless specified otherwise, henceforth all reflectance terms refer exclusively to the target pixel when a convolution is involved. The convolution process assumes horizontal homogeneity of aerosols in the scene, an assumption commonly made in AC processes (Ganter et al., 2010; Vidot and Santer, 2005; Sterckx et al., 2015); the need for such an assumption is discussed in Section 2.4.5. Substituting Eq. (2.4) into Eq. (2.8), we get an updated version of Eq. (2.8),

$$\begin{aligned} \rho'_{\text{TOA}} * \text{PSF} &= \rho_{\text{TOA}}^{\text{dir}}(\rho_s^{\text{env}}) + \rho_{\text{TOA}}^{\text{diff}}(\rho_s^{\text{env}}) * \text{PSF}, \text{ where} \\ \rho_{\text{TOA}}^{\text{dir}}(\rho_s^{\text{env}}) &= \frac{\rho_s^{\text{env}} \cdot T_{\text{RA}}(\mu_s) \cdot \exp(-\tau/\mu_v)}{1 - \rho_s^{\text{env}} \cdot S}. \end{aligned} \quad (2.9)$$

In practice, pixels have a non-negligible size and there is a finite number of pixels. The corresponding PSF is then a matrix with the weights still summed to 1:

$$\sum_{x=-X}^X \sum_{y=-Y}^Y \text{PSF}(x, y; x_0, y_0; \mu_v) = 1 \quad (2.10)$$

where X and Y are the extents of the image in x and y directions, respectively. Detailed computation of PSFs is presented in Section 2.2.2. For each target pixel, the convolution process multiplies each pixel value within the PSF's range by its corresponding PSF weight and sums up all these products over both x and y directions. For example, $\rho_{\text{TOA}}^{\text{diff}}(\rho_s^{\text{env}}) * \text{PSF}$ in Eqs. (2.8) and (2.9) for the target pixel located at (x_0, y_0) can be expressed as,

$$\begin{aligned} \rho_{\text{TOA}}^{\text{diff}}(\rho_s^{\text{env}}(x_0, y_0)) * \text{PSF} \\ = \sum_{x=-X}^X \sum_{y=-Y}^Y \rho_{\text{TOA}}^{\text{diff}}(\rho_s^{\text{env}}(x, y; x_0, y_0)) \cdot \text{PSF}(x, y; x_0, y_0; \mu_v) \end{aligned} \quad (2.11)$$

where $\rho_{\text{TOA}}^{\text{diff}}(\rho_s^{\text{env}}(x, y; x_0, y_0))$ is the value of $\rho_{\text{TOA}}^{\text{diff}}(\rho_s^{\text{env}})$ located at coordinates (x, y) in reference to the target pixel at (x_0, y_0) .

The core of the described AE correction is to use ρ'_{TOA} in Eq. (2.7) and its convolved form, $\rho'_{\text{TOA}} * \text{PSF}$ in Eq. (2.9), to derive the adjacency-effect-free surface reflectance propagated to the TOA level, $\rho'_{\text{TOA-AE-free}}$, which is defined as:

$$\begin{aligned} \rho'_{\text{TOA-AE-free}} &= \frac{\rho_s \cdot T_{\text{RA}}(\mu_s) \cdot T_{\text{RA}}(\mu_v)}{1 - \rho_s^{\text{env}} \cdot S} = \rho_{\text{TOA}}^{\text{dir}}(\rho_s) + \rho_{\text{TOA}}^{\text{diff}}(\rho_s), \text{ where} \\ \rho_{\text{TOA}}^{\text{diff}}(\rho_s) &= \frac{\rho_s \cdot T_{\text{RA}}(\mu_s) \cdot t_d(\mu_v)}{1 - \rho_s^{\text{env}} \cdot S}. \end{aligned} \quad (2.12)$$

In Eq. (2.12), ρ_s^{env} instead of ρ_s is in the denominator of both direct and diffuse components of $\rho'_{\text{TOA-AE-free}}$, meaning that the change in surface irradiance due to spherical albedo and surface heterogeneity is not yet corrected for; this is addressed later in Eq. (2.20). When the surface is

homogeneous, i.e., the surrounding environment has the same spectral properties as the target, ρ'_{TOA} , $\rho'_{\text{TOA}} * \text{PSF}$, and $\rho'_{\text{TOA-AE-free}}$ are all equal. When the surface is heterogeneous, their values can be different, and we denote the ratio of the difference between ρ'_{TOA} and $\rho'_{\text{TOA-AE-free}}$ (A in Fig. 2.1) to the difference between $\rho'_{\text{TOA}} * \text{PSF}$ and ρ'_{TOA} (B in Fig. 2.1) as α :

$$\alpha = \frac{A}{B} = \frac{\rho'_{\text{TOA}} - \rho'_{\text{TOA-AE-free}}}{\rho'_{\text{TOA}} * \text{PSF} - \rho'_{\text{TOA}}}. \quad (2.13)$$

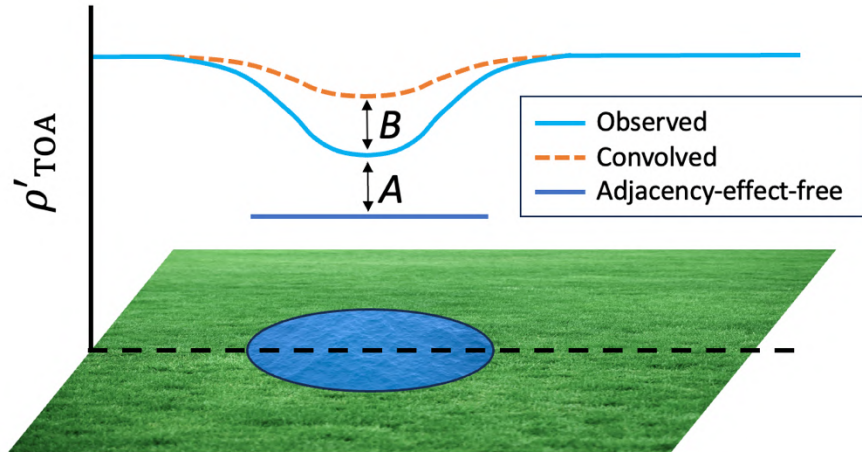


Fig. 2.1. Illustration of the removal of the adjacency effect from TOA reflectance. ρ'_{TOA} denotes surface reflectance propagated to the TOA level. Variables A and B represent the numerator and denominator of Eq. (2.13), respectively. The ratio of A to B , or α in Eq. (2.13), determines the magnitude of adjacency-effect correction to be made.

Once α and the PSF are obtained, $\rho'_{\text{TOA-AE-free}}$ can be calculated for each pixel by rearranging Eq. (2.13),

$$\rho'_{\text{TOA-AE-free}} = \rho'_{\text{TOA}} - \alpha(\rho'_{\text{TOA}} * \text{PSF} - \rho'_{\text{TOA}}). \quad (2.14)$$

Here we first attempt to solve for α while preserving the assumption of infinitesimally small pixel size. Substituting Eq. (2.7), (2.9), and (2.12) into Eq. (2.13), we get Eq. (2.15) which solves for α ,

$$\alpha = \frac{\rho_{\text{TOA}}^{\text{diff}}(\rho_s^{\text{env}}) - \rho_{\text{TOA}}^{\text{diff}}(\rho_s)}{\rho_{\text{TOA}}^{\text{dir}}(\rho_s^{\text{env}}) - \rho_{\text{TOA}}^{\text{dir}}(\rho_s) + \rho_{\text{TOA}}^{\text{diff}}(\rho_s^{\text{env}}) * \text{PSF} - \rho_{\text{TOA}}^{\text{diff}}(\rho_s^{\text{env}})}. \quad (2.15)$$

Removing the assumption of infinitesimally small pixel size, we now denote the weight of the central cell in the convolution kernel as cc . Variable cc characterizes the amount of at-sensor diffuse radiation that comes from the target pixel, ρ_s . This amount is usually small but can be non-negligible for large pixel sizes, ranging from 0.003 to 0.006 for 10-m resolution sensors, 0.01 to 0.02 for 30-m resolution sensors, and 0.1 to 0.3 for 1000-m resolution sensors from

visible to NIR wavelengths, under common coastal satellite-observation conditions with maritime or continental aerosols and an AOT₅₅₀ between 0.05 and 0.3, according to T-Mart simulations (Section 2.2.2). With a non-negligible cc , we add the diffuse radiation from ρ_s to $\rho_{\text{TOA}}^{\text{diff}}(\rho_s^{\text{env}})$ and remove the corresponding contribution from ρ_s^{env} ,

$$\rho_{\text{TOA}}^{\text{diff}}(\rho_s^{\text{env}}) \rightarrow (1 - cc) \cdot \rho_{\text{TOA}}^{\text{diff}}(\rho_s^{\text{env}}) + cc \cdot \rho_{\text{TOA}}^{\text{diff}}(\rho_s). \quad (2.16)$$

With the change in Eq. (2.16) and following Eq. (2.4), ρ'_{TOA} in Eq. (2.7) and $\rho'_{\text{TOA}} * PSF$ in Eq. (2.9) now become,

$$\begin{aligned} \rho'_{\text{TOA}} &= \rho_{\text{TOA}}^{\text{dir}}(\rho_s) + (1 - cc) \cdot \rho_{\text{TOA}}^{\text{diff}}(\rho_s^{\text{env}}) + cc \cdot \rho_{\text{TOA}}^{\text{diff}}(\rho_s) \\ \rho'_{\text{TOA}} * PSF &= \rho_{\text{TOA}}^{\text{dir}}(\rho_s^{\text{env}}) + (1 - cc) \cdot \rho_{\text{TOA}}^{\text{diff}}(\rho_s^{\text{env}}) * PSF + cc \cdot \rho_{\text{TOA}}^{\text{diff}}(\rho_s^{\text{env}}). \end{aligned} \quad (2.17)$$

Substituting Eq. (2.12) and (2.17) into Eq. (2.13), we then get an updated version of Eq. (2.15) that considers the contribution of diffuse radiation from the target pixel,

$$\begin{aligned} \alpha &= \frac{(1 - cc) \cdot [\rho_{\text{TOA}}^{\text{diff}}(\rho_s^{\text{env}}) - \rho_{\text{TOA}}^{\text{diff}}(\rho_s)]}{\rho_{\text{TOA}}^{\text{dir}}(\rho_s^{\text{env}}) - \rho_{\text{TOA}}^{\text{dir}}(\rho_s) + (1 - cc) \cdot U_1 + cc \cdot U_2} \text{ with} \\ U_1 &= \rho_{\text{TOA}}^{\text{diff}}(\rho_s^{\text{env}}) * PSF - \rho_{\text{TOA}}^{\text{diff}}(\rho_s^{\text{env}}) \\ U_2 &= \rho_{\text{TOA}}^{\text{diff}}(\rho_s^{\text{env}}) - \rho_{\text{TOA}}^{\text{diff}}(\rho_s). \end{aligned} \quad (2.18)$$

Eq. (2.18) is a closed-form expression of α ; however, in practice, $(1 - cc) \cdot U_1$ and $cc \cdot U_2$ are difficult to solve as they require characterization of surface reflectance for an area equal to or larger than the PSF's range. Excluding the two terms leads to a bias approximately an order of magnitude smaller than the noise levels of OLI and MSI in the visible-to-SWIR range because the terms are negligible compared to $\rho_{\text{TOA}}^{\text{dir}}(\rho_s^{\text{env}}) - \rho_{\text{TOA}}^{\text{dir}}(\rho_s)$ (Supplementary material 1). After removing $(1 - cc) \cdot U_1$ and $cc \cdot U_2$, Eq. (2.18) can be simplified to,

$$\alpha = (1 - cc) \frac{t_d(\mu_v)}{\exp(-\tau/\mu_v)}. \quad (2.19)$$

Eq. (2.19) shows that the magnitude of the AE correction depends on the ratio of diffuse transmittance to direct transmittance. It is also reduced by cc , as diffuse radiation from the target itself does not need to be corrected for.

The three parameters needed to calculate α in Eq. (2.19) are cc , t_d , and τ (as μ_v comes from the image metadata). All the three parameters are calculated through radiative transfer modeling in T-Mart (Wu et al., 2023) with the following input:

- Sun-sensor geometry: from image metadata,
- Sensor resolution and band spectral responses: from image metadata,
- Atmospheric information: ozone and water vapor concentrations are automatically retrieved from the GMAO MERRA2 meteorological dataset (Global Modeling and Assimilation Office, 2015a), hosted by the NASA Ocean Biology Processing Group (OBPG, 2023), and

- Aerosol information: Angstrom exponent and single-scattering albedo from the GMAO MERRA2 aerosol dataset (Global Modeling and Assimilation Office, 2015b) are automatically retrieved and used to linearly interpolate the aerosol composition by linearly mixing continental and maritime aerosols (details in Supplementary material 2); mixed aerosols allow for a smooth transition from land to water. Aerosol optical thickness at 550 nm (AOT_{550}) is also retrieved from the same dataset.

Aerosol composition, AOT_{550} , and ozone and water vapor concentrations are linearly interpolated in time, and are used to compute the optical properties of the atmosphere for each band using 6S through the Py6S Python interface (Wilson, 2013).

While calculating the three AE correction parameters, T-Mart also calculates ρ_{TOA}^{RA} , which is used for calculating ρ'_{TOA} in Eq. (2.6), as well as the PSF needed for calculating $\rho'_{TOA} * PSF$. By default, 100,000 photons are launched in each band-specific simulation in T-Mart for these calculations. This setup has been validated against the discrete-ordinate solver in libRadtran (Emde et al., 2016), demonstrating a maximum difference of 0.6 % in extreme optical settings (Wu et al., 2023).

After calculating α in Eq. (2.19), $\rho'_{TOA-AE-free}$ in Eq. (2.14) can be calculated. We then add ρ_{TOA}^{RA} back to the equation and correct for the change in ground-level irradiance due to surface heterogeneity,

$$\begin{aligned}\rho_{TOA-AE-free} &= \rho_{TOA}^{RA} + \frac{\rho_s \cdot T_{RA}(\mu_s) \cdot T_{RA}(\mu_v)}{1 - \rho_s \cdot S} \\ &= \rho_{TOA}^{RA} + \rho'_{TOA-AE-free} \cdot \frac{1 - \rho_s^{\text{env}} \cdot S}{1 - \rho_s \cdot S}\end{aligned}\quad (2.20)$$

where $\rho_{TOA-AE-free}$ is the adjacency-effect-free TOA reflectance, which is the output of the algorithm and conforms to the surface-homogeneity assumption. In Eq. (2.20), the calculation of $(1 - \rho_s^{\text{env}} \cdot S)/(1 - \rho_s \cdot S)$ for all pixels across a scene is done by computing a scene-specific lookup table for each band. A scene-wide $(1 - \rho_s^{\text{env}} \cdot S)$ is calculated with the first-estimate scene-average surface reflectance employed as ρ_s^{env} , and $(1 - \rho_s \cdot S)$ is calculated for ρ_s at 0, 0.25, 0.5, 0.75, and 1 for interpolation. The value of $(1 - \rho_s^{\text{env}} \cdot S)/(1 - \rho_s \cdot S)$ is then linearly interpolated by employing the 2D array of $\frac{\rho'_{TOA-AE-free}}{T_{RA}(\mu_s) \cdot T_{RA}(\mu_v)}$ as ρ_s . Lastly, the irradiance correction is completed in an element-wise multiplication of the two arrays $\rho'_{TOA-AE-free}$ and $(1 - \rho_s^{\text{env}} \cdot S)/(1 - \rho_s \cdot S)$.

In the image being processed, ρ_{TOA} is replaced by $\rho_{TOA-AE-free}$ for each water pixel as the final step of the correction. Identification of water pixels follows ACOLITE (Vanhellemont, 2023), with the following criteria: 1) $\rho_{TOA} < 0.3$ in all bands, 2) ρ_{TOA} at 1600 nm < 0.0215 , and 3) ρ_{TOA} in the cirrus band at 1373 nm < 0.005 , if available. By default, land pixels remain unchanged throughout the correction to facilitate the existing calibration of processors that extract information from land pixels, such as the dark spectrum fitting technique in ACOLITE that sometimes retrieves AOT from shadowed pixels (Vanhellemont and Ruddick, 2018). The option of AE correction for all pixels, including both land and water, is available in the tool's settings.

2.2.2 Calculation of the atmospheric point-spread function

The RTM solver in T-Mart is used to calculate the wavelength-dependent atmospheric PSF. For one band or wavelength at a time, a PSF is determined using atmospheric optical properties and the observation geometry as inputs. Ancillary ozone and water vapor concentrations, as well as aerosol loading and composition, are first used to construct the optical properties of the atmosphere (Section 2.2.1.2). User-defined gas and aerosol settings are also supported. These optical properties are calculated for each band, given the sensor's spectral response functions, using 6S via the Py6S Python interface (Wilson, 2013).

The PSF in T-Mart (Wu et al., 2023) is a square matrix of numerical values centered on the target pixel. The sum of the values in a PSF is normalized to 1, with the central cell, where the target pixel is located, usually having the largest weight. The calculation of the PSF employs a backward Monte Carlo radiative transfer solver. For each band, photons are launched from the sensor towards the target, following the sensor's viewing direction. Each photon carries an initial weight of 1 upon entering the atmosphere, with the weight decreasing as the photon travels through the atmosphere due to absorption. Photons that reach the surface after at least one scattering event in the atmosphere are tallied. A grid centered on the target pixel is generated, with photons binned in the grid according to their coordinates relative to the target (Eq. (2.10)). In each cell, the sum of the photons' remaining weights constitutes the cell's value in the PSF matrix. An example PSF at 400 nm is provided in Fig. 2.2; PSFs at longer wavelengths are typically more pointed due to the stronger forward scattering of aerosols at longer wavelengths.

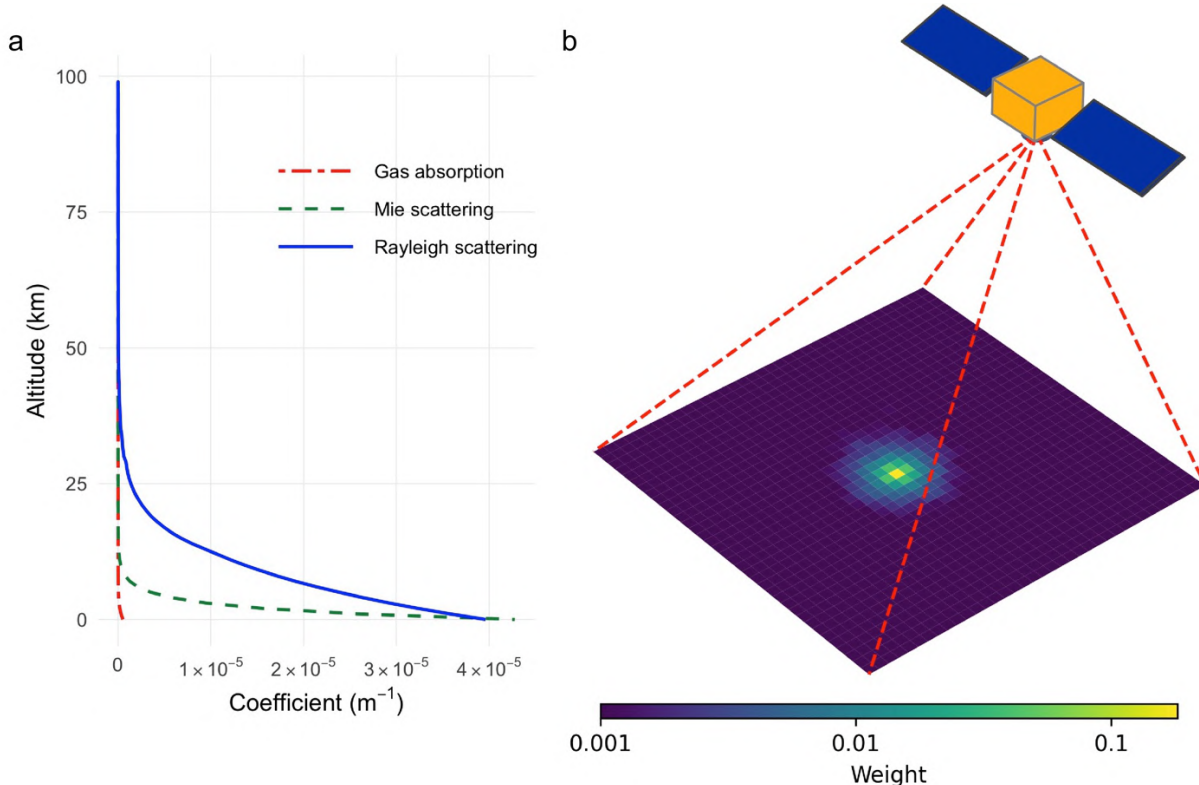


Fig. 2.2. Example atmospheric optical properties and atmospheric point-spread function (PSF) at 400 nm. (a) Scattering and absorption coefficients as a function of altitude. (b) A normalized PSF with a width and height

of 36 km, where the weights of all cells sum to 1. The resolution of the PSF is reduced here to illustrate its matrix structure; actual processing uses the sensor's resolution. Settings: mid-latitude summer atmosphere, maritime aerosol composition, $AOT_{550} = 0.1$, solar zenith angle = 45° , view zenith angle = 170° , and relative azimuth angle = 45° .

By default, the PSF is stored in a 36×36 km matrix with the sensor's resolution as the cell size; this can be modified by the user. The 36×36 km range was chosen to balance performance and computational cost. Tanré et al. (1987) demonstrated that approximately 50 % of environmental radiance comes from the adjacent area within a 1 km radius of the target, with the rate of increase dropping as the radius extends, covering over 80 % and 90 % of environmental radiance within a 10 km radius of the target at 450 nm and 850 nm, respectively, under various atmospheric conditions. The at-sensor diffuse radiance from outside the kernel (approximately 0.1-5 % of the total at-sensor diffuse radiance from shortwave infrared (SWIR) to visible bands) is included by assuming it follows the same spatial pattern and magnitude as the at-sensor diffuse radiance within the kernel. To ensure AE correction is applied across the entire image, pixel values outside the scene were assumed to be homogeneously equal to the scene-average ρ'_{TOA} when convolving ρ'_{TOA} near the edges. The PSF spans 1201×1201 pixels for the 30 m Landsat 8 OLI bands and 3601×3601 pixels for the 10 m Sentinel-2 MSI bands, each covering a window slightly larger than 36×36 km. This ensures that the PSF dimensions are odd numbers. For bands with different spatial resolutions, such as the 20 m and 60 m MSI bands, the PSF sizes are adjusted accordingly to maintain the 36×36 km coverage.

2.2.3 Validation

2.2.3.1 *In situ* dataset

Validation of the AE-correction tool was conducted by deriving water-leaving reflectance (ρ_w) using three state-of-the-art AC processors, with and without AE correction, and comparing the results to globally distributed *in situ* remote sensing reflectance (R_{rs}) measurements from the GLORIA dataset (Lehmann et al., 2023). The two radiometric quantities, ρ_w and R_{rs} , are defined and related as

$$\rho_w = \pi \cdot L_w^{0+} / E_d^{0+} = \pi \cdot R_{\text{rs}} \quad (2.21)$$

where L_w^{0+} and E_d^{0+} are the water-leaving radiance and down-welling irradiance right above the water surface, respectively (Mobley, 2022).

Google Earth Engine (Gorelick et al., 2017) was first used to identify matchups between *in situ* measurements from GLORIA, excluding the spectra flagged as ‘Suspect’ for quality control, and Sentinel-2 and Landsat 8 satellite overpasses. The criteria used to identify matchups were: 1) only *in situ* measurements within 200 m of shores, where the AE is most prominent, were included to investigate the performance of AE correction; 2) the built-in cloud masks of the level-1 MSI and OLI products were used to remove cloud-covered *in situ* measurements; and 3) the maximum allowed time difference between an *in situ* measurement and a satellite overpass was six hours. The number of matchups decreases with distance from shore (Fig. S5.1); analysis

of samples collected beyond 200 m from shore, up to 5 km, is included in Supplementary material 5 and summarized in Section 2.4.3. Although some studies have recommended three-hour time windows for matchups (Bailey and Werdell, 2006; Müller et al., 2015), there were approximately twice as many matchups in the three-to-six-hour range as there were within the zero-to-three-hour range. Some studies suggested time windows as long as 24 h (Warren et al., 2019) and 30 h (Pahlevan et al., 2021) could work for nearshore waters under stable hydrologic and atmospheric conditions. To balance sample size and temporal proximity, a six-hour time window was used for the evaluation of the tool for both sensors.

A total of 212 *in situ* measurements concurrent with 40 Sentinel-2 and 30 Landsat 8 overpasses were identified from across the globe (Fig. 2.3). Not all of them resulted in valid matchups because AC processors mask out pixels with processing errors in the output, sometimes differently across bands, leading to <212 valid matchups for each processor (Table 2.2). Detailed information on the sample size by band is included in Tables S3.1 and S3.2.



Fig. 2.3. Geographical distribution of 212 matchups from the GLORIA dataset within 200 m of shorelines and with Sentinel-2 or Landsat 8 overpasses.

Table 2.2. Sample size of matchups with and without adjacency-effect correction by atmospheric correction processor. Visible refers to bands centered between 443 and 664 nm; near-infrared (NIR) refers to bands centered between 705 and 865 nm. Hyphen denotes value ranges.

	ACOLITE	POLYMER	l2gen
Visible, without	122	177	88-94
Visible, with	125	177	84-87
NIR, without	78-110	120-157	27-44
NIR, with	81-113	120-157	27-44

All the 212 hyperspectral *in situ* R_{rs} measurements cover the 400-800 nm range, with 147 covering the 400-900 nm range. 15 of the 212 measurements were coincident with both OLI and MSI measurements. These data were convolved to match the multispectral bands of the three sensors (S2A MSI, S2B MSI, and Landsat 8 OLI) using the spectral response functions provided by their respective space agencies (ESA, 2023; Barsi et al., 2014). The distribution of distances from matchups to shore is presented in Fig. 2.4. On average, the Sentinel-2 matchups were closer to shore than the Landsat 8 matchups.

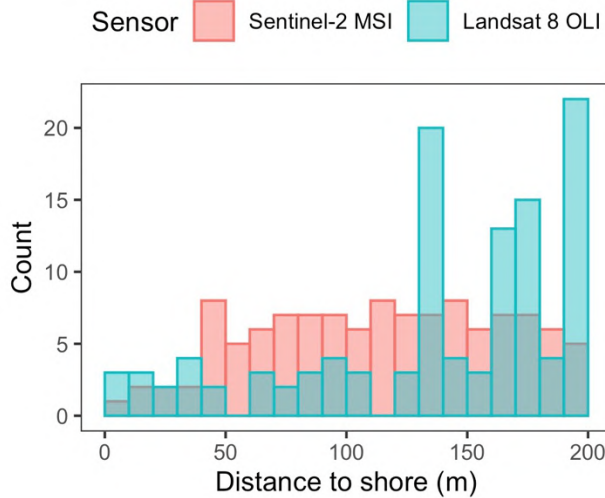


Fig. 2.4. Number of *in situ* measurements coinciding with Sentinel-2 and Landsat 8 overpasses as a function of distance to shore.

2.2.3.2 Atmospheric correction

Three state-of-the-art AC processors, ACOLITE, POLYMER, and l2gen, were selected to explore the impact of AE correction on derived ρ_w .

ACOLITE is a generic processor developed at the Royal Belgian Institute of Natural Sciences (Vanhellemont and Ruddick, 2018; Vanhellemont, 2019a), and it has shown good performance for coastal and inland water applications (Pahlevan et al., 2021). By default, ACOLITE performs the AC using the dark spectrum fitting technique, which automatically selects the band with lowest Rayleigh-corrected reflectance values to estimate AOT. Look-up tables were constructed using 6S (Vermote et al., 2006) for various observation geometry and atmospheric conditions, and atmospheric contribution interpolated from the look-up tables is removed from the TOA reflectance to derive surface-reflectance values.

POLYMER was developed at HYGEOS, France. It fits a second-order polynomial function to Rayleigh-corrected reflectance to correct for aerosol and sunglint signals simultaneously (Steinmetz et al., 2011). POLYMER first removes Rayleigh contribution from the TOA reflectance; then it combines a water reflectance model and an atmospheric reflectance model to fit the Rayleigh-corrected reflectance. The water reflectance model has two parameters, Chl-a and particle backscattering coefficient, and the atmospheric reflectance model includes aerosol and glint contributions. POLYMER optimizes five spectral-optimization parameters to best fit Rayleigh-corrected reflectance with modeled values. The final ρ_w is derived by subtracting the fitted atmospheric model from the input spectrum, making the derived ρ_w not limited to the modeled water parameters. POLYMER has demonstrated successful retrieval of ocean color information from MERIS data in the presence of intense sunglint (Steinmetz and Ramon, 2018). The relatively smooth spectral shapes of aerosol and glint confer an advantage when correcting

for both simultaneously, as this approach proves effective in minimizing errors that may arise from addressing each component individually.

l2gen, developed and maintained by NASA's Ocean Biology Processing Group, is the L1-to-L2 processing module in SeaDAS (Gordon and Wang, 1994). It is capable of performing AC and retrieving ocean color products for multiple sensors. l2gen uses a NIR and a SWIR band for aerosol estimation by assuming negligible water-leaving radiance in the two bands, attributing TOA reflectance to aerosols only to characterize them and extrapolate aerosol information to other wavelengths. Initially designed for open-ocean applications, l2gen has undergone significant improvements to characterize aerosols in various atmospheric and water-property conditions (Ahmad et al., 2010; Bailey et al., 2010; Lavender et al., 2005). These improvements enabled l2gen to derive reflectance of moderately turbid coastal waters (Jamet et al., 2011).

All MSI and OLI imagery was processed to ρ_w with the default setting in each processor to ensure the analysis stays accessible and relevant to the broader user community while avoiding the need to test multiple configurations, with the following modifications:

- ACOLITE (version: 20231023.0): glint removal was enabled, the negative- ρ_w filter was disabled to capture low reflectance with sensor noise, and NASA atmospheric ancillary data was enabled (OBPG, 2023);
- POLYMER (version: 4.16.1): ECMWF's ERA-interim atmospheric ancillary data (Dee et al., 2011) was used, because only a test version of POLYMER (4.17 beta) supports the recent update of NASA atmospheric ancillary data (OBPG, 2023) at the time of writing;
- l2gen (version: SeaDAS 8.4.1): NASA atmospheric ancillary data (OBPG, 2023) was used.

The three algorithms work with sunglint in different ways. The polynomial fitting technique in POLYMER deals with glint internally; l2gen has a glint-correction method based on sea-surface wave-slope statistics as a function of wind speed (Wang and Bailey, 2001), and ACOLITE extrapolates estimated glint reflectance from the SWIR range to NIR and visible wavelengths (Harmel et al., 2018).

ACOLITE and POLYMER use tiled processing: images are divided into tiles before performing AC in order to account for the spatial variation of aerosol properties, observation geometry, and other environmental factors. l2gen follows a pixel-based processing approach where each pixel is treated independently from neighboring pixels.

To compare with the *in situ* measurements, ρ_w was extracted from within 90 m × 90 m or 100 m × 100 m boxes surrounding the matchup location, depending on the resolution of the raw imagery and the AC-processor output. The median value of water pixels in the selected box for each band was used in the comparison with *in situ* values to remove outliers (Müller et al., 2015).

2.2.3.3 Performance metrics

We evaluated processor performance following Pahlevan et al. (2021). Two metrics were used to investigate the overall error and bias in satellite-derived water-leaving reflectance, $\hat{\rho}_w$, by comparing it with field-measured ρ_w . The symmetric signed percentage bias (β) is calculated as

$$\beta = \text{sign}(Z) \cdot (10^Z - 1) \cdot 100\% \quad (2.22)$$

where Z is the median of $\log_{10}(\hat{\rho}_w/\rho_w)$; and the median symmetric accuracy (ε) is calculated as

$$\varepsilon = (10^Y - 1) \cdot 100\% \quad (2.23)$$

where Y is the median of $|\log_{10}(\hat{\rho}_w/\rho_w)|$. The two metrics convert all paired ratios into logarithmic space before transforming them back to linear space, and they utilize median values and penalize errors in logarithmic space; they are shown to be robust to outliers and easily interpretable as percentages (Morley et al., 2018). In addition, we calculated root mean squared error (RMSE), which is a more conventional performance metric,

$$\text{RMSE} = \sqrt{\sum_{i=1}^N (\hat{\rho}_w - \rho_w)^2 / N}. \quad (2.24)$$

When calculating β and ε , negative reflectance values cannot be log-transformed and are therefore discarded in the original calculations. This becomes problematic for evaluating retrieved values that are extremely low, such as the NIR reflectance of water. For example, when ρ_w is ~ 0 and a processor successfully retrieves $\hat{\rho}_w$ centered around 0, with slight sensor and atmospheric noise, the results are biased towards overestimation if negative values are excluded. Negative retrievals were common for all three AC processors in this study (Supplementary material 4). To mitigate this, for each band with and without AE correction, the absolute value of the lowest reflectance at this wavelength, either satellite-derived or *in situ*, was added to all satellite-derived and *in situ* values (Fig. 2.5). Another 0.001 was then added to the values to force them to be positive. For each band processed by each AC processor, values with and without AE correction were incremented by the same number to ensure an unbiased comparison. If all values were positive for a band, no change was made.

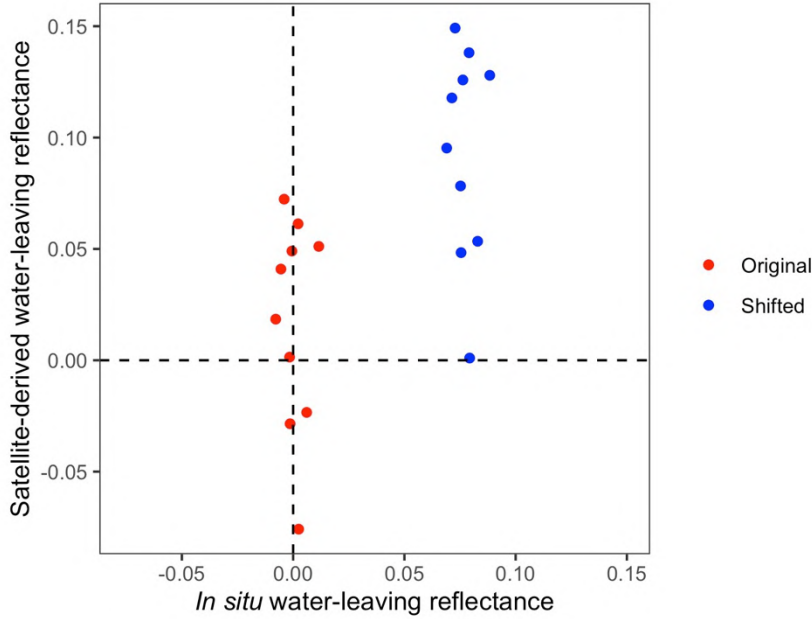


Fig. 2.5. Example of shifting values to include negative values in the calculation of β and ε . When at least one negative value is present, all values on both axes are shifted by adding the absolute value of the lowest value plus 0.001. Most of the original points in this example have negative values in at least one axis and, without such shifting, would therefore have to be removed prior to the log transformation when calculating β and ε .

The amount of improvement on all three performance metrics from AE correction was quantified as percentage change after correction, calculated as

$$\frac{|V_{\text{without}}| - |V_{\text{with}}|}{|V_{\text{without}}|} \cdot 100\% \quad (2.25)$$

where V_{with} and V_{without} are the values of the performance metrics with and without AE correction, respectively. Following Pahlevan et al. (2021), the five wavelengths shared by Sentinel-2 MSI and Landsat OLI were combined in the analysis to enhance the statistical significance. Note that the three performance metrics quantify error, and a reduction in their value indicates an improvement in AC performance.

2.3 Results

2.3.1 Performance overview

Satellite-derived water-leaving reflectance, derived with and without AE correction, was compared with *in situ* measurements. Following AE correction, the 78 values of performance metrics, for three AC processors and nine bands, were all improved except for three values for POLYMER (Fig. 2.6 and Table 2.3). On average, there was a 16.7 % reduction in RMSE, 32.4 % reduction in β , and 36.8 % reduction in ε across the three AC processors.

The change in performance varies across the processors:

- For ACOLITE, there was a >30 % reduction in all three metrics at 740, 780, 833, and 865 nm; β on average had a 64.1 % reduction across all nine bands, although it was only 0.3 % for the 705 nm band; RMSE and ε in the remaining bands, centered between 443 and 705 nm, experienced minor improvements (Fig. 2.6 and Table 2.3).
- For POLYMER, there was on average a 41.6 % reduction in β and ε at 664nm, 705 nm, 780 nm, and 865 nm. The performance was poor for β at 443 and 740 nm and RMSE at 865 nm, with 318 %, 40.5 %, and 14.2 % increases, respectively; the two increases larger than 30 % happened where the two β values were both low, changing from 4.1 % to -17.3 % for the 443 nm band and 1.9 % to -2.6 % for the 740 nm band following AE correction. There were minor improvements in the remaining bands and metrics (Fig. 2.6 and Table 2.3).
- For l2gen, the bands centered between 443 and 740 nm had on average a 58.8 % reduction in β and ε ; improvement in RMSE was moderate, ranging from 19.4 % to 29 % in the five bands from 443 and 705 nm; AE correction had almost no impact on the 833 nm band (Fig. 2.6 and Table 2.3). The 865 nm band was missing for l2gen because l2gen assumes all reflectance at this wavelength comes from aerosols, i.e. $\rho_w = 0$, in order to estimate AOTs.

Details about changes in the three metrics, reported by sensor and band, are included in Supplementary material 3.

Chapter 2: Adjacency effect correction

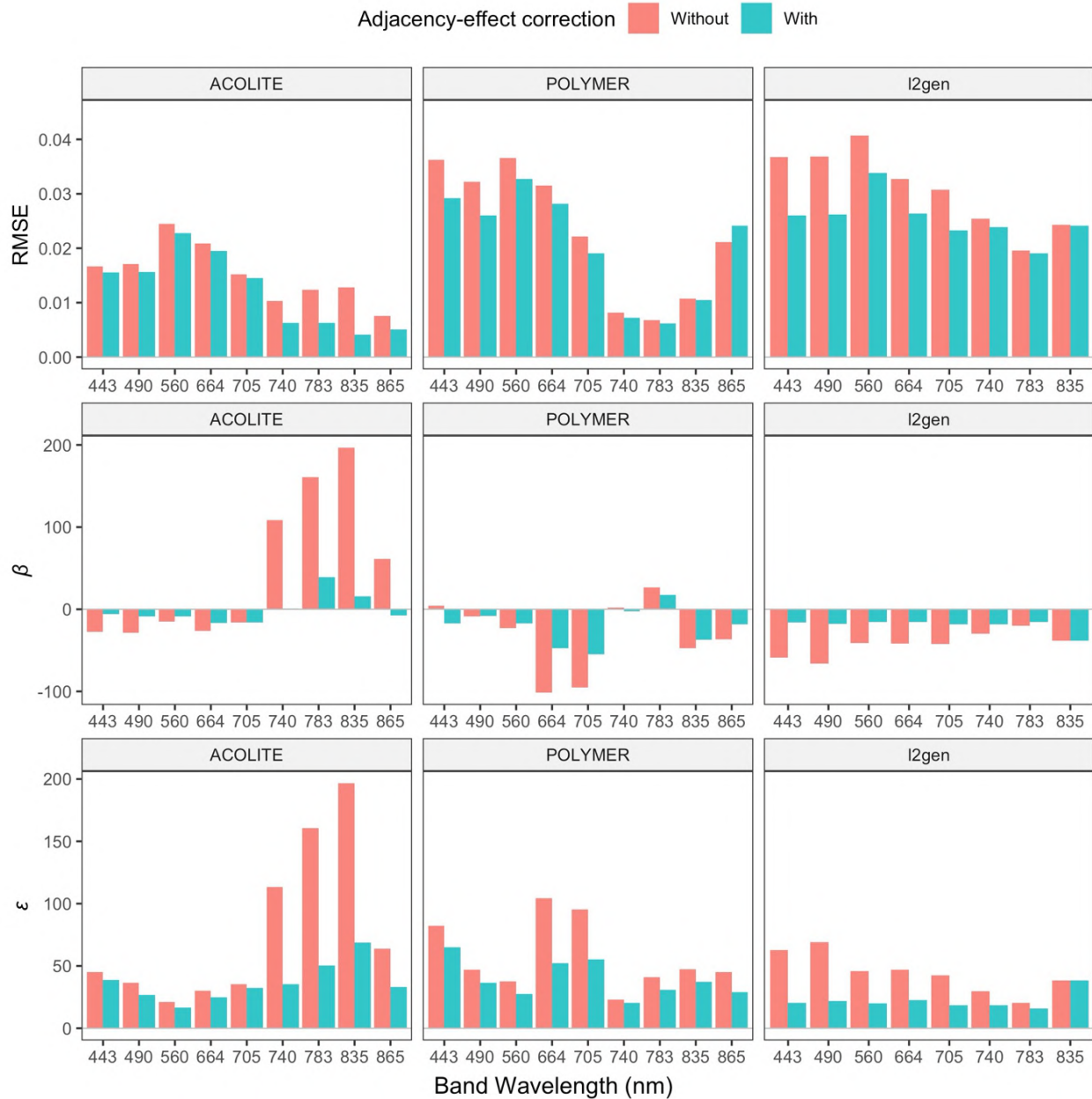


Fig. 2.6. Performance metrics with and without adjacency-effect correction, grouped by atmospheric correction processor and band wavelength. Bands at 705, 740, 783, and 835 nm are exclusive to Sentinel-2 MSI matchups, and the other bands are shared by Landsat 8 OLI and Sentinel-2 MSI.

Table 2.3. Percentage reduction of performance metrics with the implementation of adjacency-effect correction, grouped by atmospheric correction processor. Positive and negative values indicate improved and reduced performance, respectively (Eq. (2.25)). All values are in units of % change; values greater than 30 % are in bold.

	ACOLITE			POLYMER			l2gen		
	RMSE	β	ε	RMSE	β	ε	RMSE	β	ε
443 nm	7.0	78.1	14.3	19.5	-318.0	20.9	29.0	72.3	67.7
490 nm	8.6	70.2	26.4	19.3	9.2	22.3	28.9	73.2	68.6
560 nm	7.1	39.9	21.0	10.7	23.7	26.7	16.7	62.7	56.5
664 nm	6.5	35.9	17.9	10.7	53.3	50.2	19.4	62.6	52.3
705 nm	4.9	0.3	8.2	14.0	42.3	42.2	24.5	56.8	56.8
740 nm	38.8	99.1	68.7	11.7	-40.5	11.6	5.9	38.3	38.3
780 nm	49.3	75.6	68.6	8.4	35.0	24.8	2.6	22.3	22.3
833 nm	67.9	92.0	65.0	2.6	21.6	21.6	0.5	0.0	0.0
865 nm	32.9	87.2	48.4	-14.2	49.4	35.8			

2.3.2 Scatterplot comparison and additional results

Most bands from all three AC processors experienced minor to major improvements following AE correction, with points located closer to the 1:1 line when AE correction was implemented (Fig. 2.7). Certain bands experienced visually significant improvements, such as the four bands centered between 740 and 865 nm for ACOLITE, bands at 490, 664, 705, 740, and 865 nm for POLYMER, and the six bands centered between 443 and 740 nm for l2gen (Fig. 2.7). Changes in the remaining bands are less visually discernible. The retrieved MERRA2 AOT₅₅₀ for most of the images was under 0.2, with a similar distribution for MSI and OLI matchups (Fig. 2.8).

Chapter 2: Adjacency effect correction

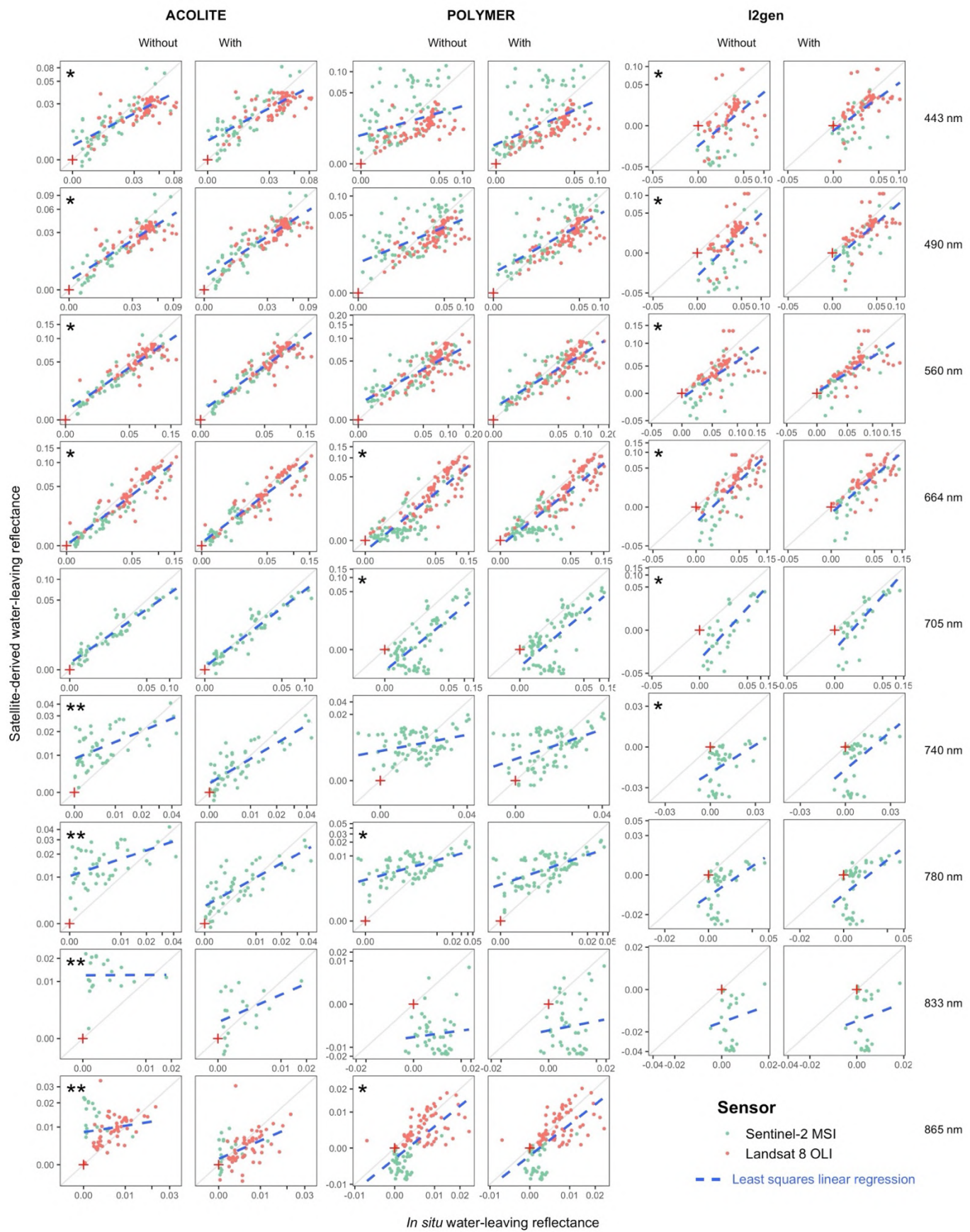


Fig. 2.7. Satellite-derived water-leaving reflectance, with and without adjacency-effect correction, compared with *in situ* values. Plots are grouped by atmospheric correction processor and band wavelength. Points are colored by satellite sensor. Blue dashed lines represent least-squares linear regression. Red crosses are located at (0,0) for visual reference. The 865 nm band is missing for l2gen as the processor assumes water-leaving reflectance at 865 nm is zero to estimate aerosol optical thickness. *: The AE correction results in a reduction of 30 % or more for at least one performance metric; **: The AE correction results in a reduction of 30 % or more for all three performance metrics.

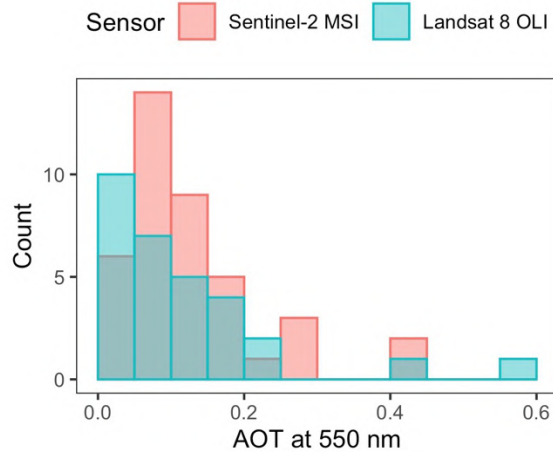


Fig. 2.8. Distribution of retrieved aerosol optical thickness at 550 nm. One value was retrieved for each image.

In some cases, changes in TOA reflectance can lead to changes in the number of negative retrievals by AC processors. For ACOLITE, around 10 % of reflectance values at NIR wavelengths changed from positive to negative with AE correction, with slightly decreased number of negative retrievals in the visible range; for l2gen, there was on average 18 % fewer negative retrievals across all bands and AC processors with AE correction; and for POLYMER, the number of negative retrievals stayed roughly the same with and without AE correction (Fig. 2.7 and Supplementary material 4).

2.3.3 Example matchups

Examples of the impact of AE correction on TOA reflectance and derived water-leaving reflectance at various distances from shore are shown in Fig. 2.9. Maps of TOA reflectance at 865 nm were included in Fig. 9 to illustrate the spatial variation of AE correction as the NIR band is often most affected by the AE (Sterckx et al., 2011); this is supported by correction at this wavelength being the largest in small waterbodies near vegetation (Fig. 2.9a, b, and e). From observing the changes in spectra following AE correction, AE correction of the TOA reflectance tends to 1) increase underestimated l2gen-derived ρ_w in the visible range (Fig. 2.9c, d, and e), with shorter wavelengths experiencing a greater increase; 2) reduce ACOLITE-derived ρ_w in the NIR range, with a small increase in the visible range (Fig. 2.9a, b, and e); and 3) for POLYMER, the changes seem to occur throughout the visible-NIR range, with visible wavelengths experiencing somewhat greater changes (Fig. 2.9a, b, and d).

Chapter 2: Adjacency effect correction

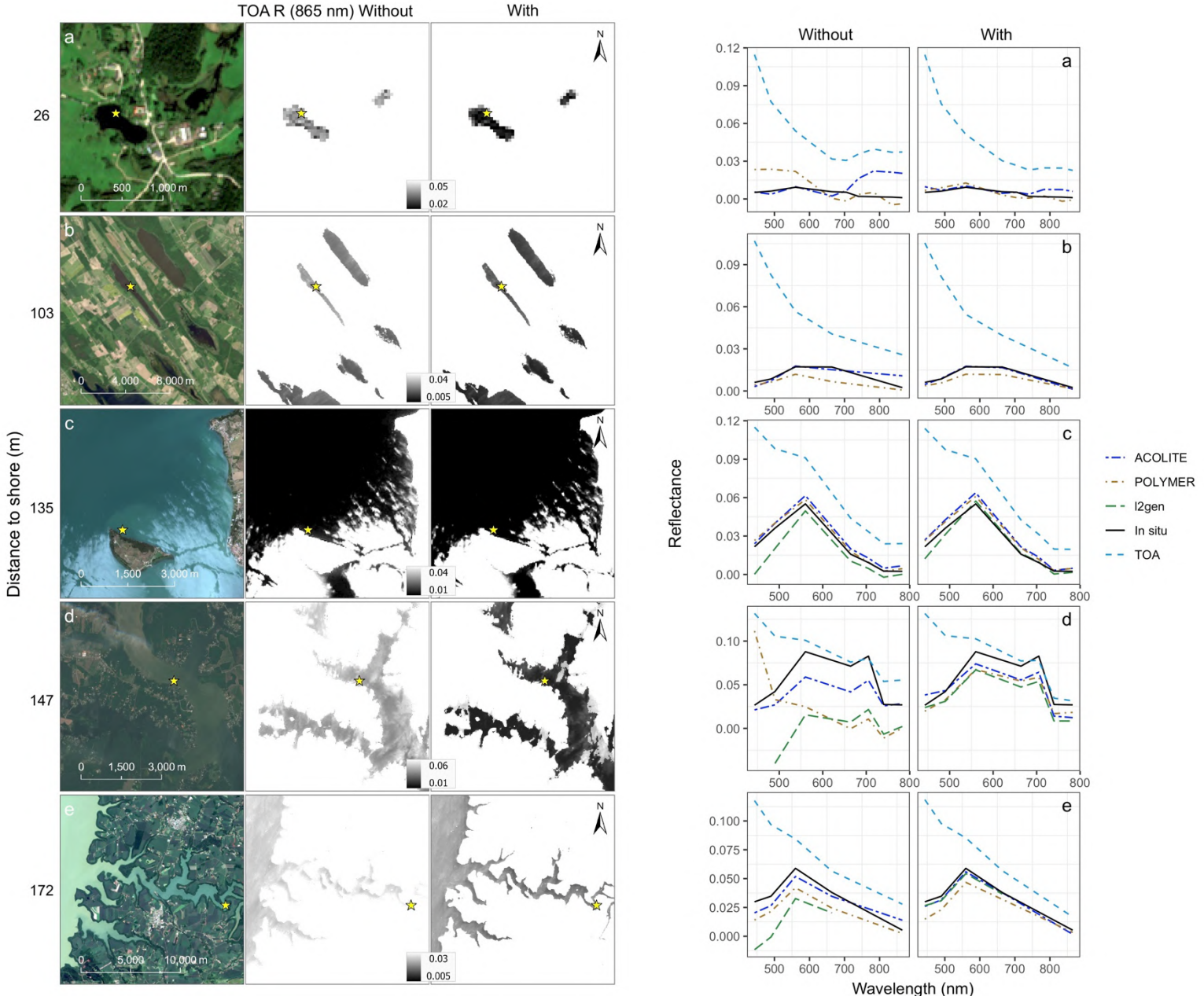


Fig. 2.9. Examples of the impact of adjacency-effect correction on TOA reflectance and water-leaving reflectance derived by three atmospheric correction processors. From left to right: RGB view of the image, TOA reflectance at 865 nm with and without adjacency-effect correction, and TOA, *in situ*, and derived water-leaving reflectance grouped by processor without and with correction. Stars on the maps represent the locations of the matchup spectra displayed on the right. Distance to shore is indicated on the left of the images. Scene IDs and aerosol optical thickness are listed in Table 2.4.

Distance to shore and AOT are two important factors in AE correction (Vermote et al., 1997a). In general, water pixels far from land experienced less correction (Fig. 2.9c and e). Fig. 2.9d shows an example of increased AE correction, at a similar distance to shore as Fig. 2.9c and e, due to a relatively large AOT_{550} of 0.266 (Table 2.4). Water pixels can be masked in the AE correction due to high aerosol loading (Fig. 2.9d).

Table 2.4. Scene IDs and AOT₅₅₀ used in adjacency-effect correction for the examples shown in Fig. 2.9.

Scene ID	AOT ₅₅₀
a S2A_MSIL1C_20170830T093031_N0205_R136_T35VMD_20170830T093331	0.097
b LC08_L1TP_186019_20150612_20200909_02_T1	0.068
c S2A_MSIL1C_20190613T101031_N0207_R022_T32TQN_20190613T121346	0.071
d S2A_MSIL1C_20210707T155911_N0301_R097_T17SNV_20210707T200456	0.266
e LC08_L1TP_224077_20160405_20200907_02_T1	0.124

2.4 Discussion

2.4.1 Improvement across AC processors

Improvements in derived ρ_w varied across AC processors, reflecting their distinct algorithms and sensitivities to the AE. Here, we interpret the improvements for each AC processor individually, without attempting to compare results across processors, as each was developed for distinct applications. For ACOLITE, there was a notable improvement in the red-edge and NIR wavelengths (Table 2.3). ACOLITE does not assume a specific spectral shape for water; instead, it simply subtracts atmospheric contributions from TOA reflectance (Vanhellemont and Ruddick, 2018). Consequently, a lowered NIR TOA reflectance from AE correction leads to a reduced ρ_w in the NIR bands (Fig. 2.9). Less improvement was seen in the visible bands, which were already relatively well-retrieved; this was likely because ACOLITE's Dark Spectrum Fitting technique tends to select visible bands, where the AE is less significant, for AOT estimation.

In contrast, POLYMER showed improvement across the entire spectrum (Fig. 2.6 and Fig. 2.9), likely due to its polynomial fitting approach. POLYMER was designed for coastal and open ocean environments where the AE is less significant (Steinmetz et al., 2011). Although POLYMER does not restrain the water reflectance in its output spectra, the NIR contribution from the AE is likely erroneously attributed to either the aerosol-and-glint model or particle backscattering in the water reflectance model during the spectral optimization process. This misattribution could lead to errors that propagate to other wavelengths through the polynomial fitting process; reducing the AE and such misattribution could therefore enhance the optimization process in POLYMER and improve its performance.

For l2gen, a pronounced improvement was observed in the visible range. While the AE correction generally led to greater changes in the NIR range for TOA reflectance, the retrieved ρ_w with AE correction was more notably improved in the visible range (Fig. 2.9), likely from enhanced characterization of aerosols from NIR bands and subsequent extrapolation towards visible wavelengths (Bulgarelli et al., 2017). This improvement was also reflected by the average 18 % less negative retrievals across all bands (Fig. 2.7). This finding is similar to those of Wang and Jiang (2018), who addressed absorbing aerosols by mitigating the negative reflectances retrieved by l2gen. Despite their different mechanisms, both the AE and absorbing aerosols can lead to negative ρ_w retrieved by l2gen, suggesting potential benefits from investigating and integrating their correction methods.

The use of the turbid water correction option in l2gen (Bailey et al., 2010) was not enabled in this exercise with matchups from diverse environments. This option, which estimates non-negligible R_{rs} in NIR bands based on Chl-a concentration, is not activated by default and requires extra settings that may not be familiar to general users. The turbid water correction can potentially compensate for the AE in the NIR bands: overestimates of NIR reflectance can compensate for the AE, when the two have similar values, balancing the retrieved values to the correct level (Bulgarelli et al., 2018). The combined use of such option and AE correction should be investigated further.

2.4.2 Benchmark with another method

Comparing the described AE correction approach with others is challenging due to the lack of open-source software that corrects for the AE at the TOA level, a step necessary for any processing to be followed by AC processors. Alternatively, the Vermote et al. (1997a) approach corrects for the AE at the surface level following atmospheric correction. This approach is the only publicly available AE correction method that the authors are aware of, other than T-Mart, that can complement existing AC methods; it was therefore used for comparison.

The Vermote et al. (1997a) approach requires surface reflectance of both land and water pixels to perform AE correction. Consequently, we applied this approach only to ACOLITE output because the other two AC processors do not derive land surface reflectance. Detailed methodology is included in Supplementary material 6. The 78-122 matchups from ACOLITE output without AE correction (Section 2.2.3.1) were treated with this AE correction. The impact of the Vermote et al. (1997a) correction was significant in the red edge and NIR bands and minimal in the visible range; on average, there was a 16.4 % reduction in RMSE, a 6.3 % reduction in β , and an 18.0 % reduction in ε (Supplementary material 6). In comparison, the T-Mart approach achieved greater improvement across all three metrics and all bands except ε at 865 nm. The greater improvement is likely due to more accurately characterized PSF and fewer assumptions about surface reflectances. The code to perform AE correction following the Vermote et al. (1997a) approach is also made publicly available, with details in Supplementary material 6. It should be noted that since that approach does not require the characterization of the PSF through Monte Carlo simulations, the code performs AE correction within seconds and could be considered a faster but less accurate alternative to T-Mart for applications that rely on NIR bands.

2.4.3 Variability of correction results with distance

The improvements in RMSE at 200 m distance-to-shore intervals (i.e., 0-200 m, 200-400 m, etc.) up to 5 km are shown in Fig. 2.10, and those for β and ε are presented in Supplementary material 5 for brevity, as they share a similar trend.

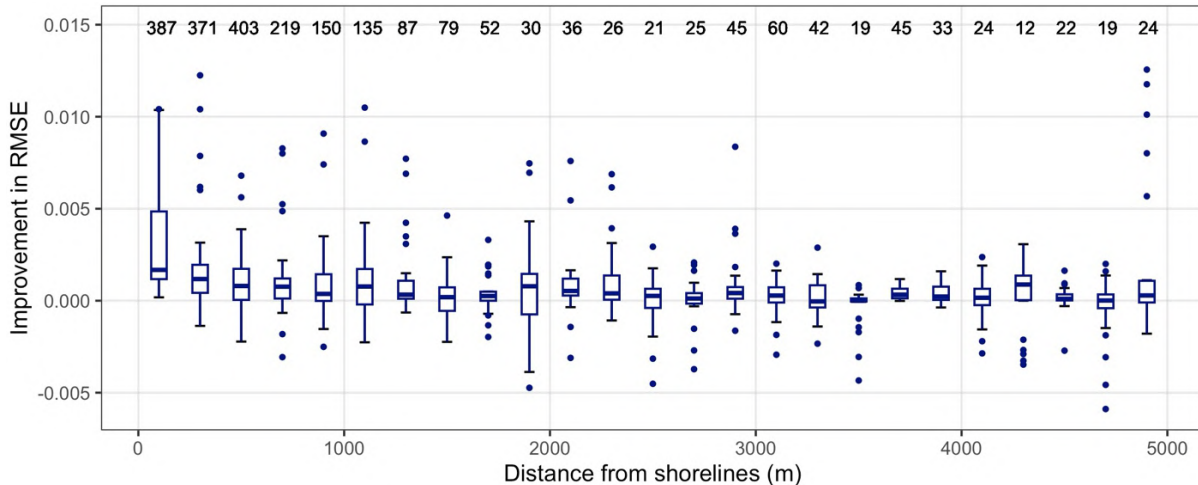


Fig. 2.10. Improvement in RMSE following AE correction for matchups at 200 m distance intervals from shore. The numbers at the top represent the combined sample size from three AC processors for both OLI and MSI products. Each box plot aggregates values for each band ($n=26$) from the three AC processors, weighted by the number of matchups. Positive and negative values indicate reduced and increased RMSE, respectively.

As expected, the most significant improvement in performance metrics was observed in the 0–200 m range where the AE is strongest; and the improvement decreases with distance, roughly centering at zero at a distance of 3000 m from shorelines (Fig. 2.10 and Fig. S5.4). Each AC processor experiences similar improvements across the bands for matchups in the 200–1000 m range as those in the 0–200 m range, although with a lower magnitude. The sample size decreases with distance; intervals beyond the 1200 m range each has a sample size smaller than 100, requiring cautious interpretation of the results.

The 3000 m estimate is shorter than the 36-kilometer range where the AE can be detected by ocean color sensors, modeled and reported by Bulgarelli and Zibordi (2018). Our finding is limited by noise from small sample sizes and instrument inaccuracies. More field data collection, supported by modeling, is likely needed to determine a more accurate distance to shore beyond which AE correction is no longer beneficial.

2.4.4 Implications

Accurate retrieval of water-leaving reflectance is fundamental in optical aquatic remote sensing and is crucial for achieving high accuracy in derived products in freshwater and coastal environments (Pahlevan et al., 2021). In this context, algorithms that utilize red-edge-to-NIR bands for estimating aquatic products, such as TSS (Balasubramanian et al., 2020; Nechad et al., 2010) and Chl-a (Gilerson et al., 2010; Gons, 2005; Moses et al., 2012), can significantly benefit from incorporating the described AE correction when used with ACOLITE, since retrieval of ρ_w in these bands has shown substantial improvements in the matchup exercise (Fig. 2.6 and Table 2.3).

Considering the complexities in measuring *in situ* reflectance in NIR bands (Groetsch et al., 2017; Ruddick et al., 2019), downstream products improved through AE correction in visible wavelengths could also be crucial to operational monitoring. For instance, improved red-band

retrieval in Pléiades products has enhanced water turbidity mapping (Vanhellemont and Ruddick, 2018), better retrieval in the coastal blue and blue bands of Landsat 8 OLI products has increased the accuracy of satellite-derived bathymetry (Ilori and Knudby, 2020), enhanced retrieval of visible wavelengths, especially in the blue spectrum, has improved Chl-a and diffuse attenuation coefficient at 490 nm in VIIRS products (Wang and Jiang, 2018), and accurate spectra of water-leaving reflectance are needed for retrieving seafloor reflectance and identifying habitat types (Hedley et al., 2018; Knudby and Nordlund, 2011; Wilson et al., 2020).

At short distances from coastlines, both *in situ* and satellite-derived reflectances may contain contributions from the water bottom of shallow areas. In addition, satellite-derived reflectance may include sub-pixel contamination of non-water objects. Depending on the processing setting and non-water-masking criteria (Section 2.2.1.2), the AE correction process could include shallow-water and mixed pixels in the output, corrected for the AE assuming Lambertian properties for all contributions (water column, water bottom, and non-water objects). ACOLITE and POLYMER use tiled processing, which utilizes neighbouring pixels to estimate atmospheric contributions, enabling them to retrieve the reflectance of these pixels. Bottom contribution could lead to failure of bio-optical algorithms designed for deep waters (Richardson et al., 2024); however, shallow-water pixels, especially following AE correction, can be used as input for satellite-derived bathymetry, bottom habitat mapping, and bio-optical algorithms tailored for shallow waters, such as the Hyperspectral Optimization Processing Exemplar model (Lee et al., 1998, 1999).

The T-Mart code as an AE correction tool offers several advantages over existing tools: 1) it characterizes multiple scattering using full 3D Monte-Carlo simulations; 2) it is versatile, making no assumptions about the spectral shape of the water, whether it is optically deep or shallow and ranging from clear to moderately turbid; 3) it is open-source with a publicly shared methodology; 4) it was designed for the new generation of decameter-resolution sensors, including Sentinel-2 MSI and Landsat 8/9 OLI, capable of monitoring small inland waterbodies where the AE is most prominent; 5) as a physics-based and sensor-generic tool, it does not require specific band combinations; and 6) it takes into account sensor characteristics and observation environments, performs AE correction at the TOA level, can be followed by any AC processor, and has been validated against *in situ* data collected from diverse environments.

2.4.5 Outlook

The current code assumes flat and Lambertian land-and-water surfaces and a vertically stratified but horizontally homogeneous atmosphere; these assumptions justify the use of a uniform PSF across a satellite scene. Testing or removing such assumptions is challenging: calculating a PSF for each pixel individually and performing spatially variant convolution across the scene is currently computationally impractical with a personal computer. Additionally, the resolution of the ancillary MERRA2 data, which is 0.5° latitude by 0.625° longitude, restricts the potential to study the impact of the heterogeneity of atmospheric gasses and aerosols. Future work could consider topographic effects, the bidirectional reflectance distribution functions of land and water, and the spatial heterogeneity of atmospheric molecules and aerosols within a scene, given improved ancillary and validation data sources and greater computational power.

The scale height for aerosol particles in T-Mart is 2 km, following the 6S model (Vermote et al., 2006); while the code supports different vertical distributions of aerosols, such input data is rare (Watson-Parris et al., 2019). Improved characterization of aerosols from space-borne lidar sensors and the two polarimeters on PACE (Jamet et al., 2019), as well as synchronous polarized multispectral measurements (Xu et al., 2022), could therefore further improve the performance of the AE correction tool.

The magnitude and extent of the AE heavily depend on AOT, which is derived from the MERRA2 dataset in the provided tool. A sensitivity analysis was conducted to examine the impact of varying AOT values from the MERRA2 dataset on the correction results (Supplementary material 7). A range of AOT offset values within the RMSE of MERRA2 AOT_{550} (0.126) was used. The analysis included the ten scenes with the highest numbers of matchups within 200 m, totaling 76 *in situ* measurements. Results from the non-zero AOT_{550} offsets were compared with those using the default MERRA2 values. The findings indicate that POLYMER benefits from slight AOT overestimates in AE correction, while ACOLITE benefits from a wide range of AOT overestimates potentially at the cost of deviating spectral shapes. l2gen works best with default AOT values, although with occasional improvements from overestimated AOT values. Overall, the use of ancillary AOT values does not appear to be a significant concern for the dataset used in this study.

The described algorithm is physics-based, and it inherently considers the spectral difference between the target and scattering sources; however, improvement from AE correction is likely to vary across different target-and-scattering-source combinations for each AC processor. For example, POLYMER demonstrated resistance to the AE from snow and ice, as the spectrally smooth impact of AE can be mitigated during the polynomial fitting process (Steinmetz and Ramon, 2018). The performance of AE correction for various land-cover, water-type, and AC-processor combinations can be further assessed following approaches in König et al. (2019), Pan et al. (2022), and Bulgarelli and Zibordi (2018).

Future work should address the AE originating from clouds, especially considering the challenges in estimating their altitude. The interaction between the relative altitude of clouds and aerosols in the atmospheric column makes this a fundamentally three-dimensional problem. While T-Mart supports modeling surfaces with non-flat topography, it assumes parallel atmospheric layers. The 3D version of the MYSTIC solver in libRadtran (Mayer, 2009), which allows for 3D optical properties of clouds, may provide the necessary capabilities for simulating such interactions.

Although a sample size of 212 has provided encouraging evidence of the tool's performance, expanding the size of nearshore matchup datasets with initiatives like the Remote sensing Adjacency Correction project (RAdCor, 2024) will enhance the assessment of tool performance. It is also essential to evaluate how these advancements affect downstream products, such as satellite-derived concentrations of Chl-a and TSS, and how they contribute to meeting monitoring and operational requirements.

The emergence of high-resolution imagery has led to development of applications for smaller waterbodies such as lakes, rivers, and estuaries (Pahlevan et al., 2021) where the AE is

significant, highlighting the importance of a sensor-generic AE correction tool. There have been successes in sub-meter AE correction for panchromatic bands (Wang et al., 2021a, 2021b). T-Mart focuses on the narrower-band sensors and supports data from Landsat 9 OLI-2 and PRISMA; its performance for these sensors has not yet been assessed due to the limited number of matchups with publicly available *in situ* measurements. Future development will prioritize high-resolution sensors such as WorldView, PlanetScope, and SkySat. Although the performance of T-Mart AE correction has only been assessed on Landsat 8 OLI and Sentinel-2 MSI products, similar performance is expected for imagery from other sensors as the algorithm does not make assumptions about sensor characteristics. It should be noted that since a large 36×36 km PSF is used to characterize the source of diffuse radiance in the AE correction, the correction results for narrow-swath imagery (i.e., 30 km swath width for PRISMA and EnMAP products) will inevitably be compromised due to missing information from neighbouring areas. In such cases, filling the reflectance outside the scenes with seasonal averages or modeled products may improve the performance of AE correction.

2.5 Conclusion

We introduced an approximate solution to a closed-form expression that corrects for the AE at the TOA level (Eq. (2.1)). This solution is implemented in a Python tool that computes the atmospheric PSF, convolves the observed reflectance, and calculates the difference between the convolved and observed reflectance. Lastly, the tool removes the product of the difference and a scaling factor from the TOA reflectance and corrects for variations in ground-level irradiance due to surface heterogeneity. The output is adjacency-effect-free TOA reflectance that can be further processed by any AC processor. Following the described AE correction, we demonstrated substantial improvements in the retrieval of water-leaving reflectance in the context of aquatic remote sensing of coastal and freshwater environments. For matchups within 200 m of shorelines ($n = 212$), applying AE correction resulted in an average 16.7 % reduction in RMSE, 32.4 % in β , and 36.8 % in ε across all MSI and OLI bands processed by three state-of-the-art AC processors (Table 2.3). 75 of the 78 performance metric values spanning all processors and bands improved as a result of AE correction. The few negative changes, all observed with POLYMER, were likely due to noise resulting from a relatively small matchup sample size and the processor's approach of optimizing spectral fitting between modeled and at-sensor reflectances. The extent of these improvements varied across processors. ACOLITE showed more significant enhancements in the NIR wavelengths, while l2gen exhibited greater improvements in the visible range and less change in longer wavelengths. For POLYMER, the improvements were evenly distributed across the visible-NIR spectrum. The improved retrieval of water-leaving reflectance from AE correction is expected to enhance the quality of derived downstream products for coastal and freshwater environments. It is therefore recommended that the provided AE correction tool be implemented when conducting aquatic remote sensing studies in such environments.

Installation and Use of the Tool

T-Mart is written in Python. The code, installation instructions, and a quick-start menu are available from <https://github.com/yulunwu8/tmart>. Detailed processing options can be found at <https://tmart-rtm.github.io>. The tool takes approximately 20 minutes to process a Landsat 8/9

scene and 30 minutes for a Sentinel-2 scene on an eight-core personal computer. Ancillary atmospheric and aerosol data are automatically downloaded in the AE correction process given NASA EarthData Credentials.

Declaration of Competing Interest

The authors declare that they have no known competing financial interests or personal relationships that could have appeared to influence the work reported in this paper.

Author Contributions

Yulun Wu: Conceptualization, Methodology, Software, Data curation, Formal analysis, Validation, Writing – original draft, Writing – review & editing. **Anders Knudby:** Conceptualization, Supervision, Funding acquisition, Writing – review & editing. **Nima Pahlevan:** Data curation, Writing – review & editing. **David Lapen:** Conceptualization, Funding acquisition, Writing – review & editing. **Chuiqing Zeng:** Writing – review & editing.

Acknowledgments

This project was funded by the Canadian Space Agency [22AO2-LIQU] and Agriculture and Agri-Food Canada [J-001839-Emerging Services of Agro-ecosystems; J-002305-Environmental Change Onehealth Observatory (ECO2)]. We thank NASA/USGS and ESA/Copernicus for the acquisition and free distribution of Landsat and Sentinel-2 imagery used in this work. We thank the data providers behind the GLORIA dataset for collecting and sharing of the data. We are thankful to Quinten Vanhellemont and Kevin Ruddick for the development and support of ACOLITE, François Steinmetz, Pierre-Yves Deschamps, Didier Ramon for the development and support of POLYMER, and the NASA Ocean Biology Processing Group and Ocean Biology Distributed Active Archive Center for the development and support of the SeaDAS software and distribution of ancillary meteorological data. Alexandre Castagna, Quinten Vanhellemont, Christopher Ilori, and Christopher Begeman are thanked for their valuable comments and discussions. Four anonymous reviewers are thanked for their constructive feedback which helped improve the manuscript.

2.6 Supplementary materials

Supplementary material 1: Impact of simplifying the calculation of α in AE correction

The impact of excluding $(1 - cc) \cdot U_1$ and $cc \cdot U_2$ in the calculation of α in AE correction (Eq. 18) was evaluated by conducting AE correction in a modeling environment. We used ACOLITE-output surface reflectance of two Sentinel-2 scenes as surface reflectance. The first scene was in Japan, featuring a complex landscape and high AOT; the second scene, a relatively smooth coastal area with medium-low AOT, was in New Zealand (Table S1.1). Aerosol type, AOT, and ozone and water vapor concentrations for the scenes were extracted from the GMAO MERRA2 meteorological and aerosol datasets following Section 2.1.2 and Supplementary material 2. These were used to construct the optical properties of the atmosphere using 6S through the Py6S Python interface (Wilson, 2013). Direct and diffuse transmittances, atmospheric spherical albedo, the PSF, and the atmospheric intrinsic reflectance were then calculated in T-Mart (Wu et al., 2023). ρ_s^{env} was calculated following Eq. (4). Lastly, the TOA reflectance of heterogeneous scenes was simulated using Eq. (3) with parameters described above as inputs. In summary, TOA reflectance in the presence of the AE was modeled in a ‘known’ atmosphere-surface system.

Table S1.1. Sentinel-2 scenes and AOT₅₅₀ used in the simulation.

Location	Scene ID	AOT ₅₅₀
Japan	S2A_MSIL1C_20190308T015651_N0207_R060_T52SFA_20190308T044306	0.17
New Zealand	S2B_MSIL1C_20191102T221609_N0208_R129_T60GTU_20191102T232453	0.09

AE correction was performed following the procedure described in Section 2.1.2. Two α values were used and compared: α with full terms in Eq. (18) and simplified α in Eq. (19), respectively. The differences in TOA reflectance of water pixels between correction results using different α values were also calculated (Fig. S1.1). Water pixels were defined as those with a surface reflectance at 865 nm < 0.02 to include shallow water pixels.

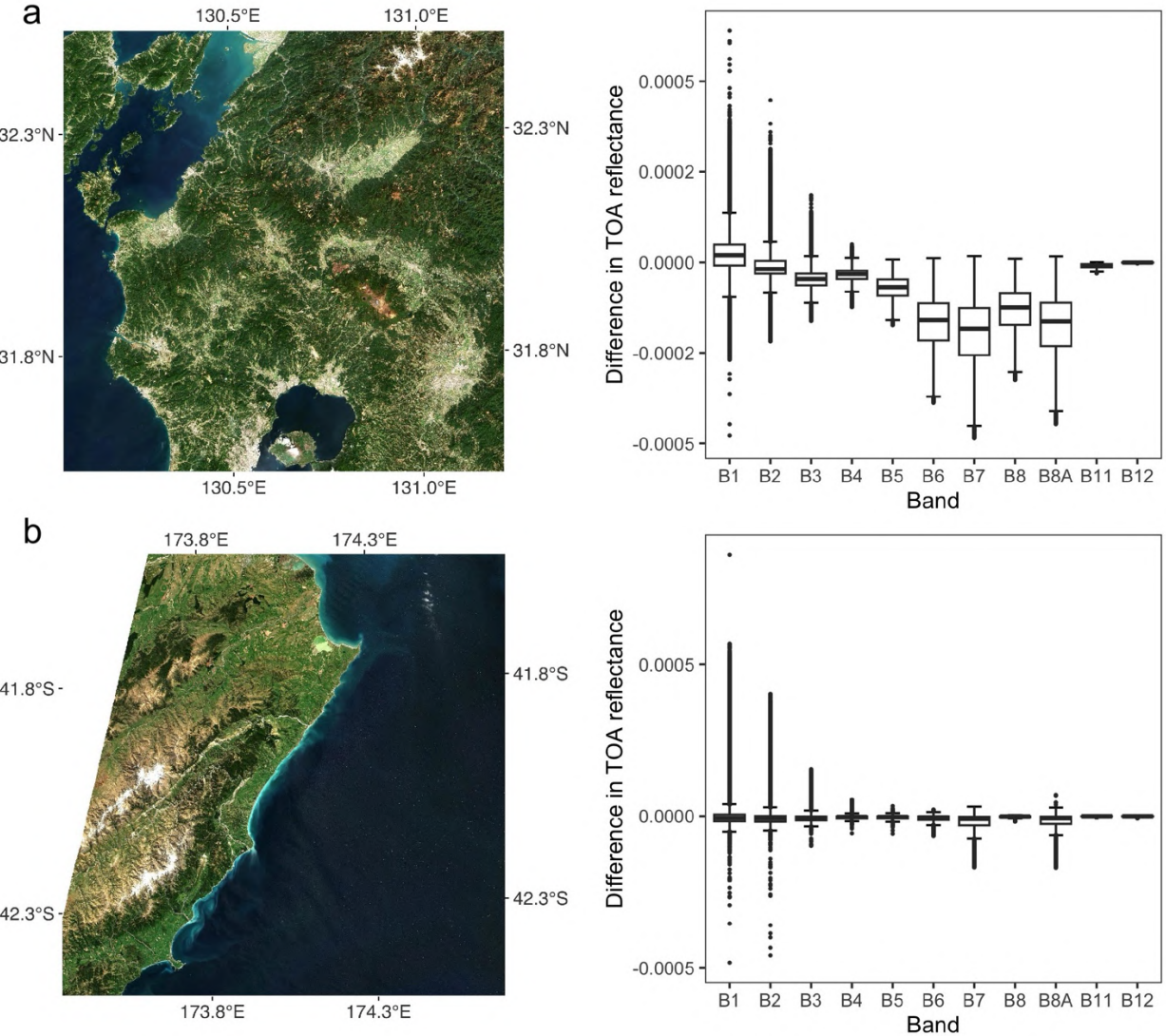


Fig. S1.1. Sentinel-2 scenes illustrating the impact of simplifying α on the output TOA reflectance with AE correction in (a) southeastern Japan, and (b) eastern New Zealand, for all water pixels in the scenes. Positive and negative values indicate overestimated and underestimated TOA reflectance, respectively, compared to AE correction using full-term α .

Compared to AE correction using the full-term α , excluding $(1 - cc) \cdot U_1$ and $cc \cdot U_2$ can result in a slight underestimation of AE-free TOA reflectance with a median bias up to 0.00017 at the TOA level in red-edge and NIR bands (Fig. S1.1a). This bias is significantly smaller than the noise level of Sentinel-2, which ranges from approximately 0.002 in visible and NIR bands to 0.0007 in SWIR bands for the two scenes. The noise levels were calculated by

$$\frac{L_{\text{ref}} \cdot \pi / E_d}{\text{SNR}}$$

where E_d is the solar irradiance at TOA level, calculated using 6S with inputs of the solar angle and observation date, and SNR and L_{ref} are the signal-to-noise ratio and reference radiance for each band, respectively, as specified in the Sentinel-2 User Handbook (ESA, 2015).

Landsat 8 OLI has a higher SNR than Sentinel-2 MSI for most of its bands due to the lower spatial resolution (Pahlevan et al., 2017). Given that the amount of AE correction decreases with a larger pixel size, the impact of excluding $(1 - cc) \cdot U_1$ and $cc \cdot U_2$ in the calculation of α for AE correction of OLI products will still be lower than the sensor's noise level, but can potentially reach the noise level in the NIR band (band 5) in case of highly complex topography and extreme AOT conditions (e.g., $AOT_{550} > 0.3$).

References:

- ESA. (2015). *Sentinel-2 User Handbook*.
https://sentinel.esa.int/documents/247904/685211/Sentinel-2_User_Handbook
- Pahlevan, N., Sarkar, S., Franz, B. A., Balasubramanian, S. V., & He, J. (2017). Sentinel-2 MultiSpectral Instrument (MSI) data processing for aquatic science applications: Demonstrations and validations. *Remote Sensing of Environment*, 201, 47–56.
<https://doi.org/10.1016/j.rse.2017.08.033>
- Wilson, R. T. (2013). Py6S: A Python interface to the 6S radiative transfer model. *Computers & Geosciences*, 51, 166–171. <https://doi.org/10.1016/j.cageo.2012.08.002>
- Wu, Y., Knudby, A., & Lapen, D. (2023). Topography-adjusted Monte Carlo simulation of the adjacency effect in remote sensing of coastal and inland waters. *Journal of Quantitative Spectroscopy and Radiative Transfer*, 303, 108589.
<https://doi.org/10.1016/j.jqsrt.2023.108589>

Supplementary material 2: Interpolation of aerosol information

MERRA2 provides hourly aerosol information, including AOT₅₅₀, Angstrom exponent, and single-scattering albedo. ACOLITE, by default, uses continental and maritime aerosol models from 6S, automatically selecting the one with the best fit using the dark-spectrum fitting technique across the reflectance spectrum (Vanhellemont and Ruddick, 2018). To ensure a smoother transition of aerosol composition from land to water, we chose to linearly interpolate the aerosol composition between the two aerosol models from 6S using MERRA2's Angstrom exponent and single-scattering albedo.

In 6S, the continental and maritime aerosol models have Angstrom exponents of 1.132 and 0.265, and single-scattering albedos of 0.893 and 0.989, respectively (Vermote et al., 2006). The two parameters are retrieved for the scenes to be processed, and used to linearly interpolate the fraction of the two aerosol types in the mixture (e.g., a single-scattering albedo of 0.941 would lead to a fraction of 50 % continental and 50 % maritime aerosols). The fractions derived from these two parameters are averaged and then linearly interpolated in time. The calculation process can be found in the script `anci_get_AER.py`
[\(https://github.com/yulunwu8/tmart/blob/main/tmart/AEC/anci_get_AER.py\)](https://github.com/yulunwu8/tmart/blob/main/tmart/AEC/anci_get_AER.py).

The composition of mixed continental and maritime aerosols is linearly attributed to the four basic aerosol components in 6S: all aerosol models in 6S are constructed using dust-like, oceanic, water-soluble, and soot components (Vermote et al., 2006). Continental aerosols consist of 70 % dust-like, 29 % water-soluble, and 1 % soot components by volume; maritime aerosols consist of 5 % water-soluble and 95 % soot components by volume. The fraction of each aerosol type is used to calculate the overall fractions of the four components or the overall aerosol composition, which are subsequently used to calculate aerosol optical properties. The calculation of aerosol optical properties is detailed in the script `Atmosphere.py`
[\(https://github.com/yulunwu8/tmart/blob/main/tmart/Atmosphere.py\)](https://github.com/yulunwu8/tmart/blob/main/tmart/Atmosphere.py).

References:

- Vanhellemont, Q., & Ruddick, K. (2018). Atmospheric correction of metre-scale optical satellite data for inland and coastal water applications. *Remote Sensing of Environment*, 216, 586–597. <https://doi.org/10.1016/j.rse.2018.07.015>
- Vermote, E. F., Tanré, D., Deuze, J. L., Herman, M., & Morcrette, J.-J. (2006). Second Simulation of a Satellite Signal in the Solar Spectrum—Vector (6SV). *6S User Guide Version 3*. <https://ltdri.org/6spage.html>

Supplementary material 3: Performance metrics**Table S3.1.** Performance metrics with and without adjacency-effect correction for Sentinel-2 imagery-derived water-leaving reflectance, grouped by atmospheric correction processor.**a) ACOLITE**

	Without				With			
	RMSE	β	ε	n	RMSE	β	ε	n
Band 1	0.011	-6.7	38.8	51	0.012	18.2	46.5	53
Band 2	0.011	-23.9	40.0	51	0.011	2.5	28.4	53
Band 3	0.016	-13.6	24.2	51	0.015	-5.3	18.9	53
Band 4	0.017	-42.1	43.8	51	0.015	-24.6	31.8	53
Band 5	0.015	-16.3	35.4	51	0.014	-16.3	32.5	53
Band 6	0.010	108.2	113.1	51	0.006	0.9	35.5	53
Band 7	0.012	160.6	160.6	51	0.006	39.2	50.4	53
Band 8	0.013	196.5	196.5	19	0.004	15.8	68.7	21
Band 8A	0.013	211.1	211.1	19	0.004	17.1	69.9	21

b) POLYMER

	Without				With			
	RMSE	β	ε	n	RMSE	β	ε	n
Band 1	0.031	76.8	96.0	86	0.030	26.4	67.7	86
Band 2	0.021	17.3	53.1	86	0.020	16.5	39.4	86
Band 3	0.026	-16.1	45.1	86	0.024	-9.0	29.5	86
Band 4	0.022	-165.4	165.4	86	0.018	-67.1	71.4	86
Band 5	0.022	-95.3	95.3	86	0.019	-54.9	55.1	86
Band 6	0.008	1.9	22.8	86	0.007	-2.6	20.2	86
Band 7	0.007	26.7	41.0	86	0.006	17.4	30.8	86
Band 8	0.011	-47.3	47.3	49	0.010	-37.0	37.0	49
Band 8A	0.006	-81.5	81.5	49	0.006	-41.1	41.1	49

c) l2gen

	Without				With			
	RMSE	β	ε	n	RMSE	β	ε	n
Band 1	0.043	-111.6	111.6	26	0.024	-22.6	22.6	29
Band 2	0.044	-125.7	125.7	29	0.025	-22.9	22.9	30
Band 3	0.043	-58.5	58.5	32	0.031	-16.4	16.4	32
Band 4	0.034	-53.0	53.0	32	0.024	-19.2	19.3	32
Band 5	0.031	-42.3	42.3	33	0.023	-18.3	18.3	33
Band 6	0.025	-29.8	29.8	42	0.024	-18.4	18.4	42
Band 7	0.020	-20.4	20.4	44	0.019	-15.8	15.8	44
Band 8	0.024	-38.2	38.2	27	0.024	-38.2	38.2	27

Table S3.2. Same as Table S1, but for Landsat 8 matchups.**a) ACOLITE**

	Without				With			
	RMSE	β	ε	n	RMSE	β	ε	n
Band 1	0.021	-42.2	49.7	71	0.018	-23.8	32.9	72
Band 2	0.021	-32.6	33.6	71	0.019	-16.8	25.5	72
Band 3	0.030	-15.7	18.9	71	0.028	-11.6	15.0	72
Band 4	0.024	-14.9	20.2	71	0.023	-11.1	19.4	72
Band 5	0.006	12.6	16.5	59	0.006	-16.5	20.0	60

b) POLYMER

	Without				With			
	RMSE	β	ε	n	RMSE	β	ε	n
Band 1	0.042	-64.5	69.5	91	0.029	-58.5	62.7	91
Band 2	0.043	-33.9	40.8	91	0.032	-31.5	33.5	91
Band 3	0.047	-29.2	30.7	91	0.041	-25.4	25.8	91
Band 4	0.041	-41.1	46.8	91	0.038	-28.7	33.7	91
Band 5	0.031	-5.4	20.0	71	0.037	-2.9	20.5	71

c) l2gen

	Without				With			
	RMSE	β	ε	n	RMSE	β	ε	n
Band 1	0.034	-37.0	42.2	62	0.027	-13.0	18.9	55
Band 2	0.034	-38.2	42.5	62	0.027	-14.8	21.0	55
Band 3	0.040	-32.1	39.5	62	0.035	-14.7	22.1	55
Band 4	0.032	-36.2	44.0	62	0.027	-13.6	24.2	55

Supplementary material 4: Negative reflectance values

Table S4.1. Number and percentage of negative reflectance values with and without adjacency-effect correction for Sentinel-2 imagery-derived water-leaving reflectance, grouped by atmospheric correction processor.

a) ACOLITE

	Without			With		
	n (neg.)	% (neg.)	n	n (neg.)	% (neg.)	n
Band 1	2	3.9	51	1	1.9	53
Band 2	2	3.9	51	0	0	53
Band 3	0	0	51	0	0	53
Band 4	1	2.0	51	0	0	53
Band 5	0	0	51	1	1.9	53
Band 6	0	0	51	2	3.8	53
Band 7	0	0	51	1	1.9	53
Band 8	0	0	19	3	14.3	21
Band 8A	0	0	19	4	19.0	21

b) POLYMER

	Without			With		
	n (neg.)	% (neg.)	n	n (neg.)	% (neg.)	n
Band 1	0	0	86	0	0	86
Band 2	0	0	86	0	0	86
Band 3	0	0	86	0	0	86
Band 4	3	3.5	86	0	0	86
Band 5	40	46.5	86	31	36.0	86
Band 6	1	1.2	86	5	5.8	86
Band 7	0	0	86	1	1.2	86
Band 8	45	91.8	49	37	75.5	49
Band 8A	46	93.9	49	39	79.6	49

c) l2gen

	Without			With		
	n (neg.)	% (neg.)	n	n (neg.)	% (neg.)	n
Band 1	21	80.8	26	17	58.6	29
Band 2	20	69.0	29	10	33.3	30
Band 3	14	43.8	32	6	18.8	32
Band 4	18	56.3	32	8	25.0	32
Band 5	19	57.6	33	9	27.3	33
Band 6	36	85.7	42	25	59.5	42
Band 7	30	68.2	44	22	50.0	44
Band 8	26	96.3	27	24	88.9	27

Table S4.2. Same as Table S1, but for Landsat 8 matchups.**a) ACOLITE**

	Without		With			
	n (neg.)	% (neg.)	n	n (neg.)	% (neg.)	n
Band 1	0	0	71	0	0	72
Band 2	0	0	71	0	0	72
Band 3	0	0	71	0	0	72
Band 4	0	0	71	0	0	72
Band 5	0	0	59	5	8.3	60

b) POLYMER

	Without		With			
	n (neg.)	% (neg.)	n	n (neg.)	% (neg.)	n
Band 1	0	0	91	0	0	91
Band 2	0	0	91	0	0	91
Band 3	0	0	91	0	0	91
Band 4	0	0	91	0	0	91
Band 5	0	0	71	0	0	71

c) l2gen

	Without		With			
	n (neg.)	% (neg.)	n	n (neg.)	% (neg.)	n
Band 1	16	25.8	62	3	5.5	55
Band 2	6	9.7	62	3	5.5	55
Band 3	3	4.8	62	2	3.6	55
Band 4	5	8.1	62	2	3.6	55

Supplementary material 5: Analysis of matchups within 5 km of shores

The sample size of matchups for *in situ* measurements from the GLORIA dataset decreases with increasing distance from shorelines (Fig. S5.1). For both MSI and OLI products, the number of matchups falls below 20 in every 200 m interval beyond 5 km. Consequently, we focused our analysis on matchups within 5 km of shorelines.

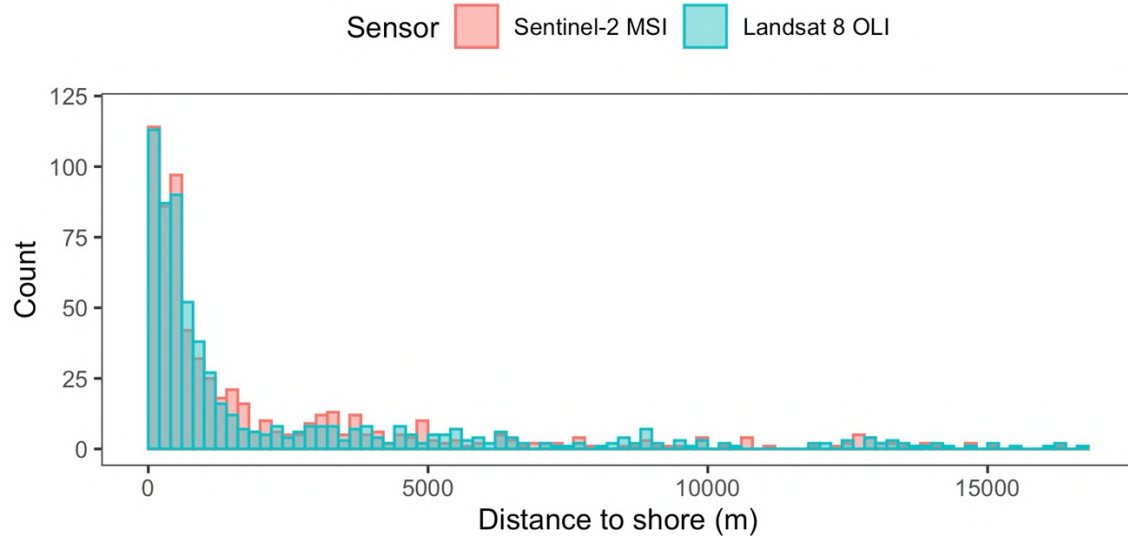


Fig. S5.1. Number of *in situ* measurements coinciding with Sentinel-2 and Landsat 8 overpasses as a function of distance from shorelines.

Matchups up to 5 km from shorelines were analyzed following Section 2.3, at every 200 m interval. A total of 981 *in situ* R_{rs} measurements were identified within a six-hour time window of 129 Sentinel-2 and 130 Landsat 8 overpasses (Fig. S5.2). The retrieved ancillary AOT values shared a similar distribution to those of the 200 m distance-to-shore dataset (Fig. S5.3 and Fig. 8).

Chapter 2: Adjacency effect correction



Fig. S5.2. Geographical distribution of 981 matchups from the GLORIA dataset within 5 km of shorelines and with Sentinel-2 or Landsat 8 overpasses.

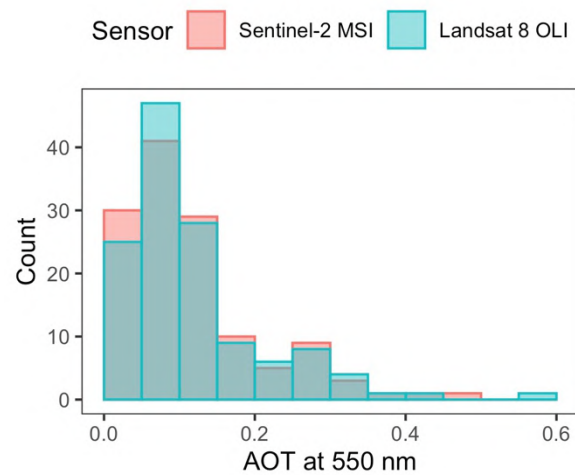


Fig. S5.3. Distribution of retrieved aerosol optical thickness at 550 nm. One value was retrieved for each image.

Chapter 2: Adjacency effect correction

For each distance interval and each performance metric, we aggregated the improvement from AE correction across all bands and AC processors for brevity (Fig. S5.4). The results are discussed in Section 4.3.

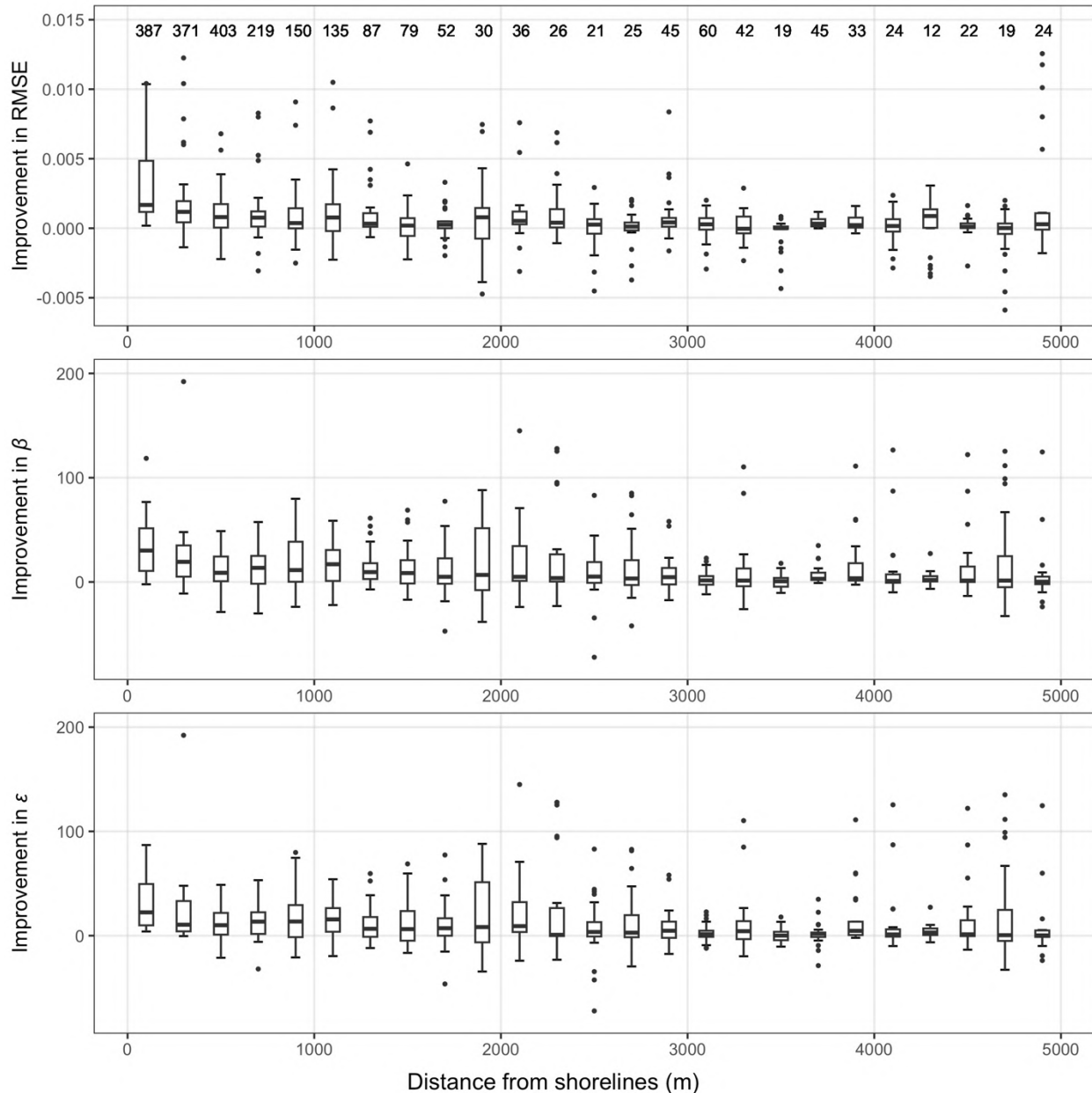


Fig. S5.4. Improvement in performance metrics following AE correction for matchups at 200 m distance intervals from shorelines. The numbers at the top represent the combined sample size from three AC processors for both OLI and MSI products. Each box plot aggregates values for each band ($n=26$) from the three AC processors, weighted by the number of matchups. Positive and negative values indicate improved and reduced performance, respectively.

Supplementary material 6: Comparison with Vermote et al. 1997

The correction results of T-Mart were compared with those following the Vermote et al. (1997) approach. The Vermote et al. (1997) approach corrects for the AE using the following formula:

$$\rho_s = \frac{\rho_s^u \cdot T_{RA}(\mu_v) - \langle \rho_s \rangle \cdot t_d(\mu_v)}{\exp(-\tau/\mu_v)} \quad (26)$$

where ρ_s is the pixel reflectance at the surface level, ρ_s^u is the reflectance of an infinite Lambertian target, approximated by performing atmospheric correction for each pixel individually under the assumption that each pixel is Lambertian and surrounded by identical pixels. $T_{RA}(\mu_v)$ and $t_d(\mu_v)$ are the total and diffuse upward transmittances, respectively. μ_v is the cosine of the view zenith angle, τ is the combined aerosol and molecular optical thickness, and $\langle \rho_s \rangle$ is the PSF-weighted average surface reflectance around a pixel. $\langle \rho_s \rangle$ is calculated as,

$$\langle \rho_s \rangle = \sum_{j=-n}^n \sum_{i=-n}^n f(r(i,j)) \cdot \rho(i,j) \quad (27)$$

where $r(i,j)$ represents the distance between pixel (i,j) and the target in km, f is weight of the PSF at the pixel or the fraction of diffuse radiance that comes from the pixel, and $\rho(i,j)$ is the reflectance of the pixel (i,j) , which is unknown in practice and therefore approximated by $\rho_s^u(i,j)$.

Following Vermote et al. (1997), Vermote et al. (2006) updated the approximation of the PSF:

$$F(r) = \frac{t_d^R(\mu_v) \cdot F_R(r) + t_d^A(\mu_v) \cdot F_A(r)}{t_d^R(\mu_v) + t_d^A(\mu_v)} \quad (28)$$

where $F(r)$ is the fraction of diffuse radiation at the sensor that originates from within the radius r (in km), t_d^R and t_d^A are the fractions of the diffuse transmittance respectively for Rayleigh and aerosols, and the functions $F_R(r)$ and $F_A(r)$ are given by:

$$\begin{aligned} F_R(r) &= 1 - 0.930 \exp(-0.08r) - 0.070 \exp(-1.1r) \\ F_A(r) &= 1 - 0.448 \exp(-0.27r) - 0.552 \exp(-2.83r) \end{aligned} \quad (29)$$

where r is distance in km.

Converting $F(r)$ to $f(r)$ is challenging as $F(r)$ is the fraction of diffuse radiation within the radius r , while $f(r)$ is the fraction of diffuse radiation from a specific pixel at distance r from the target. The conversion involves creating layers of circular bands with a width equal to half the sensor's resolution, centered at the target pixel. The weight of each band is calculated by $F(r+w) - F(r)$ where w is the width of the band at various radii r . These weights are then normalized to their respective areas to determine the density of diffuse radiation within each

band. Finally, these densities are interpolated to fill the PSF grid, with the sensor's resolution as the cell size.

Martins et al. (2019) re-arranged Eq. (2.14) as follows,

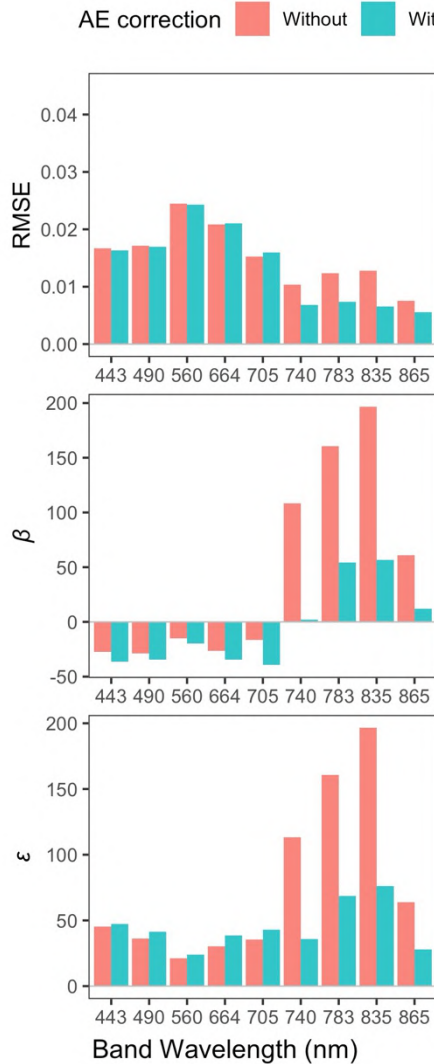
$$\rho_s = \rho_s^u + \frac{t_d(\mu_v)}{\exp(-\tau/\mu_v)} (\rho_s^u - \langle \rho_s \rangle). \quad (30)$$

This rearrangement is conceptually more straightforward and easier to implement, with the term to the right of the plus sign representing the correction amount. This modified equation was therefore used in the processing. Vermote et al. (1997, 2006) did not specify the size of the PSF. Following Martins et al. (2019), we used 1 km × 1km grids. The GMAO MERRA2 Meteorological and Aerosol datasets provided aerosol type, AOT, and ozone and water vapor concentrations, as described in Section 2.1.2 and Supplementary material 2. These inputs were used in 6S to calculate $t_d(\mu_v)$ and $\exp(-\tau/\mu_v)$, via the Py6S interface (Wilson, 2013). The code is available at <https://github.com/yulunwu8/Adjacency-effect-correction-6S>.

Since the Vermote et al. (1997) approach requires surface reflectance data for both land and water, and only ACOLITE, among the three AC processors, provides the necessary data. Consequently, ACOLITE outputs from Section 2.3, without AE correction, were treated with AE correction using the Vermote et al. (1997) approach and compared with the original outputs, followed by the matchup-extraction process in Section 2.3.2. Performance metrics were calculated following Section 2.3.3. Results are presented in Fig. S6 and discussed in Section 4.2.

References:

- Martins, V. S., Kaleita, A., Barbosa, C. C. F., Fassoni-Andrade, A. C., Lobo, F. de L., & Novo, E. M. L. M. (2019). Remote sensing of large reservoir in the drought years: Implications on surface water change and turbidity variability of Sobradinho reservoir (Northeast Brazil). *Remote Sensing Applications: Society and Environment*, 13, 275–288.
<https://doi.org/10.1016/j.rasae.2018.11.006>
- Vermote, E. F., El Saleous, N., Justice, C. O., Kaufman, Y. J., Privette, J. L., Remer, L., Roger, J. C., & Tanré, D. (1997). Atmospheric correction of visible to middle-infrared EOS-MODIS data over land surfaces: Background, operational algorithm and validation. *Journal of Geophysical Research: Atmospheres*, 102(D14), 17131–17141.
<https://doi.org/10.1029/97JD00201>
- Vermote, E. F., Tanré, D., Deuze, J. L., Herman, M., & Morcrette, J.-J. (2006). Second Simulation of a Satellite Signal in the Solar Spectrum—Vector (6SV). *6S User Guide Version 3*. <https://ltdri.org/6spage.html>
- Wilson, R. T. (2013). Py6S: A Python interface to the 6S radiative transfer model. *Computers & Geosciences*, 51, 166–171. <https://doi.org/10.1016/j.cageo.2012.08.002>



	RMSE	β	ε
443 nm	1.9	-33.2	-4.3
490 nm	0.8	-18.8	-13.4
560 nm	0.8	-33.5	-13.7
664 nm	-0.7	-32.2	-27.9
705 nm	-4.6	-141.7	-21.6
740 nm	34.0	98.0	68.4
780 nm	40.3	66.2	57.2
833 nm	48.5	71.2	61.3
865 nm	26.2	80.3	56.3

Fig. S6. (left) Performance metrics of ACOLITE outputs with and without AE correction following the Vermote et al. (1997) approach. Bands at 705, 740, 783, and 835 nm are exclusive to Sentinel-2 MSI matchups, and the other bands are shared by Landsat 8 OLI and Sentinel-2 MSI. (right) Percentage reduction of performance metrics with the implementation of AE correction, grouped by atmospheric correction processor. Positive and negative values indicate improved and reduced performance, respectively (Eq. (25)). All values are in units of % change; values greater than 30 % are in bold.

Supplementary material 7: Impact of biases in ancillary AOT values

The accuracy of the AE correction depends heavily on ancillary AOT values. Here, we investigate how potential biases in AOT values affect the results of AE correction.

We selected the ten Landsat 8 and Sentinel-2 scenes with the highest number of matchups within 200 m of shorelines from Section 2.3.1, with a total of 76 *in situ* measurements. Gueymard and Yang (2020) evaluated the global accuracy of the MERRA2 reanalysis AOT product against 15 years of AERONET observations, estimating the RMSE of MERRA2 AOT to be 0.126. We ran the T-Mart AE correction nine times with various AOT₅₅₀ offsets within the RMSE range to investigate if the retrieved reflectance by AC processors, following the AE corrections, could be more accurate than the default values. The AOT₅₅₀ offsets used were 0.126, -0.0945, -0.063, -0.0315, 0, 0.0315, 0.063, 0.0945, and 0.126. For each offset, we compared the change in performance metrics to those with an offset of 0. Results from the OLI and MSI datasets were combined, weighted by the number of matchups, and aggregated by AC processors (Fig. S7.1).

The default values for POLYMER and l2gen outperformed most of the AOT offsets. For most metrics, performance decreased for processor-offset combinations deviating from the default AOT values. However, there were occasional improvements such as an offset of 0.0315 for POLYMER and 0.063 for l2gen.

Surprisingly, overcorrection of the AE leads to consistent improvement in all three performance metrics for ACOLITE, enhancing the overall performance across the visible-NIR spectrum. High AE correction, following a high AOT offset, usually results in low AOT estimates in ACOLITE. This overcorrection seems to mitigate the underestimation of ACOLITE-derived reflectance at visible wavelengths (Fig. 7). Although all three metrics showed improvement, this comes at the potential cost of deviating spectral shapes; at high AOT offsets, the retrieved NIR reflectance by ACOLITE can become underestimated, despite achieving a better fit in the visible range (Fig. S7.2). Therefore, it is recommended to adhere to the default MERRA2 AOT₅₅₀ values for all AC processors.

Chapter 2: Adjacency effect correction

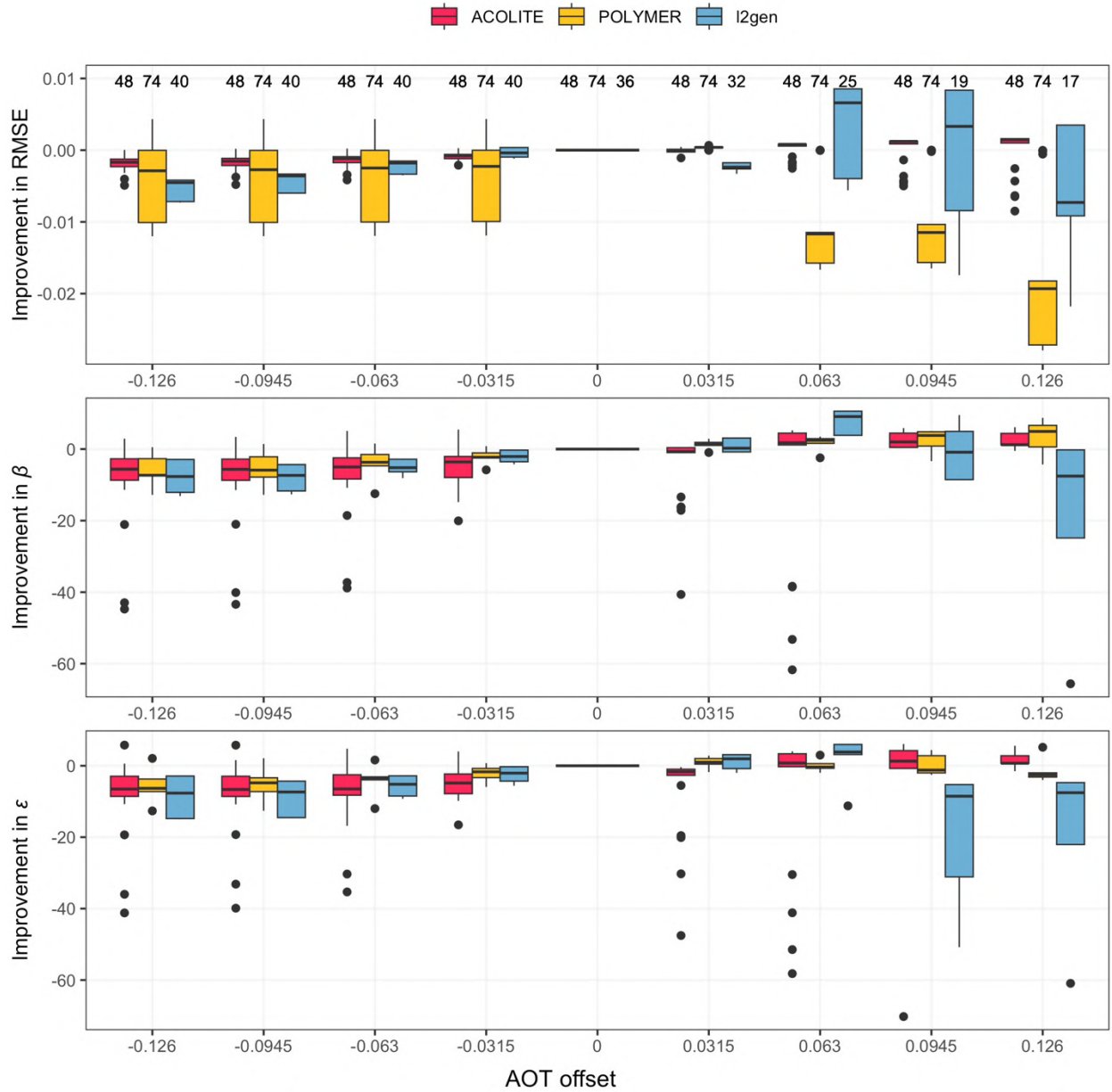


Fig. S7.1. Change in performance metrics of reflectance retrieval with AE correction at various AOT offsets. Each box plot aggregates values for each band ($n=8$ or 9) for each AC processor. Results for OLI and MSI bands were combined, weighted by the number of matchups from each dataset. Numbers at the top indicate the total number of matchups for both datasets. Some outliers, such as β and ϵ for ACOLITE at offsets of 0.0315 and 0.063, represent the unique bands of MSI. These bands have a smaller sample size and were given less weight when plotting the boxes (i.e., median and interquartile range).

Chapter 2: Adjacency effect correction

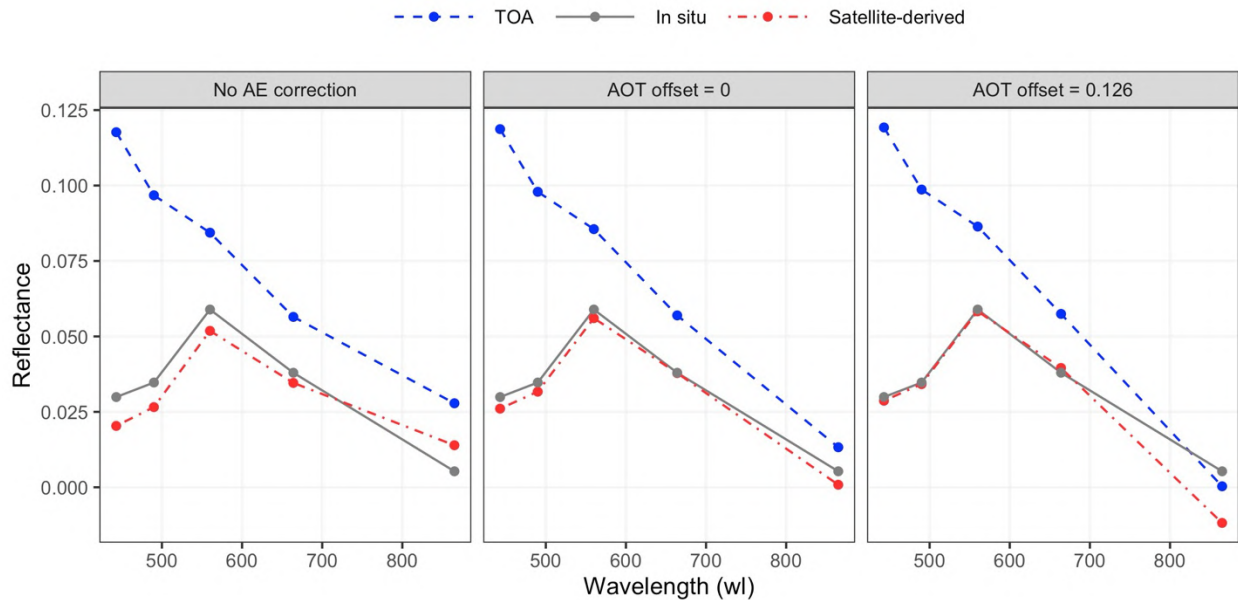


Fig. S7.2. Example ACOLITE outputs with various AOT offsets in AE correction. From left to right: ACOLITE only, ACOLITE with T-Mart AE correction, ACOLITE with T-Mart AE correction and an AOT offset of 0.126. Image scene ID: LC08_L1TP_224077_20160405_20200907_02_T1; GLORIA ID of in situ spectrum: GID_370.

Reference:

Gueymard, C. A., & Yang, D. (2020). Worldwide validation of CAMS and MERRA-2 reanalysis aerosol optical depth products using 15 years of AERONET observations. *Atmospheric Environment*, 225, 117216. <https://doi.org/10.1016/j.atmosenv.2019.117216>

Chapter 3: Accuracy and limitations of optical remote sensing for water quality of small rivers: a case study of two rivers in Eastern Ontario, Canada

Abstract

Optical remote sensing of water quality over small inland waterbodies is challenging due to factors such as the adjacency effect (AE), sub-pixel mixing, and complex water constituents. We evaluated the accuracy and limitations of optical remote sensing for water quality parameters in the South Nation River and the Ottawa River, two small rivers in Eastern Ontario, Canada. Satellite-derived reflectance and water quality parameters were compared with *in situ* measurements. AE correction using T-Mart reduced the sum of RMSE of ACOLITE-derived water-leaving reflectance by 30.4 %, achieving an RMSE of no greater than 0.0124 (dimensionless) across MSI and OLI bands between 400 and 900 nm. The retrieved reflectance with AE correction had a negligible bias in the green and red bands, where water reflectance was high, but showed overestimations in other bands with low water reflectance. Turbidity was well retrieved, with an RMSE of 5 within a range of 2–72 FNU, using the 705 nm band of MSI; AE correction did not significantly improve satellite-derived reflectance in this band, but could be more important for highly turbid waters, such as when FNU > 200. AE correction improved the linear correlation between satellite-derived coloured dissolved organic matter (CDOM) absorption and *in situ* fluorescent dissolved organic matter (fDOM) measurements, but further validation is needed due to uncertainties in the fDOM-CDOM conversion. AE correction improved chlorophyll-a retrievals that, however, remained unsatisfactory with an RMSE of 30 within the range of 2–88 µg/L. Simulated water reflectance using the range of *in situ* water quality measurements as input provided a basis for understanding the accuracy of these retrievals. Improving the retrieval of dissolved organic matter may require enhanced atmospheric correction in visible wavelengths. Accurate retrieval of chlorophyll-a may require hyperspectral sensors, with high signal-to-noise ratios, in wavelengths between 600 and 800 nm, where the reflectance spectra of optically complex waters are most sensitive to changes in chlorophyll-a concentration.

3.1 Introduction

The South Nation River, located in Eastern Ontario, Canada, flows northeast for 175 kilometres from its headwaters north of Brockville, ultimately emptying into the Ottawa River near Plantagenet (South Nation Conservation, 2023). The Ottawa River watershed, in turn, drains into the St. Lawrence River and eventually the Atlantic Ocean. The South Nation River watershed covers approximately 4,000 km² of mostly agricultural land, also including forests and wetlands (Fig. 3.1). The river has a width ranging from 100 to 180 m near its mouth, bordered mostly by vegetation and farmland. These characteristics, combined with the strong reflectance contrast between the water and adjacent land covers, make the South Nation River heavily affected by the adjacency effect (AE), particularly in its narrow sections.

The South Nation River is subject to various pollutants, including non-point source pollutants like agricultural runoff, and point-source pollutants such as raw sewage outflows. Water quality (WQ) degradation could potentially affect multiple aspects of the watershed, lowering the quality of life for people living nearby, causing economic losses to businesses and industry, and disrupting ecological processes (Government of Canada, 2019).

In this chapter, we evaluate the accuracy and limitations of aquatic remote sensing in the lower South Nation watershed and investigate the effectiveness of publicly available high-resolution satellites in monitoring WQ changes. We derive water reflectance from satellite imagery using state-of-the-art atmospheric correction tools, estimate WQ parameters using bio-optical algorithms designed for nearshore waters, and compare the results with *in situ* measurements. We then use the range of *in situ* WQ values as input to simulate inherent optical properties (IOPs) and water reflectance and observe how WQ changes lead to changes in water reflectance spectra; this allows us to interpret the challenges related to WQ retrieval in the study area and provide recommendations for how WQ monitoring of small inland waterbodies can be improved.

3.2 Methods

3.2.1 Field and satellite data

We selected the lower South Nation watershed for this study because its wider waterways, compared to the upstream tributaries, are more suitable for satellite observations. This can provide an indicator for changes occurring across the entire watershed. In addition, we surveyed a section of the Ottawa River, which is wider, less turbid, and contains lower levels of organic matter than the South Nation River (Fig. 3.1). The study design allowed us to evaluate the performance of remote sensing-derived water quality products across different aquatic ecosystems.

Between August and October 2023, six field campaigns resulted in the collection of 119 *in situ* reflectance spectra, coinciding with 10 satellite overpasses from Sentinel 2A (S2A), Sentinel 2B (S2B), Landsat 8 (L8), and Landsat 9 (L9) (Table 3.1). Additionally, Agriculture and Agri-Food Canada supported the collection of 52 sonde measurements at four hydrologically distinct sites

Chapter 3: Adjacency effect correction for regional water quality monitoring

over a period of 13 cloud-free days from May to October 2023, also timed with satellite overpasses (Table 3.2). The locations of these measurements are shown in Fig. 3.1.

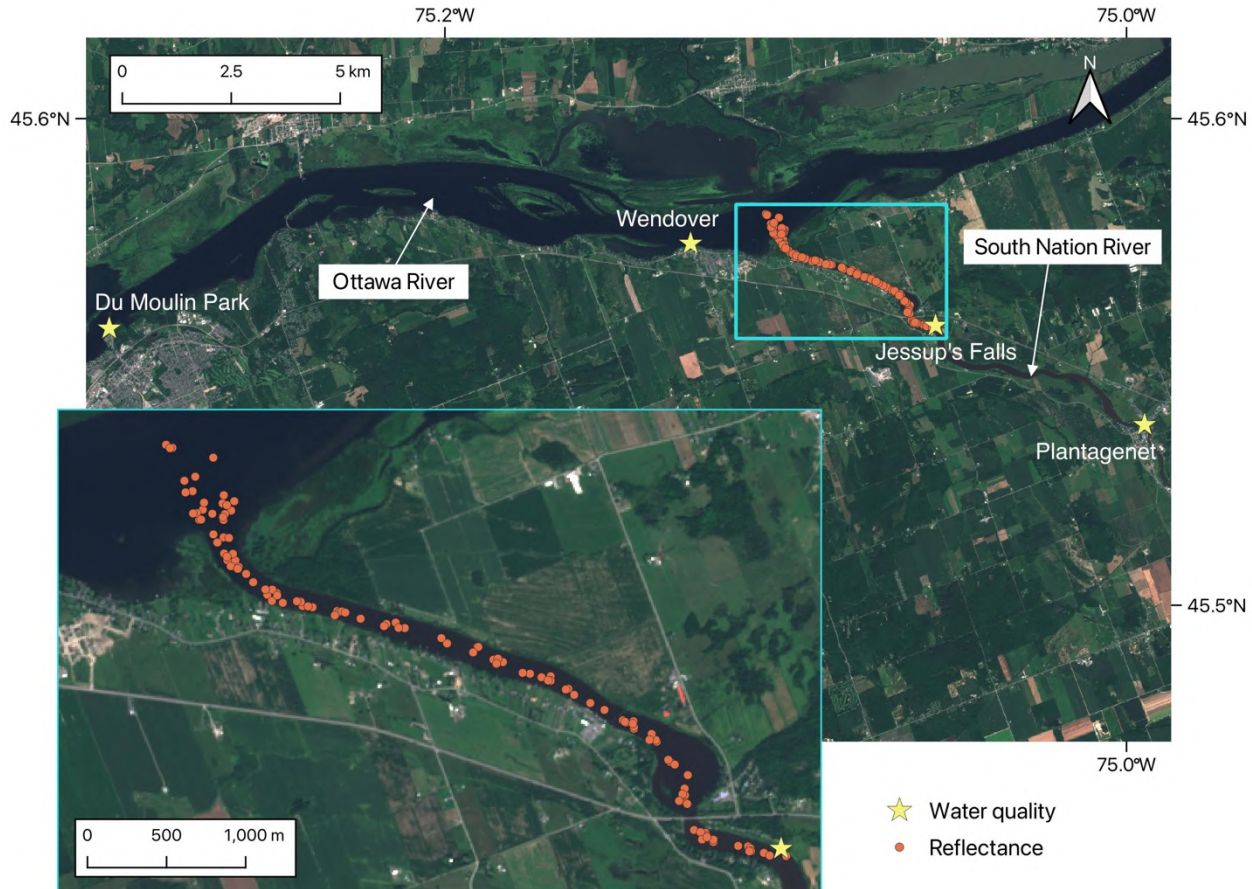


Fig. 3.1. Locations of *in situ* water quality and reflectance data collected in the South Nation River and the Ottawa River in 2023. Each star represents a water-quality site visited once during each of the 13 cloud-free satellite overpass days.

Table 3.1. Satellite overpasses with coincident *in situ* reflectance measurements in 2023.

Date	Overpass
August 06	S2A, L9
August 23	S2A, L8
August 28	S2B
August 31	S2B, L9
September 5	S2A
October 02	S2A, L9

Table 3.2. Satellite overpasses with coincident *in situ* water quality measurements in 2023.

Date	Overpass
May 25	S2A
May 28	S2A
June 22	S2B
July 12	S2B
July 19	S2B
July 24	S2A
August 16	S2A
August 31	S2B, L9
September 05	S2A
September 15	S2A, L8
September 20	S2B
September 22	S2A
September 27	S2B

Remote sensing reflectance (R_{rs}), the ratio of upwelling radiance (L_u) to downwelling irradiance (E_d), was measured with a dual-channel Jaz spectrometer deployed from a small boat. The E_d sensor was mounted on a pole above the passengers, while the L_u sensor was enclosed within a cone with a diameter of 7.5 cm. The base of the cone was submerged 3 cm below the water surface to eliminate specular reflectance and ensure that the measurements reflect only the optical properties of the water's constituents (Lee et al., 2013). To minimize shading effects from the boat, the L_u sensor was always positioned between the boat and the sun during measurements. The sensors were calibrated using seven Spectralon reflectance standards from Labsphere, with reflectance values of 5 %, 10 %, 18 %, 50 %, 80 %, 94 %, and 99 %. For each standard, at least five measurements were taken under illumination conditions similar to those at the study sites. A regression line was fitted to the scatterplot of the ratio of the digital numbers of L_u to E_d against reflectance for each wavelength, and wavelengths with an $R^2 > 0.98$ were retained, generally ranging from 350 to 930 nm. The spectral resolution of the sensors is approximately 0.3 nm. Unlike some reflectance units, R_{rs} accounts for observation angle variability and is relatively robust under varying illumination conditions (Mobley, 2020). Water-leaving reflectance (R_w) was calculated as $R_{rs} \cdot \pi$, assuming water-leaving radiance is isotropic. Correction for anisotropic BRDF was not considered in this study as such process is still under development for inland waters. *In situ* reflectance values were convolved to match the multispectral bands of the satellite sensors using the sensors' spectral response functions.

WQ data were collected using a YSI-EXO3 sonde, which measured parameters including chlorophyll-a (Chl-a) in relative fluorescence units (RFU), fluorescent dissolved organic matter (fDOM) in quinine sulfate units (QSU), and turbidity in Formazin Nephelometric units (FNU). Following the manufacturer's user manual, Chl-a in RFU was converted to concentrations in $\mu\text{g/L}$ by multiplying by 4.02, assuming a measurement temperature of approximately 20 degrees Celsius (YSI, n.d.). fDOM in QSU was converted to absorption of coloured dissolved organic matter at 340 nm, a_{CDOM} (340 nm) (m^{-1}), by multiplying by 0.2, a coefficient obtained in waters from Barnegat Bay and Chincoteague Bay on the East Coast of the US (Oestreich et al., 2016); a_{CDOM} (340 nm) (m^{-1}) was then converted to a_{CDOM} (440 nm) (m^{-1}) using an exponential decay function with a spectral slope of 0.0161 nm^{-1} , the mean value of samples from Lake Erie (Binding et al., 2008).

3.2.2 Atmospheric correction

ACOLITE (Vanhellemont and Ruddick, 2018; Vanhellemont, 2019b) version 20231023.0 was used to derive water-leaving reflectance from satellite imagery, both with and without AE correction using T-Mart version 2.4.5 (Wu et al., 2024). T-Mart uses MERRA2 ancillary data (Global Modeling and Assimilation Office, 2015b) to characterize the optical properties of the atmosphere, which includes aerosol optical thickness at 550 nm (AOT_{550}), and then calculates the point-spread functions of the atmosphere and convolves the satellite imagery to perform AE correction in one band at a time. Detailed descriptions of ACOLITE and T-Mart can be found in the methods section of Chapter 2.

The default settings in both tools were used, with the following modifications:

- For ACOLITE, glint removal (Harmel et al., 2018) and NASA atmospheric ancillary data (OBPG, 2023) were enabled; the negative- R_w filter was disabled to capture sensor-noise-affected low reflectance.
- For both tools, the threshold for the non-water mask using TOA reflectance at 1600 nm was increased from 0.0215 to 0.05, as the default value leads to a large number of water pixels falsely flagged as non-water in the study area.

3.2.3 Water quality retrieval

The calculations of all WQ-retrieval algorithms are listed in Table 3, in which negative R_w values were excluded in the calculations as they do not have a physical meaning. Methods from Gilerson et al. (2010) and Gons et al. (2008) were used to derive Chl-a concentrations. The Gilerson et al. (2010) approach uses the red-edge to red band ratio, and in a comparison study (Pahlevan et al., 2021), it achieved the best performance for inland water observations across multiple AC processors. The Gons et al. (2008) approach, another widely used method, was calibrated using samples from the Great Lakes and was also implemented in this study; this method uses three bands in total: in addition to the two bands used by Gilerson et al. (2010) it uses the 783 nm band to estimate the backscattering coefficient (b_b).

Nechad et al. (2016) recalibrated the semi-empirical single-band turbidity-estimation algorithm originally proposed by Nechad et al. (2009) using a wide range of *in situ* measurements for S2 and L8 bands; the bands achieving best results for the S2 MultiSpectral Instrument (MSI) at 783 nm, and for the L8 Operational Land Imager (OLI) at 865 nm, in Nechad et al. (2016) were used in this study to estimate turbidity. In addition, an MSI band with slightly worse results in Nechad et al. (2016), at 705 nm, which achieved an R^2 of 0.918 (compared to 0.923 for 783 nm), was used in this study as this band was less affected by the AE in the study area.

An algorithm that uses the red-to-green band ratio, calibrated by Mabit et al. (2022) for MSI and OLI, was used to derive a_{CDOM} (440 nm). Using reflectance from ACOLITE as input, it achieved unbiased satellite-based CDOM retrieval at the estuary and Gulf of St. Lawrence and eastern James Bay, Canada (Mabit et al., 2022), and has also been proven to perform well at the global scale for waters high in CDOM (Jiang et al., 2022).

Table 3.3. Water quality retrieval algorithms.

WQ variable	Algorithm	Equation
	Gilerson et al. (2010b)	$\text{Chl-a } (\mu\text{g/L}) = \left(35.75 \cdot \frac{R_w(705 \text{ nm})}{R_w(664 \text{ nm})} - 19.3 \right)^{1.124}$
Chl-a	Gons et al. (2008)	$\text{Chl-a } (\mu\text{g/L}) = \left(\frac{R_w(705 \text{ nm})}{R_w(664 \text{ nm})} \cdot (0.7 + b_{bp}) - 0.4 - b_b^{1.06} \right) / 0.016$ where $b_b = 1.61 \cdot R_w(783 \text{ nm}) / (0.082 - 0.6 \cdot R_w(783 \text{ nm}))$
	Nechad et al. (2016) 705 nm	$\text{Turbidity (FNU)} = 416.32 \cdot \frac{R_w(705 \text{ nm})}{1 - R_w(705 \text{ nm}) / 0.1875}$
Turbidity	Nechad et al. (2016) recommended band	$\text{Turbidity (FNU)} = 1587.80 \cdot \frac{R_w(783 \text{ nm})}{1 - R_w(783 \text{ nm}) / 0.2053}$ for MSI $\text{Turbidity (FNU)} = 3031.75 \cdot \frac{R_w(865 \text{ nm})}{1 - R_w(865 \text{ nm}) / 0.2114}$ for OLI
CDOM	Mabit et al. (2022)	$a_{CDOM} (440 \text{ nm}) (\text{m}^{-1}) = 20 \cdot \log_{10} \left(\frac{R_w(664 \text{ nm})}{R_w(560 \text{ nm})} + 1 \right)^{1.8}$

To test the impact of removing additional nearshore effects — such as shallow water, submerged plants, sub-pixel mixing, and residual AE — on derived spectra and WQ parameters, the water-quality-measurement locations, where coincident satellite-derived reflectance was extracted, were shifted to areas where water pixels are visually homogeneous towards the midlines of the rivers (Fig. 3.2). The shifts were slightly over 100 m for all sites except Plantagenet. At the Plantagenet site, where the measurements were taken from a bridge spanning a narrow waterway, the location was shifted downstream instead. Statistics for matchups with and without the shifting were calculated against the same *in situ* WQ measurements (Section 3.2.4).

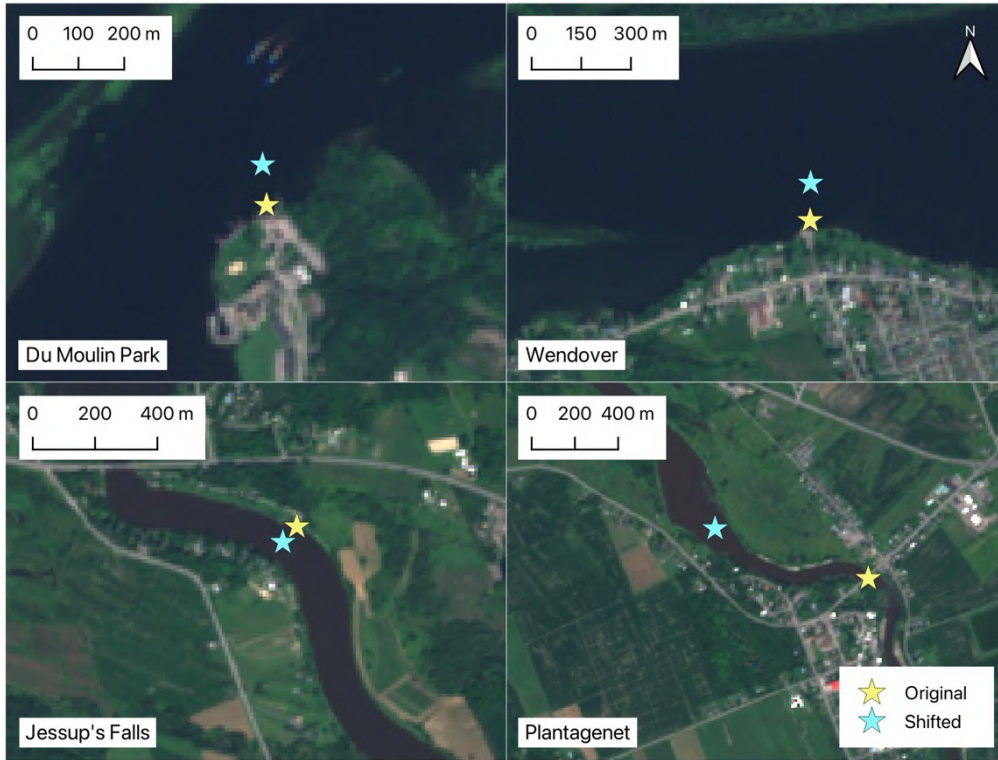


Fig. 3.2. Shifted water-quality-measurement locations to test the impact of residual nearshore effects.

3.2.4 Performance metrics

Root mean squared error (RMSE), symmetric signed percentage bias (β), and median symmetric accuracy (ε) were calculated for satellite-derived R_w , following the steps in Chapter 2. RMSE was calculated for each of the WQ parameters.

3.2.5 Forward modelling

To investigate how variations of WQ parameters in the range of *in situ* measurements affect the magnitude and spectral shape of R_w , and to help interpret the accuracy of retrieved WQ products, we implemented an IOP model provided by Bi et al. (2023). The IOP model was calibrated by, and validated against, a wide variety of oceanic, coastal, and inland water samples. The code is available at <https://github.com/bishun945/IOPmodel>. The model takes as input acDOM (440 nm) and concentrations of Chl-a and suspended particulate matter (SPM), and it outputs spectral absorption and scattering coefficients.

The median and standard deviation (SD) of WQ parameters from all *in situ* measurements were calculated. IOPs were then determined for each WQ parameter with values set at the median ± 2 SD, while keeping the other two parameters fixed at their median concentrations. This allowed us to demonstrate the variations in R_w caused by changes in the concentration of each WQ parameter individually, given the values of the other two parameters but without accounting for interactions between all three parameters. A generic case-2 water phytoplankton community composition was used in the IOP model as the actual phytoplankton composition was unknown;

a sensitivity test showed that this has a negligible impact on the R_w spectra at the relevant concentrations. The IOP model requires SPM in g/m³ instead of turbidity in FNU as input. The conversion was done by simply substituting the unit and using the same numerical values. These two values can vary by up to 10 % depending on the study area (Nechad et al., 2016), a difference considered acceptable for the purposes of the present modeling.

Following Bi et al. (2023), the IOPs calculated by the model were used to simulate R_{rs} through formulas proposed by Lee et al. (2011). This is a simplified radiative transfer method for fast processing, as the purpose of the exercise is only to demonstrate the magnitude of variations. Full radiative transfer models, such as HydroLight (Hedley and Mobley, 2019), can be used when higher accuracy is required. Lastly, R_{rs} was converted to R_w by multiplying by π , assuming isotropic distribution of the water-leaving radiation.

3.3 Results

3.3.1 Atmospheric correction

With T-Mart AE correction, ACOLITE produced R_w values with an RMSE no greater than 0.0124 across all bands (Table 3.4). Regardless of AE correction, reflectance at 560, 664, and 705 nm achieved almost unbiased retrievals. Reflectance in other bands in the 400-900 nm range was overestimated (Fig. 3.3).

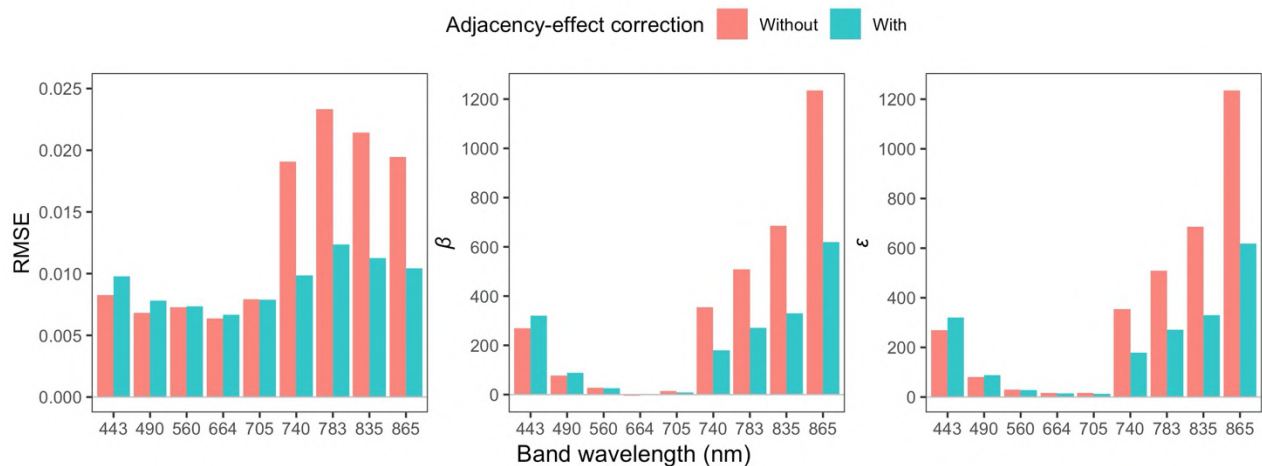


Fig. 3.3. Performance metrics without and with adjacency-effect correction, grouped by wavelength. Bands at 705, 740, 783, and 835 nm belong to Sentinel-2 MSI matchups, and the other bands are shared by Landsat and Sentinel-2. Statistics for different sensors are averaged, weighted by the sample size.

Overall, AE correction improved ACOLITE-derived R_w , lowering the sum of RMSE across the examined nine bands by 30.4 % (Table 3.4). On average, RMSE was reduced by 16.7 %, β was reduced by 38.3 %, and ϵ was reduced by 23.8 % (Table 3.4). AE correction led to significant improvements in red-edge and near-infrared (NIR) bands, but also to slightly worse retrieval for the two blue bands. Overall, overestimation in longer-wavelength bands was reduced, improving the overall spectral shapes of retrieved reflectance.

Table 3.4. Same as Fig. 3.3 but presenting the numerical values and the percentage reductions. Positive/Negative reduction indicates improved/reduced performance, respectively. Reductions greater than 30% are in bold.

Band	RMSE			β (%)			ε (%)		
	Without	With	% reduction	Without	With	% reduction	Without	With	% reduction
443 nm	0.0082	0.0098	-18.7	269.1	319.7	-18.8	269.1	319.7	-18.8
490 nm	0.0068	0.0078	-15.0	76.2	87.5	-14.8	80.7	88.3	-9.4
560 nm	0.0073	0.0074	-1.2	26.9	25.0	6.8	29.8	27.8	6.6
664 nm	0.0064	0.0067	-4.5	-5.0	1.7	66.3	16.8	14.9	11.4
705 nm	0.0079	0.0079	0.3	13.9	8.4	39.6	17.4	12.9	26.0
740 nm	0.0191	0.0099	48.3	354.5	178.8	49.6	354.5	178.8	49.6
780 nm	0.0233	0.0124	46.9	508.4	270.4	46.8	508.4	270.4	46.8
833 nm	0.0214	0.0113	47.4	686.3	329.5	52.0	686.3	329.5	52.0
865 nm	0.0194	0.0104	46.5	1234.8	618.1	49.9	1234.8	618.1	49.9

The distribution of satellite-derived R_w against *in situ* values (Fig. 3.4) was similar to those described in Chapter 2 (Fig. 2.7), which used *in situ* values from the GLORIA database (Lehmann et al., 2023). The biggest difference was in the 443 nm band — the range of *in situ* reflectance in this band in this chapter was significantly lower than the one from GLORIA (0–0.01 vs. 0–0.085).

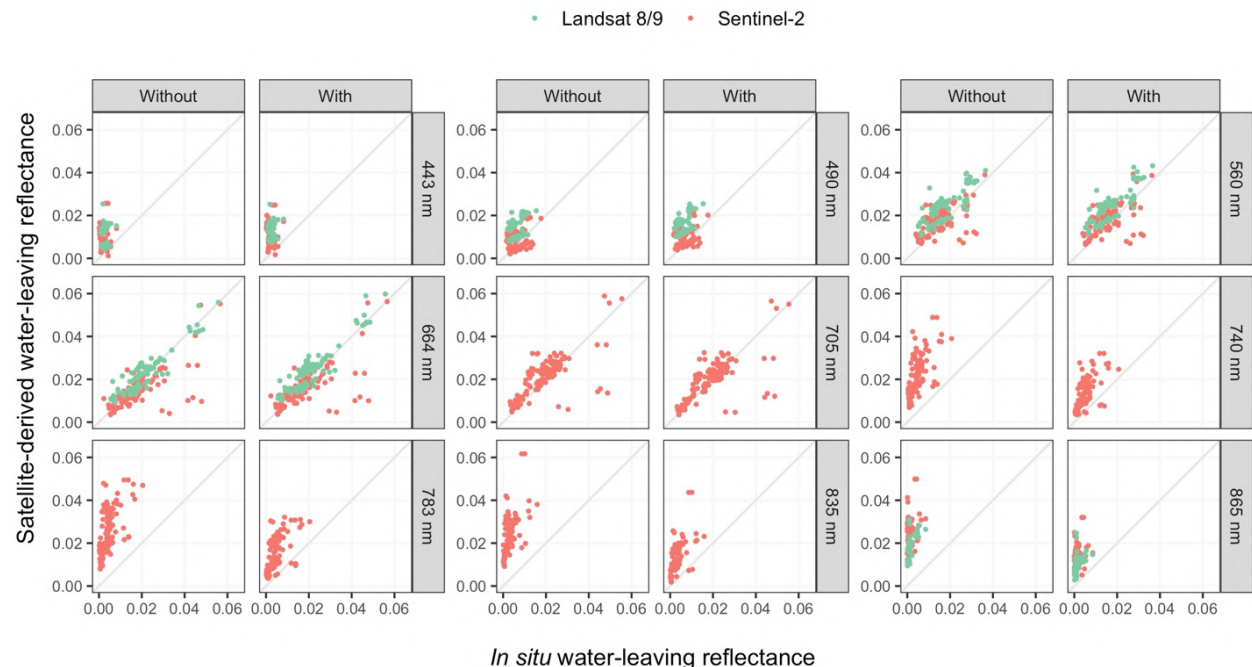


Fig. 3.4. Satellite-derived water-leaving reflectance compared with *in situ* values, without and with adjacency-effect correction. Points are coloured by sensor.

With AE correction, ACOLITE-estimated AOT_{550} was lowered from a median of 0.230 to 0.165, and thus less overestimated compared to the MERRA2 median value of 0.095 (Fig. 3.5).

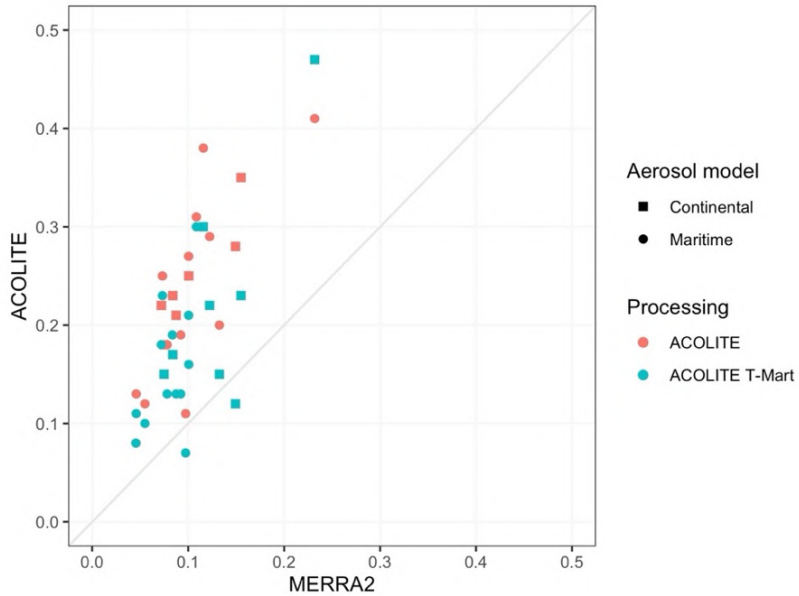


Fig. 3.5. Comparison of ACOLITE-derived and MERRA2 AOT₅₅₀ values. Shapes indicate types of aerosol models. One data point (MERRA2: 0.24, ACOLITE: 0.91) is excluded from the plot, for which AE correction had little impact because very few pixels were identified as water in that scene and AE correction was only applied to water pixels.

3.3.2 Water quality retrieval

The input to bio-optical algorithms, satellite-derived R_w spectra, were extracted at the four water quality measurement sites (Fig. 3.6). The four sites can be divided into two groups: Du Moulin Park and Wendover sites along the Ottawa River, and Jessup's Falls and Plantagenet along the South Nation River. Satellite-derived reflectance exhibited greater variation at the two South Nation River sites compared to the two Ottawa River sites (Fig. 3.6). A few retrieved reflectance values at the Ottawa River sites deviated significantly from the spectral shapes of natural waters, exhibiting unusually high reflectance in the red-edge and NIR bands. These anomalies were largely associated with instances of high AOTs.

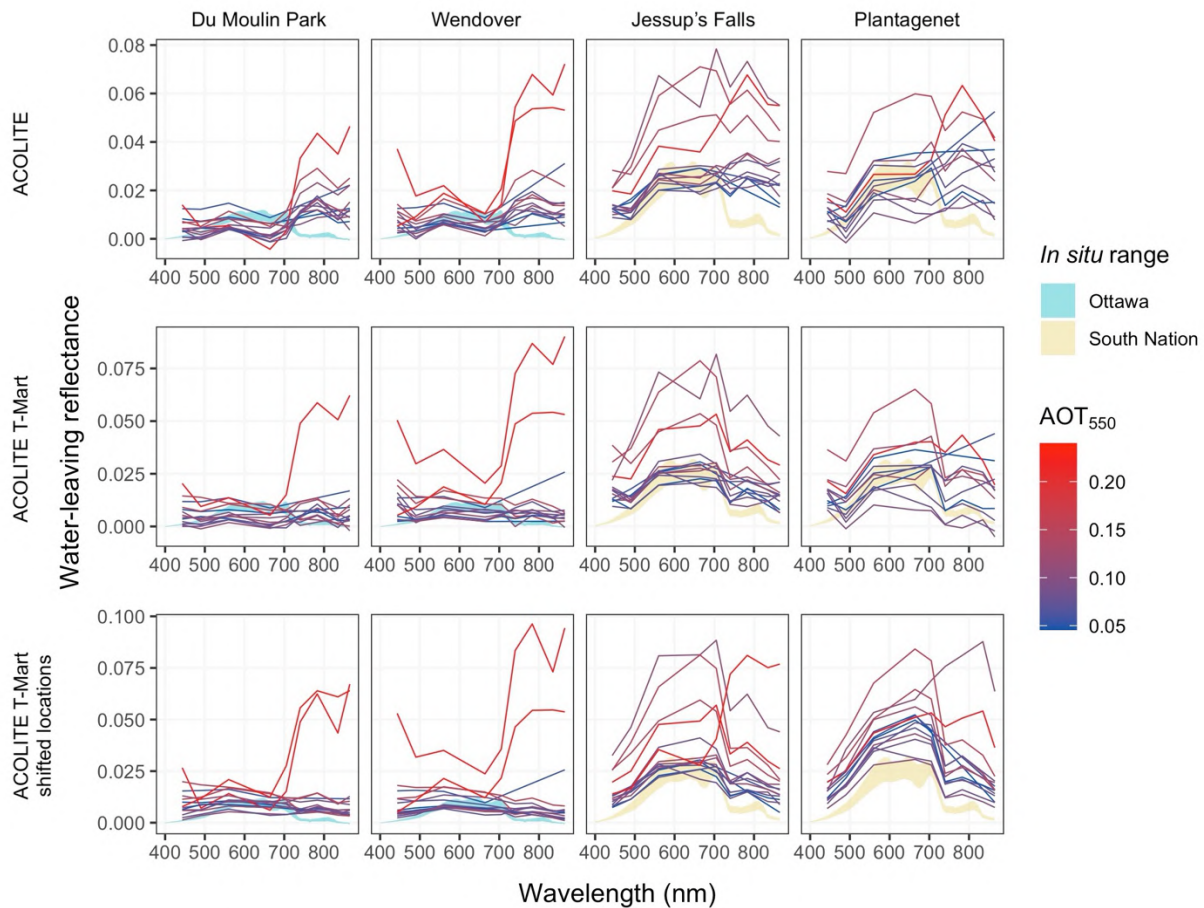


Fig. 3.6. Satellite-derived water-leaving reflectance at four water-quality sites, used as input to bio-optical algorithms, alongside coincident *in situ* water quality measurements. Shaded areas indicate the interquartile range of *in situ* reflectance for each river. Lines are coloured by MERRA2 AOT₅₅₀ values at the time of image acquisition.

An overview of the performance of WQ-retrieval algorithms is provided in Table 3.5. Compared to ACOLITE-only retrievals, AE correction benefited all WQ retrievals except those based on the Nechad et al. (2016) approach using the 705 nm band. For Chl-a retrieval, RMSE was reduced with AE correction for both approaches, from 87.2 to 59.7 µg/L (Gilerson et al., 2010) and from 93.5 to 74.4 µg/L (Gons et al., 2008). For turbidity retrieval, AE correction reduced the RMSE from 61.3 to 43.2 FNU (Nechad et al., 2016) using the 783 and 865 nm bands, while the approach using the 705 nm band achieved a very low RMSE of 4.9–7.1 FNU across the three atmospheric correction scenarios. For acDOM (440 nm) retrieval, AE correction reduced the RMSE from 1.78 to 1.48 m⁻¹. When using the shifted locations for matchups, accuracy for Chl-a retrievals was improved, especially following the Gilerson et al. (2010) approach, achieving an RMSE of 30.0 µg/L, and acDOM (440 nm) retrieval was improved to 1.26 m⁻¹.

Table 3.5. Overview of water-quality-retrieval algorithms and their performances. RMSE values were not calculated for CDOM retrievals due to multiple-conversion uncertainties (Section 3.2.1). Methods in bold are plotted in Fig. 3.7.

Method	Chlorophyll-a		Turbidity		CDOM
	Gilerson et al. (2010)	Gons et al. (2008)	Nechad et al. (2016)	Nechad et al. (2016)	Mabit et al. (2022)
Band(s)	664 nm, 705 nm	664nm, 705 nm, 783 nm	705 nm	783 nm (MSI), 865 nm (OLI)	560 nm, 664 nm
Sensor	MSI only	MSI only	MSI only	MSI, OLI	MSI, OLI
n	52	52	52	60	60
<i>In situ</i> range	2.4–87.5 µg/L		1.9–72.4 FNU		48.9–130.0 QSU 2.0–5.2 a_{CDOM} (440 nm) (m^{-1})
ACOLITE	87.2	93.5	4.9	61.3	1.78
RMSE	ACOLITE T-Mart	59.7	74.4	5.4	43.2
	ACOLITE T-Mart shifted locations	30.0	66.9	7.1	43.0
					1.26

The derived products of selected algorithms, Gilerson et al. (2010), Nechad et al. (2016), and Marit et al. (2022), were plotted against *in situ* values in Fig. 3.7.

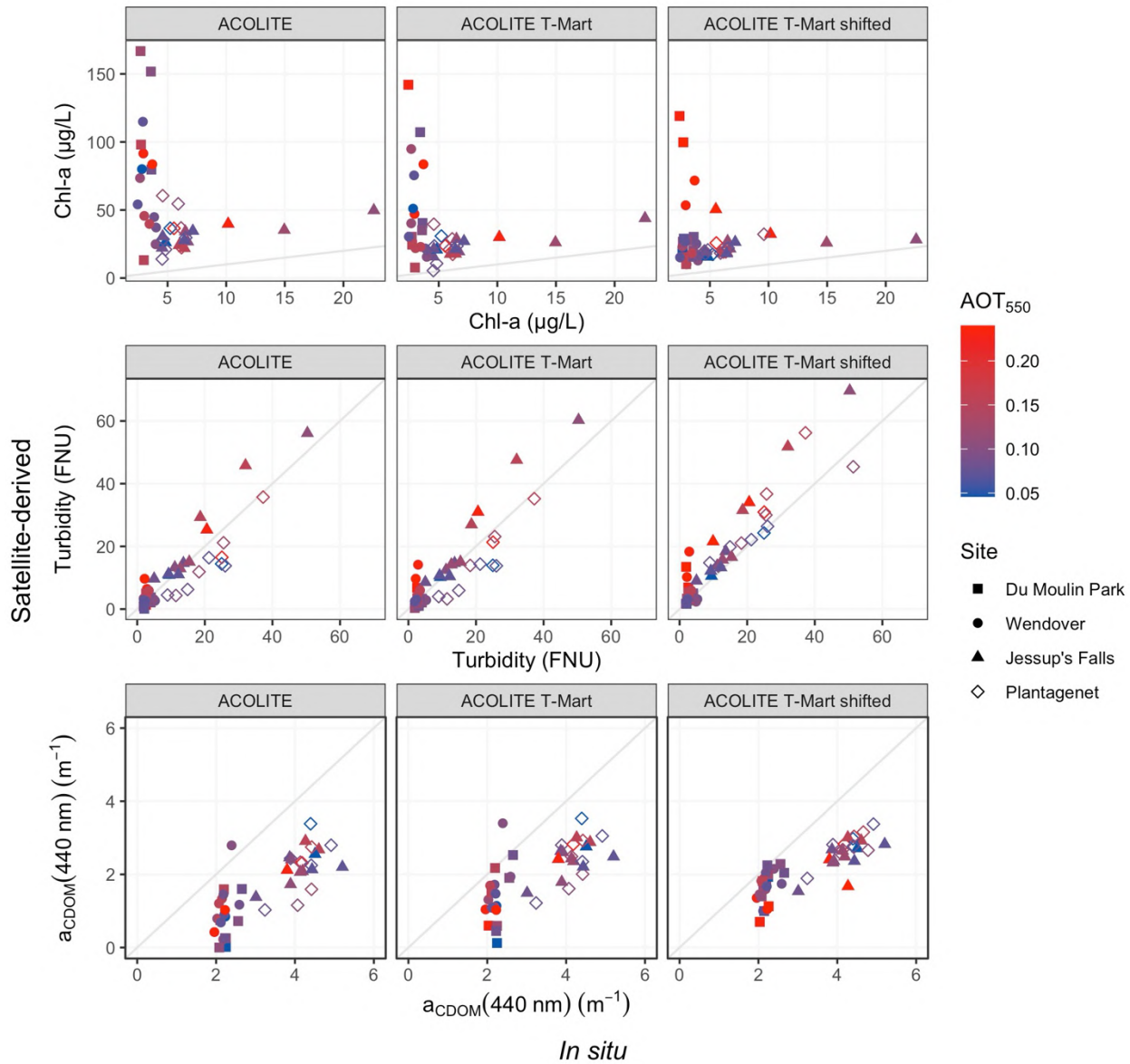


Fig. 3.7. Evaluation of satellite-derived water quality parameters against *in situ* values. Shapes are coloured by MERRA2 AOT₅₅₀ at the time of image acquisition. Grey lines for Chl-a and Turbidity represent 1:1 relationship.

Turbidity and a_{CDOM} showed good linearity between satellite-derived and *in situ* measurements, and turbidity was well retrieved with most points close to the 1:1 line and slight overestimates on high-AOT days (Fig. 3.7). Results for Chl-a were poor, with largely overestimated values especially for the two Ottawa River sites (Du Moulin Park and Wendover). The Chl-a values were less overestimated in the shifted-matchup-locations scenario, with remaining extreme overestimates associated with high AOTs (Fig. 3.7).

AE correction increased satellite-derived a_{CDOM} (440 nm) values, raising the mean from 1.69 to 1.96 m⁻¹ and the median from 1.59 to 1.97 m⁻¹. The distribution of the a_{CDOM} points was more linear for the shifted-matchup-location scenario, suggesting residual nearshore effects on

retrieved R_w outweigh the spatial variation of the variable. Performance of turbidity and CDOM retrievals did not vary significantly across sites.

3.3.3 Forward modelling

The median and SD of *in situ* WQ measurements are listed in Table 3.6, while the variations of R_w as a function of WQ changes are plotted in Fig. 3.8. Changes in Chl-a resulted in very small spectral changes within the 2 SD range, mostly reflected in the absorption line centred around 675 nm as well as the increased reflectance beyond 700 nm due to increased particle backscattering (Fig. 3.8a). It should be noted that sun-induced Chl-a fluorescence was not included in the modelling, which would lead to an increase in modelled water reflectance around 700 nm at high Chl-a concentrations. In contrast, changes in SPM concentration led to significant changes across the entire visible-NIR spectrum in both magnitude and shape (Fig. 3.8b), and changes in a_{CDOM} caused moderate spectral changes at wavelengths shorter than 700 nm (Fig. 3.8c).

Table 3.6. Median and SD of *in situ* WQ measurements.

	Chl-a ($\mu\text{g/L}$)	SPM (g/m^3)	a_{CDOM} (440 nm) (m^{-1})
Median	4.02	5.27	3.01
SD	11.28	15.32	1.09

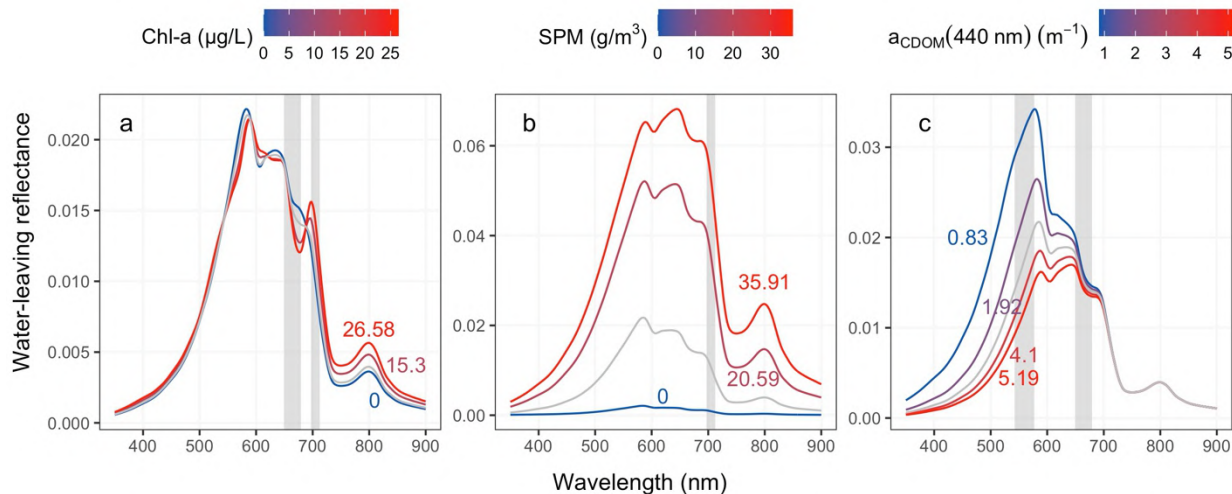


Fig. 3.8. Simulated water-leaving reflectance with various concentrations of WQ parameters (median \pm 2 SD). The grey reflectance spectra correspond to median concentrations: Chl-a at $4.02 \mu\text{g/L}$, suspended particulate matter at 5.27 g/m^3 , and a_{CDOM} (440 nm) at 3.01 m^{-1} . Grey vertical bands indicate spectral ranges of sensor bands used for calculating satellite-derived values.

3.4 Discussion

3.4.1 Atmospheric correction

With AE correction, ACOLITE achieved satisfactory accuracy in the derived R_w , with an RMSE no greater than 0.0124 across all bands (Table 3.4). The community validation database used in the ACIX-Aqua atmospheric correction inter-comparison (Pahlevan et al., 2021) includes R_w mostly from a diverse range of freshwater ecosystems; in the excise, ACOLITE achieved the best performance among 8 atmospheric correction processors in terms of RMSE, which was 0.0224, 0.0196, 0.0197, 0.0147, 0.0139, 0.0168, and 0.0168 for bands at 443, 490, 560, 664, 705, 740, and 783 nm respectively (Pahlevan et al., 2021). The RMSE achieved in this study using ACOLITE, with AE correction, was better than RMSE validated against the community validation database in all bands (Table 3.4), yet still with non-negligible bias as high as 618 % for low-reflectance bands. The extreme overestimation was likely due to extremely low reflectance, e.g., near 0 at 865 nm (Fig. 3.4), potentially shallow-water bottom effects, floating plant parts captured by satellite sensors, and incomplete AE correction due to violation of assumptions such as the vertical structure of trees on the shores.

AE correction improved or had a negligible effect on all bands except the two blue bands (Fig. 3.3 and Table 3.4). The overestimation of satellite-derived R_w at 443 nm persisted with AE correction but was negligible at offshore sites (Fig. 3.6). Potential reasons for this increase include errors in estimated atmospheric pressure and sky glint during atmospheric correction, sensor calibrations issues, and the 60 m resolution of MSI Band 1 which makes it more susceptible to sub-pixel mixing than the other bands.

In addition, the self-shading effect inherent in the skylight-blocked approach was not corrected for in the collected R_w . This effect lowers measured water reflectance, particularly in high-absorption bands. Applying a correction for this effect could significantly increase measured *in situ* water reflectance in the high-absorption blue and NIR bands, potentially improving the statistics of the currently overestimated satellite-derived water reflectance, both with and without AE correction (Fig. 3.4).

With AE correction, the median ACOLITE-estimated AOT₅₅₀ was 28 % lower (Fig. 3.5) than values without AE correction. ACOLITE is known to overestimate AOT (Vanhellemont and Ruddick, 2018), likely to compensate for the AE and other factors. The overestimation was reduced from 142 % to 73 % compared to MERRA2 values after applying AE correction. This improvement brings the AOT estimates used in aquatic remote sensing closer to the values in climatology models, contributing to more unified observations across aquatic and atmospheric domains.

3.4.2 Water quality retrieval

The variations in the accuracy of WQ retrievals (Table 3.5 and Fig. 3.7) can be explained by the simulated R_w spectra as a function of WQ changes (Fig. 3.8). For Chl-a, both Gilerson et al. (2010) and Gons et al. (2008) approaches should in theory be able to detect the variation of

chlorophyll absorption, using the 664 nm and 705 nm bands; however, this is challenging due to the noise from atmospheric correction (Fig. 3.4 and Fig. 3.6) as well as the wide bandwidths. MSI has full-width-half-maximum band widths of 30 and 15 nm for the 664 and 705 nm bands, respectively (ESA, 2015), these may be too broad to resolve the Chl-a absorption band at ~675 nm. In addition, at the longer wavelengths around 750-800 nm where Chl-a variations also influence the R_w spectrum, the modelled impact of Chl-a variations on R_w was smaller (~0.001, see Fig. 3.8) compared to the RMSE values for these bands (~0.01, see Fig. 3.3) by an order of magnitude. We likely need narrow-band or even hyperspectral sensors to capture fine spectral features between 600 and 800 nm to accurately derive Chl-a in environments similar to the study area (Fig. 3.8a).

AE correction improved the retrieval of Chl-a in the study area (Table 3.5). While the R_w RMSE for the 664 and 705-nm bands, the main input to the Chl-a algorithms, were not significantly improved by AE correction. β and ε showed noticeable improvement (Table 3.4), suggesting reduced bias or improved spectral shape may have improved the Chl-a retrieval. It should be noted that the fluorescence-based *in situ* Chl-a measurements suffer from uncertainties too. A more rigorous assessment of the accuracy of satellite-derived Chl-a requires lab techniques such as in-vitro fluorescence or high-performance liquid chromatography.

Changes in turbidity were well retrieved using the 705-nm band (Table 3.5 and Fig. 3.7), achieving an RMSE of 4.9 within the range of 1.9–72.4 FNU, very likely due to the sensitivity of the water spectra to turbidity variations in the study area (Fig. 3.8b). The 705-nm band did not benefit significantly from AE correction, which is reflected both in the evaluated spectral statistics (Fig. 3.3 and Table 3.4) and the retrieved WQ (Table 3.5). However, in situations when SPM is higher, such as over 200 g/m³, the 705-nm band saturates and responds to concentration changes less linearly, and the longer-wavelength bands should instead be used to estimate SPM and turbidity (Shen et al., 2010). In such cases, AE correction could be important given significantly improved R_w retrievals in these bands with AE correction.

Spectral changes in response to CDOM variations are smooth and span a wide spectrum in visible wavelengths (Fig. 3.8c), supporting the findings of Mabit et al. (2022) that the wide multispectral bands of high-spatial-resolution sensors, specifically the red and green bands of MSI and OLI, can be used to retrieve acDOM (440 nm). This aligns with the clear linear relationship observed between satellite-derived and *in situ* values (Fig. 3.7), highlighting the potential for monitoring CDOM in the study area. The linear relationship was even stronger with shifted matchup locations, despite the potential risk of spatial CDOM heterogeneity, suggesting that residual nearshore effects on atmospheric correction may play a more significant role in acDOM retrieval than algorithm development or improved spectral resolution. These residual nearshore effects, including shallow water, submerged plants, sub-pixel mixing, and residual AE, particularly in the visible wavelengths, should be addressed to enhance CDOM monitoring in environments similar to the study area. Additionally, a multi-band approach could reduce the impact of sensor random noise (Ibrahim et al., 2019), while machine-learning techniques may prove useful in areas where residual nearshore effects persist consistently. However, all these strategies require further evaluation due to the lack of direct *in situ* acDOM measurements in this study.

3.5 Conclusion

A total of 119 *in situ* reflectance spectra and 63 sonde measurements of water quality parameters, coinciding with 10 Sentinel-2 and 16 Landsat 8/9 overpasses, were collected between May and October 2023 in the South Nation and Ottawa rivers of Ontario, Canada. Satellite-derived R_w and WQ parameters were compared with *in situ* measurements to assess the potential for satellite-based WQ monitoring in these rivers, which run through largely agricultural landscapes. In the study area, T-Mart AE correction improved ACOLITE-retrieved R_w for all visible-NIR bands except two blue bands with low R_w values. Overall, AE correction lowered the sum of RMSE of ACOLITE-derived R_w by 30.4 %, enabling ACOLITE to achieve an RMSE of R_w no greater than 0.0124 across the visible-NIR spectrum; bias was low for wavelengths where water-leaving reflectance was high but can be non-negligible in low-reflectance bands, potentially due to the uncorrected self-shading effect inherent in *in situ* reflectance data collected through the skylight-blocked approach.

AE correction improved Chl-a retrieval, which, however, remained poor, achieving an RMSE of 30.0 for values ranging from 2.4 to 87.5 µg/L in the best scenario. AE correction also improved the retrieval of turbidity using bands recommended by Nechad et al. (2016). However, the best result with an RMSE of 5 within a range of 2–72 FNU was achieved using the 705 nm band, which did not benefit from AE correction in this study. AE correction may be important for more turbid waters, such as when SPM > 200 g/m³. For CDOM, a strong linearity was found between satellite-derived and *in situ* values; a direct comparison of satellite-derived and *in situ* measurements is needed to further validate the retrievals.

Given the errors in satellite-derived water reflectance (Fig. 3.4 and Table 3.4), better atmospheric correction and sensor calibration, coupled with more *in situ* validation, are likely needed to improve the retrieval of the three WQ products. Accurate retrieval of acDOM may require improved atmospheric correction in visible wavelengths. Satellite-based retrieval of Chl-a is especially challenging due to the small spectral change in response to Chl-a variations; its accurate retrieval may require hyperspectral sensors with high signal-to-noise ratios, especially in wavelengths between 600 and 800 nm where R_w is most sensitive to changes in Chl-a concentration in optically complex waters.

Conclusion

This thesis comprises three chapters that address the problem of the adjacency effect (AE) in nearshore aquatic remote sensing. In Chapter 1, we introduced a three-dimensional radiative transfer model designed for AE modelling, named T-Mart. The model uses molecular and aerosol profiles from 6S (Wilson, 2013) and supports arbitrary topography. The chapter details the characterization of the optical properties of the surface and the atmosphere and how radiative quantities are calculated through a Monte Carlo approach. The accuracy of the model was validated against libRadtran, showing a maximum difference of less than 0.6 % in extreme optical settings. Case studies demonstrated the use of T-Mart in investigating the AE in custom environments. For example, one case study showed that 83.7 % of the variance in near-infrared top-of-atmosphere reflectance of 47 lakes in Minnesota, as observed in a Sentinel-2 scene, could be attributed to the AE. In addition, modelled and measured reflectances in the same scene aligned closely with each other.

In Chapter 2, we derived a physics-based method for AE correction, building upon the T-Mart code. Ancillary data is first used to calculate the optical properties of the atmosphere, which are then used to compute the atmospheric point-spread function. A satellite image is convolved, one band at a time, and the difference between the convolved and observed reflectances is scaled by a factor derived from radiative transfer simulations. The scaled difference is subsequently removed from the observed reflectance to correct for the AE. The performance of AE correction was evaluated by deriving water-leaving reflectance from Sentinel-2 and Landsat 8 imagery using ACOLITE, POLYMER and l2gen, with and without AE correction, and comparing the results to *in situ* reflectance data from the globally distributed GLORIA dataset (Lehmann et al., 2023). For matchups within 200 m of shorelines ($n = 212$), applying AE correction led to an average reduction of 16.7 % in root mean squared error (RMSE), 32.4 % in symmetric signed percentage bias, and 36.8 % in median symmetric accuracy for the three processors. The improvements were most notable in the near-infrared (NIR) range for ACOLITE, in visible wavelengths for l2gen, and evenly distributed across the visible-NIR spectrum for POLYMER.

In Chapter 3, we evaluated the accuracy and limitations of optical remote sensing for small rivers by comparing satellite-derived water-leaving reflectance and water quality parameters with *in situ* measurements in two small rivers within the lower South Nation River watershed. AE correction improved ACOLITE-retrieved water-reflectance retrievals across most bands, except for the two bands where water reflectance was negligible. Overall, AE correction reduced the sum of RMSE across nine visible-NIR bands by 30.4 %, enabling ACOLITE to achieve an RMSE for R_w no greater than 0.0124. Bias was low for wavelengths with high water-leaving reflectance and was non-negligible in bands with low reflectance. While turbidity was well retrieved, there is room for improvement in retrieving coloured-dissolved-organic-matter (CDOM) absorption and chlorophyll-a concentration (Chl-a). Accurate CDOM absorption may require improved atmospheric correction in visible wavelengths, and accurate retrieval of Chl-a may require hyperspectral sensors with high signal-to-noise ratios, particularly in the 600–800 nm range, where water-leaving reflectance is most sensitive to variations in Chl-a concentration in optically complex waters.

Conclusion

In addition to the AE, nearshore aquatic remote sensing faces various challenges that must be addressed to accurately retrieve optically active water quality products. Beyond the need for new-generation sensors and rigorous sensor calibration, atmospheric correction poses difficulties including the influence of shallow water (Richardson et al., 2024), estimating aerosol optical thickness in the presence of non-negligible reflectance in shortwave infrared bands (Houskeeper and Hooker, 2023), sun glint (Kay et al., 2009), spatial variations in atmospheric pressure and Rayleigh scattering (Gilerson et al., 2022), the intricate polarization states of radiation at the water surface (Foster and Gilerson, 2016) and below it (Jamet et al., 2019), and sub-pixel mixing of plant parts and land reflectance. Furthermore, the proposed AE correction itself has limitations, including unaddressed impacts of clouds and spatial variability in observation geometry, as well as assumptions of flat, isotropically scattering surfaces and horizontally homogeneous atmospheric conditions. Despite these challenges, the open-source and publicly available AE modelling and correction software developed in this thesis marks a critical advancement in improving the accuracy of aquatic remote sensing in nearshore environments, serving as a foundation for more refined methodologies in future research.

References

- Ahmad, Z., Franz, B.A., McClain, C.R., Kwiatkowska, E.J., Werdell, J., Shettle, E.P., Holben, B.N., 2010. New aerosol models for the retrieval of aerosol optical thickness and normalized water-leaving radiances from the SeaWiFS and MODIS sensors over coastal regions and open oceans. *Appl. Opt.* 49, 5545. <https://doi.org/10.1364/AO.49.005545>
- Antoine, D., Morel, A., 1999. A multiple scattering algorithm for atmospheric correction of remotely sensed ocean colour (MERIS instrument): Principle and implementation for atmospheres carrying various aerosols including absorbing ones. *International Journal of Remote Sensing* 20, 1875–1916. <https://doi.org/10.1080/014311699212533>
- Bailey, S.W., Franz, B.A., Werdell, P.J., 2010. Estimation of near-infrared water-leaving reflectance for satellite ocean color data processing. *Opt. Express* 18, 7521. <https://doi.org/10.1364/OE.18.007521>
- Bailey, S.W., Werdell, P.J., 2006. A multi-sensor approach for the on-orbit validation of ocean color satellite data products. *Remote Sensing of Environment* 102, 12–23. <https://doi.org/10.1016/j.rse.2006.01.015>
- Balasubramanian, S.V., Pahlevan, N., Smith, B., Binding, C., Schalles, J., Loisel, H., Gurlin, D., Greb, S., Alikas, K., Randa, M., Bunkei, M., Moses, W., Nguyẽn, H., Lehmann, M.K., O'Donnell, D., Ondrusk, M., Han, T.-H., Fichot, C.G., Moore, T., Boss, E., 2020. Robust algorithm for estimating total suspended solids (TSS) in inland and nearshore coastal waters. *Remote Sensing of Environment* 246, 111768. <https://doi.org/10.1016/j.rse.2020.111768>
- Barsi, J., Lee, K., Kvaran, G., Markham, B., Pedelty, J., 2014. The Spectral Response of the Landsat-8 Operational Land Imager. *Remote Sensing* 6, 10232–10251. <https://doi.org/10.3390/rs61010232>
- Bélanger, S., Ehn, J.K., Babin, M., 2007. Impact of sea ice on the retrieval of water-leaving reflectance, chlorophyll a concentration and inherent optical properties from satellite ocean color data. *Remote Sensing of Environment* 111, 51–68. <https://doi.org/10.1016/j.rse.2007.03.013>
- Berk, A., Conforti, P., Kennett, R., Perkins, T., Hawes, F., van den Bosch, J., 2014. MODTRAN® 6: A major upgrade of the MODTRAN® radiative transfer code, in: 2014 6th Workshop on Hyperspectral Image and Signal Processing: Evolution in Remote Sensing (WHISPERS). Presented at the 2014 6th Workshop on Hyperspectral Image and Signal Processing: Evolution in Remote Sensing (WHISPERS), IEEE, Lausanne, Switzerland, pp. 1–4. <https://doi.org/10.1109/WHISPERS.2014.8077573>
- Bi, S., Hieronymi, M., Röttgers, R., 2023. Bio-geo-optical modelling of natural waters. *Front. Mar. Sci.* 10, 1196352. <https://doi.org/10.3389/fmars.2023.1196352>
- Binding, C., Jerome, J., Bukata, R., Booty, W., 2008. Spectral absorption properties of dissolved and particulate matter in Lake Erie. *Remote Sensing of Environment* 112, 1702–1711. <https://doi.org/10.1016/j.rse.2007.08.017>
- Binding, C.E., Greenberg, T.A., Jerome, J.H., Bukata, R.P., Letourneau, G., 2011. An assessment of MERIS algal products during an intense bloom in Lake of the Woods. *Journal of Plankton Research* 33, 793–806. <https://doi.org/10.1093/plankt/fbq133>
- Boss, E.S., Collier, R., Larson, G., Fennel, K., Pegau, W.S., 2007. Measurements of spectral optical properties and their relation to biogeochemical variables and processes in Crater Lake, Crater Lake National Park, OR. *Hydrobiologia* 574, 149–159. <https://doi.org/10.1007/s10750-006-2609-3>
- Bulgarelli, B., Kiselev, V., Zibordi, G., 2017. Adjacency effects in satellite radiometric products from coastal waters: a theoretical analysis for the northern Adriatic Sea. *Appl. Opt.* 56, 854. <https://doi.org/10.1364/AO.56.000854>
- Bulgarelli, B., Kiselev, V., Zibordi, G., 2014. Simulation and analysis of adjacency effects in coastal waters: a case study. *Appl. Opt.* 53, 1523. <https://doi.org/10.1364/AO.53.001523>
- Bulgarelli, B., Zibordi, G., 2018. On the detectability of adjacency effects in ocean color remote sensing of mid-latitude coastal environments by SeaWiFS, MODIS-A, MERIS, OLCI, OLI and MSI. *Remote Sensing of Environment* 209, 423–438. <https://doi.org/10.1016/j.rse.2017.12.021>
- Bulgarelli, B., Zibordi, G., Mélin, F., 2018. On the minimization of adjacency effects in SeaWiFS primary data products from coastal areas. *Opt. Express* 26, A709. <https://doi.org/10.1364/OE.26.00A709>
- Buras, R., Mayer, B., 2011. Efficient unbiased variance reduction techniques for Monte Carlo simulations of radiative transfer in cloudy atmospheres: The solution. *Journal of Quantitative Spectroscopy and Radiative Transfer* 112, 434–447. <https://doi.org/10.1016/j.jqsrt.2010.10.005>
- Cox, C., Munk, W., 1954. Measurement of the Roughness of the Sea Surface from Photographs of the Sun's Glitter. *J. Opt. Soc. Am.* 44, 838. <https://doi.org/10.1364/JOSA.44.000838>
- De Keukelaere, L., Sterckx, S., Adriaensen, S., Knaeps, E., Reusen, I., Giardino, C., Bresciani, M., Hunter, P., Neil, C., Van der Zande, D., Vaiciute, D., 2018. Atmospheric correction of Landsat-8/OLI and Sentinel-2/MSI data using iCOR algorithm: validation for coastal and inland waters. *European Journal of Remote Sensing* 51, 525–542. <https://doi.org/10.1080/22797254.2018.1457937>
- Dee, D.P., Uppala, S.M., Simmons, A.J., Berrisford, P., Poli, P., Kobayashi, S., Andrae, U., Balmaseda, M.A., Balsamo, G., Bauer, P., Bechtold, P., Beljaars, A.C.M., Van De Berg, L., Bidlot, J., Bormann, N., Delsol, C., Dragani, R., Fuentes, M., Geer, A.J., Haimberger, L., Healy, S.B., Hersbach, H., Hölm, E.V., Isaksen, L., Källberg, P., Köhler, M., Matricardi, M., McNally, A.P., Monge-Sanz, B.M., Morcrette, J.-J., Park, B.-K., Peubey, C., De Rosnay, P., Tavolato, C., Thépaut, J.-N., Vitart, F., 2011. The ERA-Interim reanalysis: configuration and performance of the data assimilation system. *Quart J Royal Meteorol Soc* 137, 553–597. <https://doi.org/10.1002/qj.828>

References

- Dierssen, H.M., Ackleson, S.G., Joyce, K.E., Hestir, E.L., Castagna, A., Lavender, S., McManus, M.A., 2021. Living up to the Hype of Hyperspectral Aquatic Remote Sensing: Science, Resources and Outlook. *Front. Environ. Sci.* 9, 649528. <https://doi.org/10.3389/fenvs.2021.649528>
- Ehret, G., Kiemle, C., Wirth, M., Amediek, A., Fix, A., Houweling, S., 2008. Space-borne remote sensing of CO₂, CH₄, and N₂O by integrated path differential absorption lidar: a sensitivity analysis. *Appl. Phys. B-Lasers Opt.* 90, 593–608. <https://doi.org/10.1007/s00340-007-2892-3>
- Emde, C., Buras-Schnell, R., Kylling, A., Mayer, B., Gasteiger, J., Hamann, U., Kylling, J., Richter, B., Pause, C., Dowling, T., Bugliaro, L., 2016. The libRadtran software package for radiative transfer calculations (version 2.0.1). *Geosci. Model Dev.* 9, 1647–1672. <https://doi.org/10.5194/gmd-9-1647-2016>
- ESA, 2023. Sentinel-2 Spectral Response Functions (S2-SRF) [WWW Document]. Sentinel Online. URL https://copernicus.eu/user-guides/sentinel-2-msi/document-library/-/asset_publisher/Wk0TKajiISaR/content/sentinel-2a-spectral-responses (accessed 1.23.24).
- ESA, 2015. Sentinel-2 User Handbook. https://sentinel.esa.int/documents/247904/685211/Sentinel-2_User_Handbook
- Feng, L., Hu, C., 2016. Cloud adjacency effects on top-of-atmosphere radiance and ocean color data products: A statistical assessment. *Remote Sensing of Environment* 174, 301–313. <https://doi.org/10.1016/j.rse.2015.12.020>
- Foster, R., Gilerson, A., 2016. Polarized transfer functions of the ocean surface for above-surface determination of the vector submarine light field. *Appl. Opt.* 55, 9476. <https://doi.org/10.1364/AO.55.009476>
- Frouin, R.J., Franz, B.A., Ibrahim, A., Knobelspiesse, K., Ahmad, Z., Cairns, B., Chowdhary, J., Dierssen, H.M., Tan, J., Dubovik, O., Huang, X., Davis, A.B., Kalashnikova, O., Thompson, D.R., Remer, L.A., Boss, E., Coddington, O., Deschamps, P.-Y., Gao, B.-C., Gross, L., Hasekamp, O., Omar, A., Pelletier, B., Ramon, D., Steinmetz, F., Zhai, P.-W., 2019. Atmospheric Correction of Satellite Ocean-Color Imagery During the PACE Era. *Front. Earth Sci.* 7, 145. <https://doi.org/10.3389/feart.2019.00145>
- Giardino, C., Brando, V.E., Gege, P., Pinnel, N., Hochberg, E., Knaeps, E., Reusen, I., Doerffer, R., Bresciani, M., Braga, F., Foerster, S., Champollion, N., Dekker, A., 2019. Imaging Spectrometry of Inland and Coastal Waters: State of the Art, Achievements and Perspectives. *Surv Geophys* 40, 401–429. <https://doi.org/10.1007/s10712-018-9476-0>
- Gilerson, A., Herrera-Estrella, E., Foster, R., Agaglia, J., Hu, C., Ibrahim, A., Franz, B., 2022. Determining the Primary Sources of Uncertainty in Retrieval of Marine Remote Sensing Reflectance From Satellite Ocean Color Sensors. *Front. Remote Sens.* 3, 857530. <https://doi.org/10.3389/frsen.2022.857530>
- Gilerson, A.A., Gitelson, A.A., Zhou, J., Gurlin, D., Moses, W., Ioannou, I., Ahmed, S.A., 2010. Algorithms for remote estimation of chlorophyll-a in coastal and inland waters using red and near infrared bands. *Opt. Express* 18, 24109. <https://doi.org/10.1364/OE.18.024109>
- Global Modeling and Assimilation Office, 2015a. MERRA-2 tavg1_2d_chm_Nx: 2d,1-Hourly,Time-Averaged,Single-Level,Assimilation,Carbon Monoxide and Ozone Diagnostics V5.12.4, Greenbelt, MD, USA, Goddard Earth Sciences Data and Information Services Center (GES DISC). <https://doi.org/10.5067/3RQ5YS674DGQ>
- Global Modeling and Assimilation Office, 2015b. MERRA-2 tavg1_2d_aer_Nx: 2d,1-Hourly,Time-averaged,Single-Level,Assimilation,Aerosol Diagnostics V5.12.4, Greenbelt, MD, USA, Goddard Earth Sciences Data and Information Services Center (GES DISC). <https://doi.org/10.5067/KLICLTZ8EM9D>
- Gons, H.J., 2005. Effect of a waveband shift on chlorophyll retrieval from MERIS imagery of inland and coastal waters. *Journal of Plankton Research* 27, 125–127. <https://doi.org/10.1093/plankt/fbh151>
- Gons, H.J., Auer, M.T., Effler, S.W., 2008. MERIS satellite chlorophyll mapping of oligotrophic and eutrophic waters in the Laurentian Great Lakes. *Remote Sensing of Environment* 112, 4098–4106. <https://doi.org/10.1016/j.rse.2007.06.029>
- Gordon, H.R., 1985. Ship perturbation of irradiance measurements at sea 1: Monte Carlo simulations. *Appl. Opt.* 24, 4172. <https://doi.org/10.1364/AO.24.004172>
- Gordon, H.R., Wang, M., 1994. Retrieval of water-leaving radiance and aerosol optical thickness over the oceans with SeaWiFS: a preliminary algorithm. *Appl. Opt.*, AO 33, 443–452. <https://doi.org/10.1364/AO.33.000443>
- Gorelick, N., Hancher, M., Dixon, M., Ilyushchenko, S., Thau, D., Moore, R., 2017. Google Earth Engine: Planetary-scale geospatial analysis for everyone. *Remote Sensing of Environment* 202, 18–27. <https://doi.org/10.1016/j.rse.2017.06.031>
- Government of Canada, 2019. An examination of governance, existing data, potential indicators and values in the Ottawa River watershed [WWW Document]. URL <https://publications.gc.ca/site/eng/9.873604/publication.html> (accessed 9.8.24).
- Groetsch, P.M.M., Gege, P., Simis, S.G.H., Eleveld, M.A., Peters, S.W.M., 2017. Variability of adjacency effects in sky reflectance measurements. *Opt. Lett.* 42, 3359. <https://doi.org/10.1364/OL.42.003359>
- Guanter, L., Ruiz-Verdú, A., Odermatt, D., Giardino, C., Simis, S., Estellés, V., Heege, T., Domínguez-Gómez, J.A., Moreno, J., 2010. Atmospheric correction of ENVISAT/MERIS data over inland waters: Validation for European lakes. *Remote Sensing of Environment* 114, 467–480. <https://doi.org/10.1016/j.rse.2009.10.004>
- Harmel, T., Chami, M., Tormos, T., Reynaud, N., Danis, P.-A., 2018. Sunglint correction of the Multi-Spectral Instrument (MSI)-SENTINEL-2 imagery over inland and sea waters from SWIR bands. *Remote Sensing of Environment* 204, 308–321. <https://doi.org/10.1016/j.rse.2017.10.022>
- Hedley, J., Russell, B., Randolph, K., Dierssen, H., 2016. A physics-based method for the remote sensing of seagrasses. *Remote Sensing of Environment* 174, 134–147. <https://doi.org/10.1016/j.rse.2015.12.001>
- Hedley, J.D., Mobley, C.D., 2019. Hydrolight 6 Ecelight 6 User Guide. Numerical Optics Ltd. <https://www.numericaloptics.com/hydrolight.html>

References

- Hedley, J.D., Roelfsema, C., Brando, V., Giardino, C., Kutser, T., Phinn, S., Mumby, P.J., Barrilero, O., Laporte, J., Koetz, B., 2018. Coral reef applications of Sentinel-2: Coverage, characteristics, bathymetry and benthic mapping with comparison to Landsat 8. *Remote Sensing of Environment* 216, 598–614. <https://doi.org/10.1016/j.rse.2018.07.014>
- Heege, T., Fischer, J., 2004. Mapping of water constituents in Lake Constance using multispectral airborne scanner data and a physically based processing scheme. *Canadian Journal of Remote Sensing* 30, 77–86. <https://doi.org/10.5589/m03-056>
- Hieronymi, M., Bi, S., Müller, D., Schütt, E.M., Behr, D., Brockmann, C., Lebreton, C., Steinmetz, F., Stelzer, K., Vanhellemont, Q., 2023. Ocean color atmospheric correction methods in view of usability for different optical water types. *Front. Mar. Sci.* 10, 1129876. <https://doi.org/10.3389/fmars.2023.1129876>
- Houskeeper, H.F., Hooker, S.B., 2023. Extending aquatic spectral information with the first radiometric IR-B field observations. *PNAS Nexus* 2, pgad340. <https://doi.org/10.1093/pnasnexus/pgad340>
- Ibrahim, A., Franz, B.A., Ahmad, Z., Bailey, S.W., 2019. Multiband Atmospheric Correction Algorithm for Ocean Color Retrievals. *Front. Earth Sci.* 7, 116. <https://doi.org/10.3389/feart.2019.00116>
- Ilori, C.O., Knudby, A., 2020. An Approach to Minimize Atmospheric Correction Error and Improve Physics-Based Satellite-Derived Bathymetry in a Coastal Environment. *Remote Sensing* 12, 2752. <https://doi.org/10.3390/rs12172752>
- Iwabuchi, H., Okamura, R., 2017. Multispectral Monte Carlo radiative transfer simulation by the maximum cross-section method. *Journal of Quantitative Spectroscopy and Radiative Transfer* 193, 40–46. <https://doi.org/10.1016/j.jqsrt.2017.01.025>
- Jamet, C., Ibrahim, A., Ahmad, Z., Angelini, F., Babin, M., Behrenfeld, M.J., Boss, E., Cairns, B., Churnside, J., Chowdhary, J., Davis, A.B., Dionisi, D., Duforêt-Gaurier, L., Franz, B., Frouin, R., Gao, M., Gray, D., Hasekamp, O., He, X., Hostettler, C., Kalashnikova, O.V., Knobelispiesse, K., Lacour, L., Loisel, H., Martins, V., Rehm, E., Remer, L., Sanhaj, I., Stamnes, K., Stamnes, S., Victori, S., Werdell, J., Zhai, P.-W., 2019. Going Beyond Standard Ocean Color Observations: Lidar and Polarimetry. *Front. Mar. Sci.* 6, 251. <https://doi.org/10.3389/fmars.2019.00251>
- Jamet, C., Loisel, H., Kuchinke, C.P., Ruddick, K., Zibordi, G., Feng, H., 2011. Comparison of three SeaWiFS atmospheric correction algorithms for turbid waters using AERONET-OC measurements. *Remote Sensing of Environment* 115, 1955–1965. <https://doi.org/10.1016/j.rse.2011.03.018>
- Jiang, D., Spyракος, E., Simis, S., Liu, X., Andral, A., 2022. Technical note: CDOM algorithm development for global inland waters. *ESA Climate Office*. https://climate.esa.int/media/documents/CDOM_Technical_Note_CCN-D_1_V1.2_final.pdf
- Kahma, K.K., 1981. A Study of the Growth of the Wave Spectrum with Fetch. *Journal of Physical Oceanography* 11, 1503–1515. [https://doi.org/10.1175/1520-0485\(1981\)011<1503:ASOTGO>2.0.CO;2](https://doi.org/10.1175/1520-0485(1981)011<1503:ASOTGO>2.0.CO;2)
- Kay, S., Hedley, J., Lavender, S., 2009. Sun Glint Correction of High and Low Spatial Resolution Images of Aquatic Scenes: a Review of Methods for Visible and Near-Infrared Wavelengths. *Remote Sensing* 1, 697–730. <https://doi.org/10.3390/rs1040697>
- Kiselev, V., Bulgarelli, B., Heege, T., 2015. Sensor independent adjacency correction algorithm for coastal and inland water systems. *Remote Sensing of Environment* 157, 85–95. <https://doi.org/10.1016/j.rse.2014.07.025>
- Knudby, A., Nordlund, L., 2011. Remote sensing of seagrasses in a patchy multi-species environment. *International Journal of Remote Sensing* 32, 2227–2244. <https://doi.org/10.1080/01431161003692057>
- Koepke, P., 1984. Effective reflectance of oceanic whitecaps. *Appl. Opt.* 23, 1816. <https://doi.org/10.1364/AO.23.001816>
- Kokaly, R.F., Clark, R.N., Swayze, G.A., Livo, K.E., Hoefen, T.M., Pearson, N.C., Wise, R.A., Benz, W.M., Lowers, H.A., Driscoll, R.L., Klein, A.J., 2017. USGS Spectral Library Version 7 (USGS Numbered Series No. 1035), USGS Spectral Library Version 7, Data Series. U.S. Geological Survey, Reston, VA. <https://doi.org/10.3133/ds1035>
- König, M., Hieronymi, M., Oppelt, N., 2019. Application of Sentinel-2 MSI in Arctic Research: Evaluating the Performance of Atmospheric Correction Approaches Over Arctic Sea Ice. *Front. Earth Sci.* 7, 22. <https://doi.org/10.3389/feart.2019.00022>
- Kotchenova, S.Y., Vermote, E.F., 2007. Validation of a vector version of the 6S radiative transfer code for atmospheric correction of satellite data Part II Homogeneous Lambertian and anisotropic surfaces. *Appl. Opt.* 46, 4455. <https://doi.org/10.1364/AO.46.004455>
- Kotchenova, S.Y., Vermote, E.F., Levy, R., Lyapustin, A., 2008. Radiative transfer codes for atmospheric correction and aerosol retrieval: intercomparison study. *Appl. Opt.* 47, 2215. <https://doi.org/10.1364/AO.47.002215>
- Kotchenova, S.Y., Vermote, E.F., Matarrese, R., Klemm, Jr., F.J., 2006. Validation of a vector version of the 6S radiative transfer code for atmospheric correction of satellite data Part I: Path radiance. *Appl. Opt.* 45, 6762. <https://doi.org/10.1364/AO.45.006762>
- Kuhn, C., de Matos Valerio, A., Ward, N., Loken, L., Sawakuchi, H.O., Kampel, M., Richey, J., Stadler, P., Crawford, J., Strieg, R., Vermote, E., Pahlevan, N., Butman, D., 2019. Performance of Landsat-8 and Sentinel-2 surface reflectance products for river remote sensing retrievals of chlorophyll-a and turbidity. *Remote Sensing of Environment* 224, 104–118. <https://doi.org/10.1016/j.rse.2019.01.023>
- Kutser, T., Hedley, J., Giardino, C., Roelfsema, C., Brando, V.E., 2020. Remote sensing of shallow waters – A 50 year retrospective and future directions. *Remote Sensing of Environment* 240, 111619. <https://doi.org/10.1016/j.rse.2019.111619>
- Lavender, S.J., Pinkerton, M.H., Moore, G.F., Aiken, J., Blondeau-Patissier, D., 2005. Modification to the atmospheric correction of SeaWiFS ocean colour images over turbid waters. *Continental Shelf Research* 25, 539–555. <https://doi.org/10.1016/j.csr.2004.10.007>

References

- Lee, Z., Ahn, Y.-H., Mobley, C., Arnone, R., 2010. Removal of surface-reflected light for the measurement of remote-sensing reflectance from an above-surface platform. *Opt. Express* 18, 26313. <https://doi.org/10.1364/OE.18.026313>
- Lee, Z., Carder, K.L., Mobley, C.D., Steward, R.G., Patch, J.S., 1999. Hyperspectral remote sensing for shallow waters: 2 Deriving bottom depths and water properties by optimization. *Appl. Opt.* 38, 3831. <https://doi.org/10.1364/AO.38.003831>
- Lee, Z., Carder, K.L., Mobley, C.D., Steward, R.G., Patch, J.S., 1998. Hyperspectral remote sensing for shallow waters I A semianalytical model. *Appl. Opt.* 37, 6329. <https://doi.org/10.1364/AO.37.006329>
- Lee, Z., Casey, B., Arnone, R.A., Weidemann, A.D., Parsons, R., Montes, M.J., Gao, B.-C., Goode, W., Davis, C.O., Dye, J., 2007. Water and bottom properties of a coastal environment derived from Hyperion data measured from the EO-1 spacecraft platform. *JARS* 1, 011502. <https://doi.org/10.1117/1.2822610>
- Lee, Z., Pahlevan, N., Ahn, Y.-H., Greb, S., O'Donnell, D., 2013. Robust approach to directly measuring water-leaving radiance in the field. *Appl. Opt.* 52, 1693. <https://doi.org/10.1364/AO.52.001693>
- Lehmann, M.K., Gurlin, D., Pahlevan, N., Alikas, K., Conroy, T., Anstee, J., Balasubramanian, S.V., Barbosa, C.C.F., Binding, C., Bracher, A., Bresciani, M., Burtner, A., Cao, Z., Dekker, A.G., Di Vittorio, C., Drayson, N., Errera, R.M., Fernandez, V., Ficek, D., Fichot, C.G., Gege, P., Giardino, C., Gitelson, A.A., Greb, S.R., Henderson, H., Higa, H., Rahaghi, A.I., Jamet, C., Jiang, D., Jordan, T., Kangro, K., Kravitz, J.A., Kristoffersen, A.S., Kudela, R., Li, L., Ligi, M., Loisel, H., Lohrenz, S., Ma, R., Maciel, D.A., Malthus, T.J., Matsushita, B., Matthews, M., Minaudo, C., Mishra, D.R., Mishra, S., Moore, T., Moses, W.J., Nguyễn, H., Novo, E.M.L.M., Novoa, S., Odermatt, D., O'Donnell, D.M., Olmanson, L.G., Ondrusek, M., Oppelt, N., Ouillon, S., Pereira Filho, W., Plattner, S., Verdú, A.R., Salem, S.I., Schalles, J.F., Simis, S.G.H., Siswanto, E., Smith, B., Somlai-Schweiger, I., Soppa, M.A., Spyarakos, E., Tessin, E., Van Der Woerd, H.J., Vander Woude, A., Vandermeulen, R.A., Vantrepotte, V., Wernand, M.R., Werther, M., Young, K., Yue, L., 2023. GLORIA - A globally representative hyperspectral in situ dataset for optical sensing of water quality. *Sci Data* 10, 100. <https://doi.org/10.1038/s41597-023-01973-y>
- Light, B., 2003. A two-dimensional Monte Carlo model of radiative transfer in sea ice. *J. Geophys. Res.* 108, 3219. <https://doi.org/10.1029/2002JC001513>
- Liou, K.N., 2002. An Introduction to Atmospheric Radiation. Elsevier.
- Lyapustin, A., Wang, Y., 2018. MCD19A2 MODIS/Terra+Aqua Land Aerosol Optical Depth Daily L2G Global 1km SIN Grid V006. NASA EOSDIS Land Processes DAAC. <https://doi.org/10.5067/MODIS/MCD19A2.006>
- Mabit, R., Araújo, C.A.S., Singh, R.K., Bélanger, S., 2022. Empirical Remote Sensing Algorithms to Retrieve SPM and CDOM in Québec Coastal Waters. *Front. Remote Sens.* 3, 834908. <https://doi.org/10.3389/frsen.2022.834908>
- Marchuk, G.I., Mikhailov, G.A., Nazareliev, M.A., Darbinjan, R.A., Kargin, B.A., Elepov, B.S., 1980. The Monte Carlo Methods in Atmospheric Optics, Springer Series in Optical Sciences. Springer-Verlag, Berlin Heidelberg. <https://doi.org/10.1007/978-3-540-35237-2>
- Martins, V.S., Kaleita, A., Barbosa, C.C.F., Fassoni-Andrade, A.C., Lobo, F. de L., Novo, E.M.L.M., 2019. Remote sensing of large reservoir in the drought years: Implications on surface water change and turbidity variability of Sobradinho reservoir (Northeast Brazil). *Remote Sensing Applications: Society and Environment* 13, 275–288. <https://doi.org/10.1016/j.rsase.2018.11.006>
- Mayer, B., 2009. Radiative transfer in the cloudy atmosphere. *Eur. Phys. J. Conferences* 1, 75–99. <https://doi.org/10.1140/epjconf/e2009-00912-1>
- Mayer, B., Hoch, S.W., Whiteman, C.D., 2010. Validating the MYSTIC three-dimensional radiative transfer model with observations from the complex topography of Arizona's Meteor Crater. *Atmos. Chem. Phys.* 10, 8685–8696. <https://doi.org/10.5194/acp-10-8685-2010>
- Mayer, B., Kylling, A., Emde, C., Buras, R., Hamann, U., Gasteiger, J., Richter, B., 2020. libRadtran User's Guide [WWW Document]. URL <http://libradtran.org/doc/libRadtran.pdf>
- McClatchey, R.A., Fenn, R.W., Volz, F.E., Garing, J.S., 1971. Optical Properties of the Atmosphere (Revised). Defense Technical Information Center. <http://www.dtic.mil/docs/citations/AD0726116>
- Minnesota DNR, 2013. Lakes, rivers, and wetlands facts [WWW Document]. Minnesota Department of Natural Resources. URL <https://www.dnr.state.mn.us/faq/mnfacts/water.html> (accessed 11.20.22).
- Mobley, C., 2022. The Oceanic Optics Book. <https://doi.org/10.25607/OPB-1710>
- Mobley, C.D., 2020. Reflectances [WWW Document]. Ocean Optics Web Book. URL <https://www.oceanopticsbook.info/view/inherent-and-apparent-optical-properties/reflectances> (accessed 8.7.23).
- Mobley, C.D., 1999. Estimation of the remote-sensing reflectance from above-surface measurements. *Appl. Opt.* 38, 7442. <https://doi.org/10.1364/AO.38.007442>
- Mobley, C.D., 1994. Chapter 6 Monte Carlo Methods, in: Light and Water: Radiative Transfer in Natural Waters.
- Mobley, C.D., Werdell, J., Franz, B., Ahmad, Z., Bailey, S., 2016. Atmospheric Correction for Satellite Ocean Color Radiometry: A Tutorial and Documentation of the Algorithms Used by the NASA Ocean Biology Processing Group. <https://oceancolor.gsfc.nasa.gov/resources/docs/technical/NASA-TM-2016-217551.pdf>
- Morel, A., Gentili, B., 1996. Diffuse reflectance of oceanic waters III Implication of bidirectionality for the remote-sensing problem. *Appl. Opt.* 35, 4850. <https://doi.org/10.1364/AO.35.004850>
- Morel, A., Maritorena, S., 2001. Bio-optical properties of oceanic waters: A reappraisal. *J. Geophys. Res.* 106, 7163–7180. <https://doi.org/10.1029/2000JC000319>

References

- Morley, S.K., Brito, T.V., Welling, D.T., 2018. Measures of Model Performance Based On the Log Accuracy Ratio. *Space Weather* 16, 69–88. <https://doi.org/10.1002/2017SW001669>
- Moses, W.J., Gitelson, A.A., Berdnikov, S., Saprygin, V., Povazhnyi, V., 2012. Operational MERIS-based NIR-red algorithms for estimating chlorophyll-a concentrations in coastal waters — The Azov Sea case study. *Remote Sensing of Environment* 121, 118–124. <https://doi.org/10.1016/j.rse.2012.01.024>
- Moses, W.J., Sterckx, S., Montes, M.J., De Keukelaere, L., Knaeps, E., 2017. Atmospheric Correction for Inland Waters, in: Bio-Optical Modeling and Remote Sensing of Inland Waters. Elsevier, pp. 69–100.
- Müller, D., Krasemann, H., Brewin, R.J.W., Brockmann, C., Deschamps, P.-Y., Doerffer, R., Fomferra, N., Franz, B.A., Grant, M.G., Groom, S.B., Mélin, F., Platt, T., Regner, P., Sathyendranath, S., Steinmetz, F., Swinton, J., 2015. The Ocean Colour Climate Change Initiative: I. A methodology for assessing atmospheric correction processors based on in-situ measurements. *Remote Sensing of Environment* 162, 242–256. <https://doi.org/10.1016/j.rse.2013.11.026>
- Nechad, B., Dogliotti, A., Ruddick, K., Doxaran, D., 2016. Particulate Backscattering and Suspended Matter Concentration Retrieval From Remote-Sensed Turbidity in Various Coastal and Riverine Turbid Waters. Presented at the ESA Living Planet Symposium.
- Nechad, B., Ruddick, K.G., Neukermans, G., 2009. Calibration and validation of a generic multisensor algorithm for mapping of turbidity in coastal waters. Presented at the SPIE Europe Remote Sensing, Berlin, Germany, p. 74730H. <https://doi.org/10.1117/12.830700>
- Nechad, B., Ruddick, K.G., Park, Y., 2010. Calibration and validation of a generic multisensor algorithm for mapping of total suspended matter in turbid waters. *Remote Sensing of Environment* 114, 854–866. <https://doi.org/10.1016/j.rse.2009.11.022>
- OBPG, 2023. Ancillary Data [WWW Document]. NASA Ocean Biology Processing Group. URL <https://oceancolor.gsfc.nasa.gov/resources/docs/ancillary/> (accessed 9.6.23).
- Odermatt, D., Giardino, C., Heege, T., 2010. Chlorophyll retrieval with MERIS Case-2-Regional in perialpine lakes. *Remote Sensing of Environment* 114, 607–617. <https://doi.org/10.1016/j.rse.2009.10.016>
- Odermatt, D., Kiselev, S., Heege, T., Kneubühler, M., Itten, K.I., 2008. Adjacency effect considerations and air/water constituent retrieval for Lake Constance. <https://doi.org/10.5167/UZH-4507>
- Oestreich, W.K., Ganju, N.K., Pohlman, J.W., Suttles, S.E., 2016. Colored dissolved organic matter in shallow estuaries: relationships between carbon sources and light attenuation. *Biogeosciences* 13, 583–595. <https://doi.org/10.5194/bg-13-583-2016>
- Pahlevan, N., Mangin, A., Balasubramanian, S.V., Smith, B., Alikas, K., Arai, K., Barbosa, C., Bélanger, S., Binding, C., Bresciani, M., Giardino, C., Gurlin, D., Fan, Y., Harmel, T., Hunter, P., Ishikaza, J., Kratzer, S., Lehmann, M.K., Ligi, M., Ma, R., Martin-Lauzer, F.-R., Olmanson, L., Oppelt, N., Pan, Y., Peters, S., Reynaud, N., Sander de Carvalho, L.A., Simis, S., Spyракος, E., Steinmetz, F., Stelzer, K., Sterckx, S., Tormos, T., Tyler, A., Vanhellemont, Q., Warren, M., 2021. ACIX-Aqua: A global assessment of atmospheric correction methods for Landsat-8 and Sentinel-2 over lakes, rivers, and coastal waters. *Remote Sensing of Environment* 258, 112366. <https://doi.org/10.1016/j.rse.2021.112366>
- Pahlevan, N., Smith, B., Schalles, J., Binding, C., Cao, Z., Ma, R., Alikas, K., Kangro, K., Gurlin, D., Hà, N., Matsushita, B., Moses, W., Greb, S., Lehmann, M.K., Ondrusek, M., Oppelt, N., Stumpf, R., 2020. Seamless retrievals of chlorophyll-a from Sentinel-2 (MSI) and Sentinel-3 (OLCI) in inland and coastal waters: A machine-learning approach. *Remote Sensing of Environment* 240, 111604. <https://doi.org/10.1016/j.rse.2019.111604>
- Pan, Y., Bélanger, S., Huot, Y., 2022. Evaluation of Atmospheric Correction Algorithms over Lakes for High-Resolution Multispectral Imagery: Implications of Adjacency Effect. *Remote Sensing* 14, 2979. <https://doi.org/10.3390/rs14132979>
- Paulino, R.S., Martins, V.S., Novo, E.M.L.M., Barbosa, C.C.F., de Carvalho, L.A.S., Begliomini, F.N., 2022. Assessment of Adjacency Correction over Inland Waters Using Sentinel-2 MSI Images. *Remote Sensing* 14, 1829. <https://doi.org/10.3390/rs14081829>
- Quan, X., Fry, E.S., 1995. Empirical equation for the index of refraction of seawater. *Appl. Opt.* 34, 3477. <https://doi.org/10.1364/AO.34.003477>
- RAdCor, 2024. Remote sensing Adjacency Correction [WWW Document]. URL <https://odnature.naturalsciences.be/radcor/> (accessed 1.22.24).
- Ramon, D., Steinmetz, F., Jolivet, D., Compiègne, M., Frouin, R., 2019. Modeling polarized radiative transfer in the ocean-atmosphere system with the GPU-accelerated SMART-G Monte Carlo code. *Journal of Quantitative Spectroscopy and Radiative Transfer* 222–223, 89–107. <https://doi.org/10.1016/j.jqsrt.2018.10.017>
- Reinersman, P.N., Carder, K.L., 1995. Monte Carlo simulation of the atmospheric point-spread function with an application to correction for the adjacency effect. *Appl. Opt.* 34, 4453. <https://doi.org/10.1364/AO.34.004453>
- Richardson, G., Foreman, N., Knudby, A., Wu, Y., Lin, Y., 2024. Global deep learning model for delineation of optically shallow and optically deep water in Sentinel-2 imagery. *Remote Sensing of Environment* 311, 114302. <https://doi.org/10.1016/j.rse.2024.114302>
- Ruddick, K.G., Voss, K., Boss, E., Castagna, A., Frouin, R., Gilerson, A., Hieronymi, M., Johnson, B.C., Kuusk, J., Lee, Z., Ondrusek, M., Vabson, V., Vendt, R., 2019. A Review of Protocols for Fiducial Reference Measurements of Water-Leaving Radiance for Validation of Satellite Remote-Sensing Data over Water. *Remote Sensing* 11, 2198. <https://doi.org/10.3390/rs11192198>

References

- Saleh, R., Marks, M., Heo, J., Adams, P.J., Donahue, N.M., Robinson, A.L., 2015. Contribution of brown carbon and lensing to the direct radiative effect of carbonaceous aerosols from biomass and biofuel burning emissions. *J. Geophys. Res.-Atmos.* 120, 10285–10296. <https://doi.org/10.1002/2015JD023697>
- Santer, R., Schmechtig, C., 2000. Adjacency effects on water surfaces: primary scattering approximation and sensitivity study. *Appl. Opt.* 39, 361. <https://doi.org/10.1364/AO.39.000361>
- Santer, R., Sterckx, S., 2013. SIMEC-ICOL-ODESA processing MERIS (ISECA-A2). <https://core.ac.uk/download/pdf/45437215.pdf>
- Schaepman-Strub, G., Schaepman, M.E., Painter, T.H., Dangel, S., Martonchik, J.V., 2006. Reflectance quantities in optical remote sensing—definitions and case studies. *Remote Sensing of Environment* 103, 27–42. <https://doi.org/10.1016/j.rse.2006.03.002>
- Sei, A., 2015. Efficient correction of adjacency effects for high-resolution imagery: integral equations, analytic continuation, and Padé approximants. *Appl. Opt.* 54, 3748. <https://doi.org/10.1364/AO.54.003748>
- Shen, F., Verhoef, W., Zhou, Y., Salama, Mhd.S., Liu, X., 2010. Satellite Estimates of Wide-Range Suspended Sediment Concentrations in Changjiang (Yangtze) Estuary Using MERIS Data. *Estuaries and Coasts* 33, 1420–1429. <https://doi.org/10.1007/s12237-010-9313-2>
- South Nation Conservation, 2023. State of the Nation Watershed Report Card 2023. <https://www.nation.on.ca/water/reports/watershed-report-cards>
- Stamnes, K., Tsay, S.-C., Wiscombe, W., Jayaweera, K., 1988. Numerically stable algorithm for discrete-ordinate-method radiative transfer in multiple scattering and emitting layered media. *Appl. Opt.* 27, 2502. <https://doi.org/10.1364/AO.27.002502>
- Steinmetz, F., Deschamps, P.-Y., Ramon, D., 2011. Atmospheric correction in presence of sun glint: application to MERIS. *Opt. Express* 19, 9783. <https://doi.org/10.1364/OE.19.009783>
- Steinmetz, F., Ramon, D., 2018. Sentinel-2 MSI and Sentinel-3 OLCI consistent ocean colour products using POLYMER, in: Frouin, R.J., Murakami, H. (Eds.), . Presented at the Remote Sensing of the Open and Coastal Ocean and Inland Waters, SPIE, Honolulu, United States, p. 13. <https://doi.org/10.1117/12.2500232>
- Sterckx, S., Knaeps, E., Ruddick, K., 2011. Detection and correction of adjacency effects in hyperspectral airborne data of coastal and inland waters: the use of the near infrared similarity spectrum. *International Journal of Remote Sensing* 32, 6479–6505. <https://doi.org/10.1080/01431161.2010.512930>
- Sterckx, S., Knaeps, S., Kratzer, S., Ruddick, K., 2015. SIMilarity Environment Correction (SIMEC) applied to MERIS data over inland and coastal waters. *Remote Sensing of Environment* 157, 96–110. <https://doi.org/10.1016/j.rse.2014.06.017>
- Stramska, M., 2003. Observations of oceanic whitecaps in the north polar waters of the Atlantic. *J. Geophys. Res.* 108, 3086. <https://doi.org/10.1029/2002JC001321>
- Tanré, D., Deschamps, P.Y., Duhaut, P., Herman, M., 1987. Adjacency effect produced by the atmospheric scattering in thematic mapper data. *J. Geophys. Res.* 92, 12000. <https://doi.org/10.1029/JD092iD10p12000>
- Tanré, D., Herman, M., Deschamps, P.Y., 1981. Influence of the background contribution upon space measurements of ground reflectance. *Appl. Opt.* 20, 3676. <https://doi.org/10.1364/AO.20.003676>
- Tilstone, G., Dall'Olmo, G., Hieronymi, M., Ruddick, K., Beck, M., Ligi, M., Costa, M., D'Alimonte, D., Vellucci, V., Vansteenwegen, D., Bracher, A., Wiegmann, S., Kuusk, J., Vabson, V., Ansko, I., Vendt, R., Donlon, C., Casal, T., 2020. Field Intercomparison of Radiometer Measurements for Ocean Colour Validation. *Remote Sensing* 12, 1587. <https://doi.org/10.3390/rs12101587>
- Vanhellemont, Q., 2023. ACOLITE User Manual. URL <https://github.com/acolite/acolite/releases/tag/20231023.0>
- Vanhellemont, Q., 2019a. Adaptation of the dark spectrum fitting atmospheric correction for aquatic applications of the Landsat and Sentinel-2 archives. *Remote Sensing of Environment* 225, 175–192. <https://doi.org/10.1016/j.rse.2019.03.010>
- Vanhellemont, Q., 2019b. Adaptation of the dark spectrum fitting atmospheric correction for aquatic applications of the Landsat and Sentinel-2 archives. *Remote Sensing of Environment* 225, 175–192. <https://doi.org/10.1016/j.rse.2019.03.010>
- Vanhellemont, Q., Ruddick, K., 2018. Atmospheric correction of metre-scale optical satellite data for inland and coastal water applications. *Remote Sensing of Environment* 216, 586–597. <https://doi.org/10.1016/j.rse.2018.07.015>
- Vermote, E.F., El Saleous, N., Justice, C.O., Kaufman, Y.J., Privette, J.L., Remer, L., Roger, J.C., Tanré, D., 1997a. Atmospheric correction of visible to middle-infrared EOS-MODIS data over land surfaces: Background, operational algorithm and validation. *J. Geophys. Res.* 102, 17131–17141. <https://doi.org/10.1029/97JD00201>
- Vermote, E.F., Tanré, D., Deuze, J.L., Herman, M., Morcrette, J.-J., 2006. Second Simulation of a Satellite Signal in the Solar Spectrum - Vector (6SV). 6S User Guide Version 3. URL <https://ltdri.org/6spage.html>
- Vermote, E.F., Tanré, D., Deuze, J.L., Herman, M., Morcrette, J.-J., 1997b. Second Simulation of the Satellite Signal in the Solar Spectrum, 6S: an overview. *IEEE Trans. Geosci. Remote Sensing* 35, 675–686. <https://doi.org/10.1109/36.581987>
- Vidot, J., Santer, R., 2005. Atmospheric correction for inland waters—application to SeaWiFS. *International Journal of Remote Sensing* 26, 3663–3682. <https://doi.org/10.1080/01431160500034029>
- Wang, M., Bailey, S.W., 2001. Correction of sun glint contamination on the SeaWiFS ocean and atmosphere products. *Appl. Opt.* 40, 4790. <https://doi.org/10.1364/AO.40.004790>
- Wang, M., Jiang, L., 2018. Atmospheric Correction Using the Information From the Short Blue Band. *IEEE Trans. Geosci. Remote Sensing* 56, 6224–6237. <https://doi.org/10.1109/TGRS.2018.2833839>
- Wang, M., Shi, W., 2005. Estimation of ocean contribution at the MODIS near-infrared wavelengths along the east coast of the U.S.: Two case studies. *Geophysical Research Letters* 32, 2005GL022917. <https://doi.org/10.1029/2005GL022917>

References

- Wang, T., Du, L., Yi, W., Hong, J., Zhang, L., Zheng, J., Li, C., Ma, X., Zhang, D., Fang, W., Huang, H., Wang, A., Song, B., Zhou, N., Ti, R., Li, K., Cui, W., 2021a. An adaptive atmospheric correction algorithm for the effective adjacency effect correction of submeter-scale spatial resolution optical satellite images: Application to a WorldView-3 panchromatic image. *Remote Sensing of Environment* 259, 112412. <https://doi.org/10.1016/j.rse.2021.112412>
- Wang, T., Zhou, N., Yi, W.-N., Hong, J., Liu, X., Li, X., Zhang, Q., Liu, S.-Y., Li, Z.-Z., Li, K.-T., Cui, W.-Y., 2021b. Adjacency effect correction of optical satellite image with sub-meter spatial resolution. *Acta Physica Sinica* 70, 139101–1. <https://doi.org/10.7498/aps.70.20202187>
- Warren, M.A., Simis, S.G.H., Martinez-Vicente, V., Poser, K., Bresciani, M., Alikas, K., Spyarakos, E., Giardino, C., Ansper, A., 2019. Assessment of atmospheric correction algorithms for the Sentinel-2A MultiSpectral Imager over coastal and inland waters. *Remote Sensing of Environment* 225, 267–289. <https://doi.org/10.1016/j.rse.2019.03.018>
- Warren, M.A., Simis, S.G.H., Selmes, N., 2021. Complementary water quality observations from high and medium resolution Sentinel sensors by aligning chlorophyll-a and turbidity algorithms. *Remote Sensing of Environment* 265, 112651. <https://doi.org/10.1016/j.rse.2021.112651>
- Watson-Parris, D., Schutgens, N., Reddington, C., Pringle, K.J., Liu, D., Allan, J.D., Coe, H., Carslaw, K.S., Stier, P., 2019. In situ constraints on the vertical distribution of global aerosol. *Atmos. Chem. Phys.* 19, 11765–11790. <https://doi.org/10.5194/acp-19-11765-2019>
- Werdell, P.J., McKenna, L.I.W., Boss, E., Ackleson, S.G., Craig, S.E., Gregg, W.W., Lee, Z., Maritorena, S., Roesler, C.S., Rousseaux, C.S., Stramski, D., Sullivan, J.M., Twardowski, M.S., Tzortziou, M., Zhang, X., 2018. An overview of approaches and challenges for retrieving marine inherent optical properties from ocean color remote sensing. *Progress in Oceanography* 160, 186–212. <https://doi.org/10.1016/j.pocean.2018.01.001>
- Wilson, K.L., Wong, M.C., Devred, E., 2020. Branching Algorithm to Identify Bottom Habitat in the Optically Complex Coastal Waters of Atlantic Canada Using Sentinel-2 Satellite Imagery. *Front. Environ. Sci.* 8, 579856. <https://doi.org/10.3389/fenvs.2020.579856>
- Wilson, R.T., 2013. Py6S: A Python interface to the 6S radiative transfer model. *Computers & Geosciences* 51, 166–171. <https://doi.org/10.1016/j.cageo.2012.08.002>
- Wu, Y., Knudby, A., Lapen, D., 2023. Topography-adjusted Monte Carlo simulation of the adjacency effect in remote sensing of coastal and inland waters. *Journal of Quantitative Spectroscopy and Radiative Transfer* 303, 108589. <https://doi.org/10.1016/j.jqsrt.2023.108589>
- Wu, Y., Knudby, A., Pahlevan, N., Lapen, D., Zeng, C., 2024. Sensor-generic adjacency-effect correction for remote sensing of coastal and inland waters. *Remote Sensing of Environment* 315, 114433. <https://doi.org/10.1016/j.rse.2024.114433>
- Xu, L., Xiong, W., Yi, W., Qiu, Z., Liu, X., Zhang, D., Fang, W., Li, Z., Hou, W., Lin, J., Hu, Z., Wang, T., Cui, W., 2022. Synchronous Atmospheric Correction of High Spatial Resolution Images from Gao Fen Duo Mo Satellite. *Remote Sensing* 14, 4427. <https://doi.org/10.3390/rs14174427>
- YSI, n.d. Exo User Manual [WWW Document]. URL <https://www.xylem.com/siteassets/brand/ysi/resources/manual/exo-user-manual-web.pdf> (accessed 11.24.24).
- Zhai, P.-W., Hu, Y., Chowdhary, J., Trepte, C.R., Lucker, P.L., Josset, D.B., 2010. A vector radiative transfer model for coupled atmosphere and ocean systems with a rough interface. *Journal of Quantitative Spectroscopy and Radiative Transfer* 111, 1025–1040. <https://doi.org/10.1016/j.jqsrt.2009.12.005>
- Zhang, H., Wang, M., 2010. Evaluation of sun glint models using MODIS measurements. *Journal of Quantitative Spectroscopy and Radiative Transfer* 111, 492–506. <https://doi.org/10.1016/j.jqsrt.2009.10.001>